UNIVERSITAT DE BARCELONA

Prospects of microwave spectrometry for vascular stent monitoring

Towards a non-invasive and non-ionizing follow-up alternative

Gianluca Arauz Garofalo

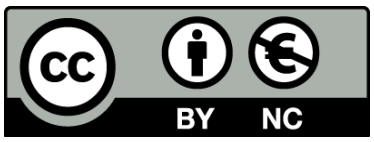

Prospects of microwave spectrometry for vascular stent monitoring

Towards a non-invasive and non-ionizing follow-up alternative

by

Gianluca Arauz Garofalo

A dissertation submitted to *Facultat de Física*
in candidacy for the degree of Doctor
in the subject of Condensed Matter Physics
Programa de Doctorat de Física

Departament de Física de la Matèria Condensada

UNIVERSITAT DE BARCELONA

Advisors:
Prof. Javier Tejada Palacios
Dr. Antoni García Santiago

Tutor:
Dr. Giancarlo Franzese

Barcelona, June 2017

Prospects of microwave spectrometry for vascular stent monitoring

Towards a non-invasive and non-ionizing follow-up alternative

Prospects of microwave spectrometry for vascular stent monitoring

Towards a non-invasive and non-ionizing follow-up alternative

Gianluca Arauz Garofalo

Universitat de Barcelona

A mis padres Misael y María,
a mi hermano Misa,
y a mi compañera Laila.

Gracias por vuestra paciencia, os quiero.

Contents

List of acronyms

BA	**B**alloon **A**ngioplasty
BMS	**B**are-**M**etal **S**tent
DES	**D**rug-**E**luting **S**tent
IHD	**I**schemic **H**eart **D**isease
ISNA	**I**n-**S**tent **N**eo-**A**therosclerosis
ISR	**I**n-**S**tent **R**estenosis
IVUS	**I**ntra**V**ascular **U**ltra**S**ound
MWS	**M**icro**W**ave **S**pectrometry
MDS	**M**edtronic **D**river **S**print® bare-metal stent
MES	**M**edtronic **E**ndeavor **S**print® zotarolimus-eluting stent
OCT	**I**ntravascular **O**ptical **C**oherence **T**omography
PCI	**P**ercutaneous **C**oronary **I**ntervention
SF	**S**tent **F**racture
VNA	**V**ector **N**etwork **A**nalyzer
XRA	**X**-**R**ay **A**ngiography

List of Tables

List of Figures

Resumen

Esta tesis se titula *Prospects of microwave spectrometry for vascular stent monitoring: Towards a non-invasive and non-ionizing follow-up alternative*. En ella se recoge gran parte de los trabajos que realicé en el *Grup de Magnetisme* de la *Universitat de Barcelona* entre los años 2010 y 2016. A lo largo de la presente memoria he evaluado las perspectivas de una técnica basada en microondas, bautizada como espectrometría de microondas, como posible alternativa no invasiva y no ionizante para el seguimiento médico de pacientes con estents vasculares. La ordenación de los capítulos de esta tesis es bastante fiel al orden cronológico en el que se obtuvieron y se publicaron los resultados. Parte del contenido de los Capítulos 2, 3 y 4 fue publicado en 2014 en un extenso artículo enviado a la revista *Medical Physics*. De la misma manera, parte del contenido del Capítulo 5 fue publicado en 2015, esta vez de forma más sumaria, en la revista *Biomedical Physics & Engineering Express*. Estos dos artículos, además de representar las primeras publicaciones del *Grup de Magnetisme* sobre "microondas y estents", sirvieron de base para solicitar dos proyectos: el primero financiado por el Ministerio de Economía y Competitividad[1]; y el segundo por la *Fundació La Marató de TV3*[2]. A pesar de haber trabajado en ambos, la presente memoria no recoge mis contribuciones en dichos proyectos.

La tesis mantiene un tono marcadamente experimental e interdisciplinar desde el capítulo introductorio. Dependiendo de la experiencia

[1] TEC2013-49465-EXP, de un año de duración (iniciado en Febrero 2015).
[2] 201535-30-31, de tres años de duración (iniciado en Enero de 2016)

del lector, el contenido de la memoria puede llegar a parecer "demasiado médico" o "demasiado técnico". Como físico, he intentado combinar ambos enfoques en su justa medida, pretendiendo transmitir los resultados independientemente de la experiencia original del lector.

El Capítulo 1 consta de una introducción médica retrospectiva y generalista, así como de un resumen sobre los últimos avances en las técnicas de monitorización de estents basadas en microondas. En la primera parte de este capítulo se repasa el impacto de las enfermedades cardiovasculares y circulatorias en las estadísticas de mortalidad globales, resaltando la cardiopatía isquémica como la principal causa de mortalidad mundial. A continuación, se revisa el desarrollo histórico de las intervenciones coronarias percutáneas, haciendo especial énfasis en la angioplastia de globo y los estents. Después de exponer los prometedores resultados de estas revolucionarias estrategias, se presenta la restenosis intra-estent como la principal complicación derivada de la implantación del estent, haciendo inevitable el seguimiento médico invasivo e/o ionizante de los pacientes con estents. Finalmente se resume las principales técnicas de monitorización de stents basadas en el uso de microondas propuestas recientemente.

En el Capítulo 2 se introduce el funcionamiento del montaje de espectrometría de microondas. Primero mostramos cómo el equipo es capaz de obtener la absorbancia de un estent en función de la frecuencia y el ángulo azimutal de los campos de microondas incidentes. También se ilustra cómo toda esta información puede combinarse en un único diagrama de absorción, y cómo se identifican las frecuencias de resonancia de los estents sobre dichos diagramas. A modo de ejemplo se presenta un diagrama de absorción típico con la intención de ilustrar las características generales de dichas resonancias. Concretamente se destaca su naturaleza discreta y sus patrones angulares multilobulares.

En el Capítulo 3 se caracteriza un gran número de estents de diversos tamaños nominales con la intención de interpretar las resonancias de los estents en términos de dispersión de microondas. Primero se encontra que las frecuencias de resonancia siguen una dependencia recíproca con la longitud de los estents. Esto permite obtener una expresión empírica para la frecuencia en función de la longitud simplemente ajustando dos parámetros. Sin embargo, no se

pudo encontrar una expresión análoga para el diámetro de los estents. En cualquier caso, al inspeccionar la dependencia de la frecuencia con del diámetro, se descubre inesperadamente como la arquitectura del estent influye en su correspondiente frecuencia de resonancia. Recopilando todos estos resultados finalmente se sugiere un sencillo modelo medio empírico medio teórico que relaciona la frecuencia de resonancia del estent con su integridad estructural (a través la longitud del estent), así como con las propiedades electromagnéticas del medio circundante (a través de la permitividad dieléctrica relativa y la permeabilidad magnética relativa del medio). También se estima teóricamente la frecuencia resonante que presentaría un estent implantado a partir de su correspondiente frecuencia resonante en espacio libre, mostrando que las resonancias *in vivo* serían alrededor de un orden de magnitud menores que las respectivas resonancias en espacio libre.

En los Capítulos 4 y 5 se explora las capacidades diagnósticas potenciales de la espectrometría de microondas en dos escenarios posibles: la fractura de estent y la neoaterosclerosis intra-estent. Ambos capítulos constan de una breve introducción médica, donde se repasa la incidencia, las implicaciones médicas y los mecanismos de estas dos complicaciones derivadas de la implantación del estent. En el Capítulo 4 se evalúa la fractura de estent mediante dos "pruebas de fractura" consistentes en una serie de cortes sucesivos en los puntales del estent. Se demuestra que la espectrometría de microondas proporciona indicadores cualitativos de fracturas en los puntales del estent (disminución de la frecuencia de resonancia fundamental), así como indicadores cuantitativos de fracturas lineales transversales completas del stent (división e incremento de la frecuencia de resonancia fundamental). En el Capítulo 5 se evalúa la neoaterosclerosis intra-estent mediante cuatro "pruebas de colesterol" consistentes en un proceso gradual de deposición de colesterol. Se demuestra que la espectrometría de microondas proporciona un indicador cualitativo para la creciente presencia de colesterol alrededor del estent (disminución gradual de la frecuencia de resonancia fundamental). El capítulo concluye con el cálculo teórico de la evolución de la frecuencia de resonancia fundamental a lo largo del proceso de deposición de colesterol, estimándose el límite superior para el desplazamiento de dicha frecuencia. De esta manera, los Capítulos 4 y 5 muestran el

potencial de la espectrometría de microondas para la detección de fracturas de stent y neoaterosclerosis intra-estent.

En su conjunto, los resultados presentados en esta tesis evalúan las perspectivas de la espectrometría de microondas como alternativa de futuro a las actuales técnicas de seguimiento utilizadas en pacientes portadores de estents vasculares.

1

Introduction and motivation

The development of percutaneous coronary interventions throughout the second half of the last century represented a revolution in interventional cardiology. In particular, balloon angioplasty with stenting became the preferred choice in the treatment of ischemic heart disease, establishing a solid alternative to risky open-heart surgeries. However, stented patients require chronic follow-up due to the several complications arising from stent deployment. To date, stent evaluation relies on ionizing or invasive methodologies and, given these limitations, it would be ideal to have an alternative technology at disposal. In this thesis we have assessed the prospects of microwave spectrometry as a non-invasive non-ionizing approach for stent monitoring. In order to acquaint the reader with the interdisciplinary tone of the text, this generalist retrospective chapter provides a medical background and a state-of-the-art summary of existing microwave-based stent monitoring approaches. First, we will contextualize the specific weight of ischemic heart disease in global mortality, devoting special attention to atherosclerosis. Then, we will review the birth of stenting, and we will present the gold standard follow-up modalities for stented patients. Finally, we will summarize the emerging stent monitoring approaches based on microwave techniques.

1.1 Global mortality statistics

Along 2010 there were 52.8 million human deaths worldwide according to the last Global Burden of Disease Study published in 2012

[1]. In this study, the causes of all these deaths are grouped into three major categories: non-communicable disorders (34.6 million deaths), communicable disorders (13.2 million deaths), and injuries (5.1 million deaths). In turn, these three categories are subdivided into a number of disease groups. The pie chart in Figure 1.1 specifies the rates of each disease group within the three main categories. Among all, the group established by cardiovascular and circulatory diseases was the major contributor to the 2010 global mortality with 15.6 million deaths (see the darkest blue pie slice). Similarly, this group can be broken down into sundry different cardiovascular and circulatory-related diseases. The stacked bar in Figure 1.1 provides the rates associated with each cardiovascular and circulatory-related disease. Worldwide, ischemic heart disease (IHD) was the top cause of death in 2010, contributing 7.0 million fatalities (see the darkest orange stack bar slice), which represents a 13.3% of the total. It is particularly worrisome the upward trend of this rate, which in 1990 only constituted a 11.2% [1]. In view of these statistics we are immediately aware of the magnitude of the health problem represented by cardiovascular diseases in general, and IHD in particular.

1.2 Ischemic heart disease and atherosclerosis

The first description of a cardiac ischemic event is attributed to the physician James Bryan Herrick and occurred in 1912, more than a century ago [2]. IHD (also known as coronary artery disease, atherosclerotic heart disease, atherosclerotic cardiovascular disease, or coronary heart disease) includes a subgroup of disorders characterized by a reduced blood flow through the coronary arteries irrigating the myocardium. Due to the lack of oxygen cardiac muscle cells suffer starvation, which is clinically manifested as angina pectoris, myocardial infarction, or sudden cardiac death [3]. Usually, the onset of IHD is closely related to atherosclerosis, a specific form of arteriosclerosis. Arteriosclerosis is a general term encompassing those situations where the artery wall becomes thicker, harder, and less elastic than normal. In particular, atherosclerosis is characterized by the formation of an atheromatous lesion within the vessel wall. This chronic condition of the artery has traditionally been considered just

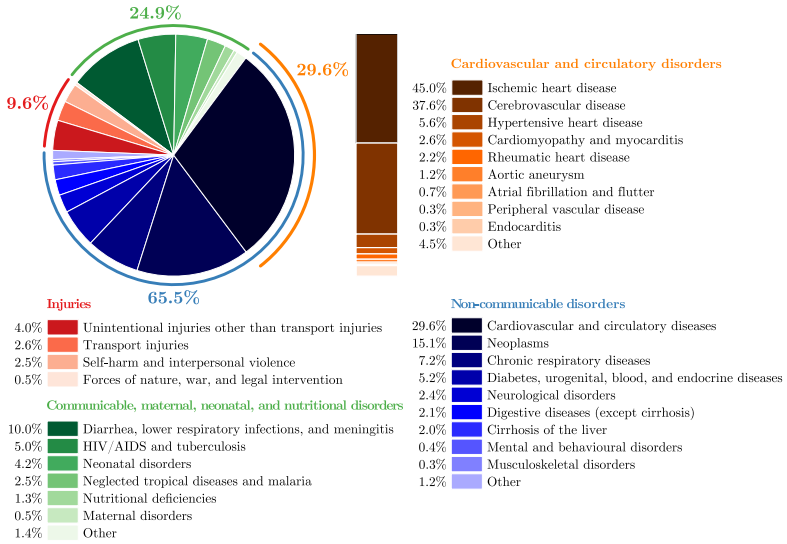

Figure 1.1: Pie chart summarizing the global mortality statistics in 2010. Reddish, greenish and bluish colors denote deaths caused by injuries, communicable disorders and non-communicable disorders, respectively. The orangish stacked bar breaks down all the cardiovascular and circulatory-related diseases comprising this last group (see legend for details). Data taken from Ref. [1].

as mere cholesterol storage disease, but now is recognized as a complex succession of biochemical and inflammatory/immunomodulatory reactions involving the multiple cell types within the various layers of a human artery wall [4].

Figure 1.2 illustrates the layered organization of a healthy artery wall from a morpho-histological viewpoint. From innermost to outermost these layers, or tunicae, are called intima, media, and adventitia. Two elastic membranes act as frontiers in between of them, the internal (separating intima and media), and the external (separating media and adventitia). Overlying the adventitia, a monolayer of endothelial cells protects the rest of the artery wall. On the other side of the endothelium, the bloodstream flows through the artery lumen carrying the usual blood cells, such erythrocytes (red blood cells), leukocytes (white blood cells), and thrombocytes (platelets). Atherogenesis is usually triggered when certain irritating stimuli

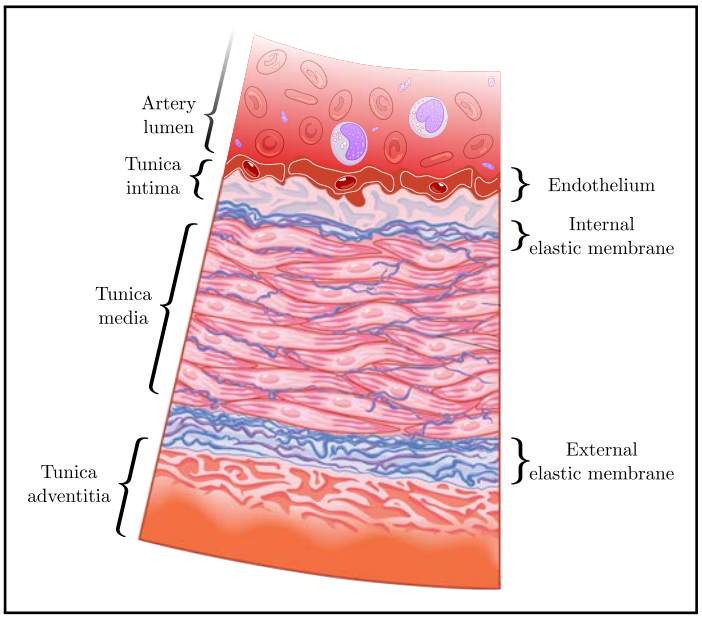

Figure 1.2: Sketch showing the layered organization of a human artery wall. The tunica intima is composed by a monolayer of endothelial cells. The tunica media contains stratified smooth muscle cells embedded within an extracellular matrix of elastin fibers. The tunica adventitia is mainly made of collagen fibers. Graphics adapted from Encyclopædia Britannica [7].

lead the endothelium to a pathological state known as endothelial dysfunction [5, 6].

Figure 1.3 qualitatively illustrates the temporal evolution of atherogenesis, showing three related complications. As we have just mentioned, when the endothelium of a healthy artery is damaged, the vascular homeostasis becomes impaired, and its permeability to plasma lipoproteins increases (Figure 1.3a). Eventually, some LDLs (low-density lipoproteins) may go across and lodge within the intima, from where they induce the overlying endothelial cells to capture monocytes, one type of white blood cell [8]. The adhered monocytes are able to migrate towards the underlying intima, where they differentiate to macrophages. Such phagocyter cells start engulfing the lipoproteins allocated within the intima, and accumulate large amounts of lipid droplets inside. Gradually, they become foam cells,

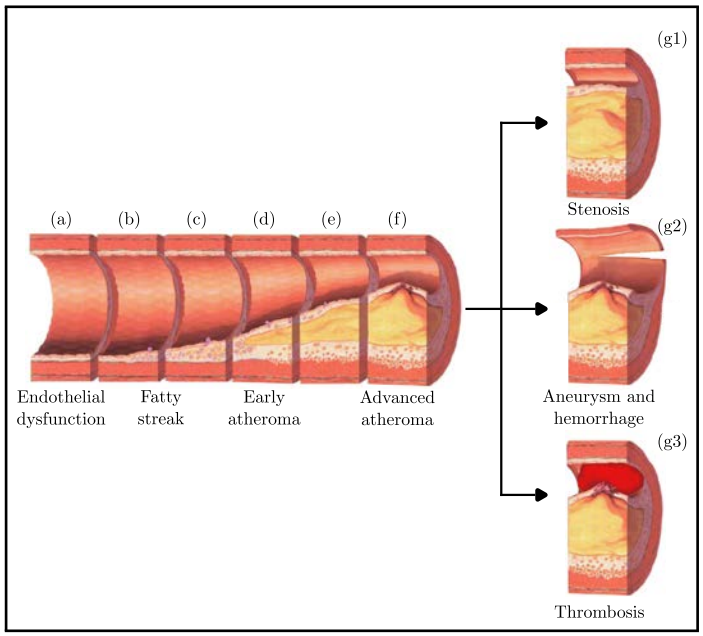

Figure 1.3: Sketch showing the temporal evolution of atheromatous lesions. The main stages of atherogenesis are: endothelial dysfunction (a); foam cells accumulation (b); fatty streak formation (c); plaque formation (d) and maturation (e); and vulnerable plaque formation (f). Finally, three usual ending scenarios are also represented: critical stenosis (g1); aneurysm with subsequent hemorrhage (g2); and thrombosis following the fibrous cap disruption (g3). Graphics adapted from Wikimedia Commons [9].

which are lipid-laden macrophages (Figure 1.3b). As a consequence of the exaggerated amount of lipids they phagocyte, these foam cells begin to die. Foam cells do not only release to the intima all the lipids previously assimilated while dying, but they also send several biochemical signals that, again, induce the endothelial cells to capture even more monocytes. Then, the cycle just described feeds back until the accumulation of lipids and foam cells within the intima forms a lesion called fatty streak (Figure 1.3b to 1.3c).

The appearance of this lesion unleashes another series of adverse events that eventually would lead to the formation of the atheroma plaque itself. Some platelets from the bloodstream come to assist and try to repair the damaged endothelium. In their attempt, these

platelets release biochemical signals that encourage the smooth muscle cells from the media to migrate towards the endothelium. Once there, the smooth muscle cells proliferate and start to produce extracellular matrix molecules such collagen, elastin and proteoglycans. As a result, the fatty streak is covered by a protective layer known as fibrous cap. This fatty streak encapsulated by the fibrous cap is what we call atheroma plaque (Figure 1.3d). In parallel, the lipid loadings released by dying foam cells continue to accumulate until they form a large extracellular lipid-rich pool called necrotic core [10]. Moreover, some smooth muscle cells die as well, providing calcium as additional extracellular debris. Such calcification along with the formation of tiny crystals of cholesterol thicken the atheroma plaque and gradually make the artery wall more fragile (Figure 1.3f).

Finally, this high-risk situation may be a prelude to several acute clinical manifestations. On the one hand, the artery lumen may reach a critical blood flow reduction if the atheroma plaque continues developing. This narrowing, called stenosis, may cause angina pectoris or myocardial infarction (Figure 1.3g1). On the other hand, if the artery wall weakens enough, a balloon-like bulge may appear in the vessel. Eventually, this blood-filled abnormal dilatation, know as aneurysm, may breach and lead to severe hemorrhage (Figure 1.3g2). Last but not least, the disruption of the fibrous cap may trigger the formation of a blood clot. When the thrombogenic factors of the underlying necrotic core are exposed to the bloodstream, platelets flock around and coagulate the circulating red blood cells (Figure 1.3g3). Now, this cluster of platelets, red blood cells, and fibrin, the so-called thrombus, can block the blood flow locally or embolize downstream towards distal arteries. In the first case, angina and myocardial infarction can occur. In the second case, the consequences depend on where the embolized thrombus ends up. For example, the occlusion of the internal carotid or the middle cerebral arteries lead to strokes and cerebral atrophy; an occluded popliteal artery can cause peripheral vascular ischemia, like gangrene or claudication.

Any condition leading to endothelial dysfunction would represent an important atherosclerosis risk factor. Hypertension, dyslipidemia, tobacco smoking, obesity, diabetes and aging are some of the best examples of atherosclerosis risk factors which are known to alter the normal functioning of the endothelium [11].

1.3 Percutaneous coronary interventions and restenosis

Throughout the last century, cardiologist have developed different solutions to prevent or manage IHD. Pharmacological [12] and interventional [13] approaches are good examples of such multiple strategies. Among all interventional options introduced in the second half of the 20^{th} century, percutaneous coronary interventions (PCIs) in general, and angioplasty plus stenting in particular, represented the most revolutionary treatments against IHD. In this section we will briefly review the birth of balloon angioplasty, bare-metal stents, and drug-eluting stents, the three milestones that denote the most important hallmarks in PCI history [14, 15]. We will also make a parenthesis to introduce the concept of restenosis, which is still the main antagonist of this story.

1.3.1 Balloon angioplasty

Balloon angioplasty (BA) is a type of PCI consisting in a small perforation of a peripheral artery (usually the femoral or the radial artery) and the subsequent introduction of a long guide-wire within its lumen. This allows to head a catheter with a deflated balloon towards the coronary arteries. Once accurately positioned at the target atherosclerotic lesion, the balloon can be expanded to compress the atheroma plaque and thus rehabilitate the blood flow across the vessel (see Figure 1.4). This catheter-based endovascular technique was conceived in 1964 by the interventional radiologists Charles Theodore Dotter and Melvin Paul Judkins [17]. In their report of the first transluminal revascularization of atherosclerotic lesions in human peripheral arteries, Dotter and Judkins provided the earliest conceptual description of modern BA [17]:

> *"It was our plan to attempt a more adequate dilatation as soon as an expandable guide could be devised."*

More than a decade later, in 1977, Andreas Roland Grüntzig performed the first coronary BA in a human being [18]. This milestone constituted the birth of contemporary BA and represents the first hallmark in the development of PCI. In the course of the following years, with refinement in technique and improvement in operator

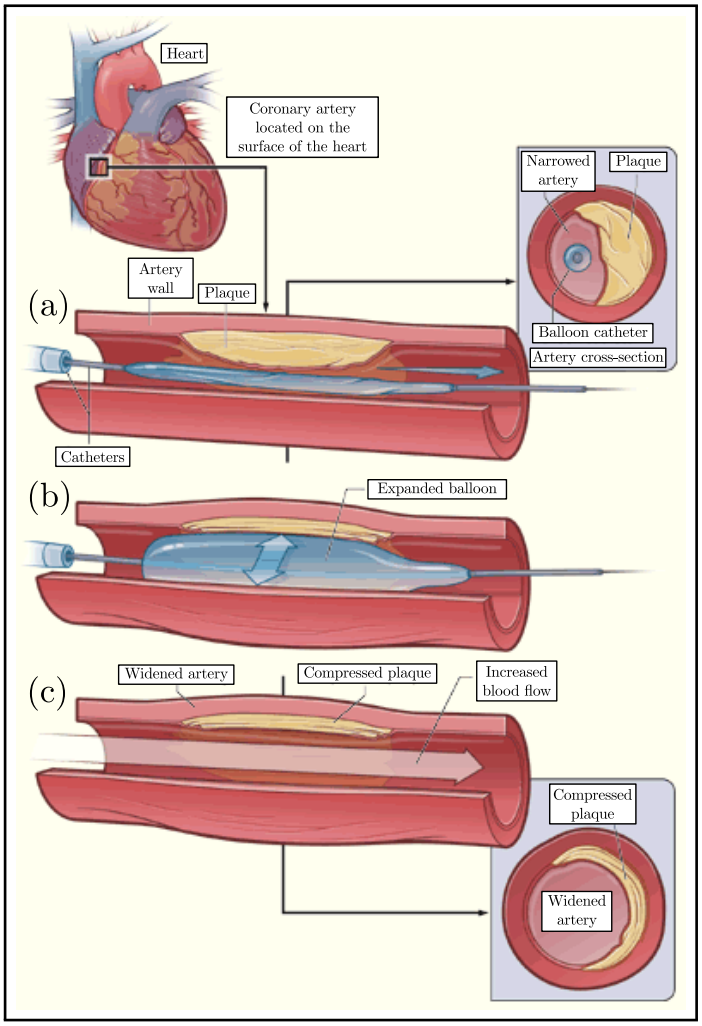

Figure 1.4: Sketch showing the BA procedure. The balloon catheter is guided to the target lesion location (a), and then is inflated (b). As a result the atheroma plaque is compressed and the myocardium revascularized (c). Graphics adapted from the National Heart, Lung, and Blood Institute, National Institute of Health, U.S. Department of Health and Human Services [16].

experience, this minimally invasive method represented a solid alternative to risky open-heart surgeries, such coronary artery bypass grafting. Indeed, in less than two decades the number of procedures performed grew five orders of magnitude: from 7 in 1977 to almost 700,000 in 1994 [19].

1.3.2 Restenosis

The promising outcomes of BA were compromised by the high rates derived from post-procedural complications. Before the 90s, approximately half of patients submitted to BA required repeated revascularization interventions [20], especially due to a complication known as post-BA restenosis. It is precisely for this reason that some authors have referred to restenosis as "the Achilles heel of coronary angioplasty" [21]. From a clinical viewpoint, restenosis is defined as a recurrent angina pectoris occurring in a previously revascularized vessel, which requires a repeated intervention [22]. Alternatively, restenosis can also be defined from an angiographical perspective as a vessel lumen renarrowing larger than 50% [23]. The risk factors associated with restenosis are multi-factorial and highly heterogeneous. The most widely accepted are inflammation [24] and diabetes mellitus [25], among others [26].

Despite that the mechanisms behind restenosis have not yet been fully understood, the vascular injury caused by balloon dilatation seems to play a central role in its onset [26]. Like all PCIs, BA involves endothelial denudation and medial tearing. The resulting inflammatory response triggers the migration of smooth mucle cells from the damaged tunica media towards the tunica intima, where they start an uncontrolled proliferation and production of extracellular matrix molecules [27, 28]. Eventually, this process, know as neointimal hyperplasia, ends up narrowing the artery lumen, which ultimately leads to the manifestation of renewed clinical symptoms and the need for a repeated revascularization. We shall emphasize here that restenosis and atherosclerosis processes are significantly different in several respects. While an atherosclerotic tissue is mainly lipidic in nature and evolve over various decades, a restenotic tissue is rather fibrotic and may manifest just a few weeks after BA [29].

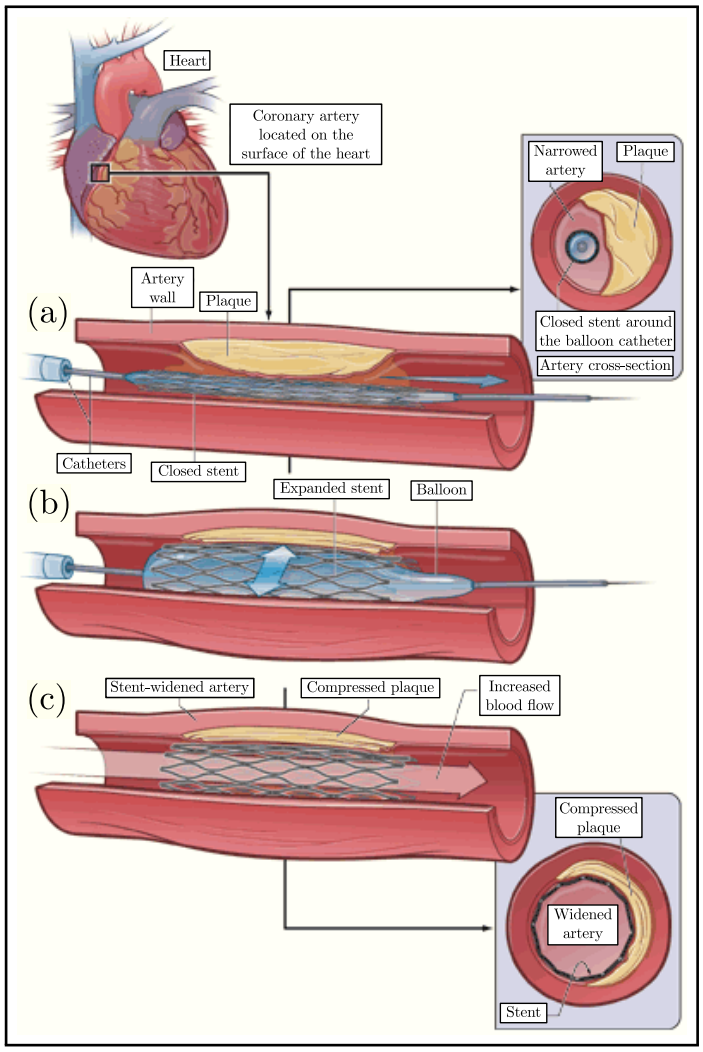

Figure 1.5: Sketch showing the stenting procedure. The balloon catheter with the cramped stent is guided to the target lesion location (a), and then is inflated (b). As a result the stent is deployed and the myocardium revascularized (c). Graphics adapted from the National Heart, Lung, and Blood Institute, National Institute of Health, U.S. Department of Health and Human Services [16].

1.3.3 Bare-metal stenting

There is no dispute that BA represented a deep revolution in the treatment of IHD, but a 50% post-BA restenosis rate was unacceptably high. This drawback prompted the development of the bare-metal stent (BMS) for the treatment of IHD. In essence, the stenting procedure is completely analogous to BA. The only difference between both kinds of PCI is the introduction of a small but revolutionary element: the stent [30]. This endovascular prosthetic device is a cylindrical tube with wire mesh walls which is previously mounted on the balloon catheter. Once the catheter with the cramped stent is well positioned at a target atherosclerotic lesion, the balloon can be inflated to expand the stent against the arterial wall. As a result, the atheroma plaque is compressed, and the stent is deployed providing an optimum scaffolding to the coronary artery lumen (see Figure 1.5). The first coronary stenting in a human being was performed in 1986 by Ulrich Sigwart *et al.* [20]. Sigwart and his collaborators described their endovascular prosthetic device as follows [20]:

> *"A new system has been developed, consisting of a stainless-steel multifilament, self-expanding, macroporous stent and an innovative instrument for placing it."*

This stent ancestor was baptized as Medinvent Wallstent® bare-metal stent[1], and its pioneering deployment in a coronary artery represented the second hallmark in the evolution of PCI. Further stent refinements and upgrades ultimately led to the first stents approved by the FDA (U.S. Food and Drug Administration), such the Cook Gianturco-Roubin Flex-Stent® bare-metal stent[2] [31] and the Johnson & Johnson Palmaz-Schatz® bare-metal stent[3] [32]. The subsequent publication of the BENESTENT (Belgian Netherlands Stent) [33] and the STRESS (Stent Restenosis Study) [34] clinical trials in 1994, constituted the final big push for PCI. Both studies demonstrated the superiority of BMS over BA in terms of post-procedure restenosis rates, and therefore established stenting as the preferred choice in the treatment of IHD with PCI. Indeed, by 1999 around 84% of all PCI performed included stent deployment [35].

[1] Medinvent, Lausanne, Vaud, Switzerland.
[2] Cook Medical, Bloomington, IN, USA.
[3] Johnson & Johnson Interventional Systems, Warren, NJ, USA.

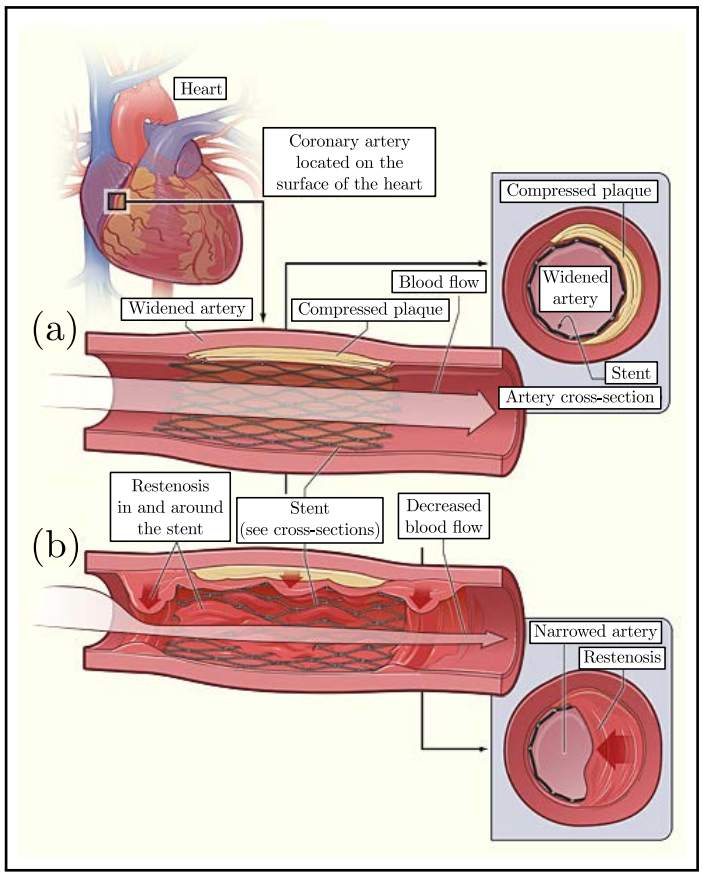

Figure 1.6: Sketch representing in-stent restenosis. A previously stented lesion (a) experiences a process of neointimal hyperplasia which critically reduces blood flow (b). Graphics adapted from the National Heart, Lung, and Blood Institute, National Institute of Health, U.S. Department of Health and Human Services [16].

1.3.4 Drug-eluting stenting

The use of BMSs reduced post-BA restenosis rates from 50% to just $20\% - 30\%$ [36]. However, post-stenting restenosis (see Figure 1.6), now called in-stent restenosis (ISR), remained remarkably frequent among stented patients. The drug-eluting stent (DES) was specifically devised to further minimize ISR rates and therefore "heal the Achilles heel of coronary angioplasty" [37]. A DES is just a BMS incorporating a polymer coat carrying an anti-restenotic drug, such paclitaxel, sirolimus, everolimus, or zotarolimus. The first coronary DESs in human beings were deployed in 1999 by José Eduardo Moraes Rego Sousa *et al.* as part of a pioneering thirty-patients study sponsored by Johnson & Johnson [38]. According to the report published by Sousa and his team, the DES used was [38]:

> *"A laser-cut, 316L stainless steel, balloon-expandable stent that contains a fixed amount of sirolimus per unit of metal surface area."*

The preliminary results obtained with this first DES were very promising. They showed minimal neointimal proliferation at four months after the stent implantation [38], and one-year sustained suppression of ISR [39]. The outstanding results of this innovative stent type represented the third hallmark in the development of PCI. Three years later, and after several clinical trials comparing BMSs with the novel DES [40, 41], the FDA approved the launch of the Cordis Cypher® sirolimus-eluting stent[4], the commercial version of the pioneer stent studied by Sousa and his team. Just one year later, in 2004, the FDA also approved the Boston Scientific Taxus® paclitaxel-eluting stent[5], which showed equally promising results [42]. The success of the first generation sirolimus- and paclitaxel-eluting stents ultimately led to the development of the second generation of everolimus- and zotarolimus-eluting stents so widely used today [43, 44], and supposed the definitive consolidation of PCI as a treatment of IHD. Since then, the technology behind PCI is still undergoing continuous upgrades [45]. Better anti-restenotic drugs, such novolimus or biolimus, are currently under study [46, 47]. Other promising innovations are bioresorbable stenting [48] and drug-coated balloon angioplasty [49].

[4]Cordis Corporation, Warren, NJ, USA.
[5]Boston Scientific, Natick, MA, USA.

1.4 Microwave-based stent monitoring

Through the previous section we have seen that the development of PCI could be envisaged like a struggle between stents and restenosis. First, BMSs reduced the original post-BA restenosis rate from 50% [20] to $20\% - 30\%$ [36] and then, the remaining ISR rate was further minimized to just $5\% - 10\%$ thanks to DESs [50]. Despite the unquestionable success of DESs, stent failure still represents a risk in interventional cardiology. For this reason patients with stents require chronic medication and monitoring in order to prevent or manage stent-related complications, such as ISR or stent thrombosis [51]. However, stented patients cannot be subjected to an exhaustive medical follow-up. Nowadays, the stent evaluation relies on ionizing or invasive techniques, such x-ray angiography (XRA) [52], intravascular ultrasound (IVUS) [53], and intravascular optical coherence tomography (OCT) [54], which require hospitalization and trained physicians. In view of the drawbacks of current gold standard monitoring techniques, it would be ideal to have a non-invasive, non-ionizing methodology at disposal that could be performed by non-specialized medical personnel.

Microwaves comprise the portion of the electromagnetic spectrum with frequencies between 0.3 GHz and 300 GHz, which is equivalent to wavelengths between 100 cm and 0.1 cm [55]. The maximum energy associated with this type of electromagnetic waves (1.24 meV), is four orders or magnitude lower than the ionizing energies of typical atoms in biological tissues (10 eV). As a consequence, microwaves are classified as non-ionizing radiation. As the understanding of the interaction between microwaves and biological tissues progressed, there has been an increasing presence of microwave-based technologies in medicine [56, 57]. In particular, several stent monitoring alternatives which use microwaves have been proposed along the last decade.

The first steps in this promising field started around 2002, when Ken'Ichi Takahata and his work team developed a method for manufacturing stents from thin foils of stainless steel [58]. Their microelectrodischarge machining-based technique enabled them to produce novel stent designs with optimal mechanical performance and customized electromagnetic properties [59]. In particular, they devised the "stentenna", a stent that, due to its helical architecture, acts as a cylindrical inductive antenna with a given inductance, L_{st} [60].

Assuming a circular cross-section area, the stentenna inductance could be approximated as

$$L_{\mathrm{st}} \approx \frac{\pi \mu d^2 N^2}{4\ell}, \tag{1.1}$$

where ℓ and d are the length and the diameter of the stentenna, respectively, μ is the magnetic permeability of the material inside the stentenna lumen, and N is the number of turns of the stentenna architecture. Additionally, they mounted on this stentenna a capacitive pressure sensor microchip able to link its overall capacitance, C_{st}, with ambient pressure, p. As a result, the whole stentenna/sensor construct behaves like a resonant LC circuit with a characteristic resonance angular frequency that depends on ambient pressure:

$$\omega_0(p) = \frac{1}{\sqrt{L_{\mathrm{st}} C_{\mathrm{st}}(p)}}. \tag{1.2}$$

Now, the resulting LC circuit can be inductively coupled to an external coil, and thus p can be telemetrically queried by scanning the impedance of the equivalent circuit from hundredths to tenths of gigahertz. Starting with this clever idea, Takahata and his team developed a passive dual-inductor stentenna with two pressure sensors (one at each stentenna end) able to provide blood pressure and flow when wirelessly interrogated (see Figure 1.7a) [60]. This first version was subsequently redesigned to improve its performance (see Figure 1.7b) [61, 62], ultimately leading to very promising *in vivo* tests in porcine animal models [63]. Nowadays, Takahata and coauthors are focused on improving the stentenna reading range, which is around 2.5 cm [64]. Taking advantage of the same principle, they are also investigating alternative applications, such as wireless endohyperthermia treatment of ISR [65, 66].

Another outstanding contribution in the field was provided by the group led by Pedro P. Irazoqui. In 2009 they developed an implantable wireless monitoring platform by assembling two identical stents, a transmitter microchip, and a battery (see Figure 1.7c) [67]. This initial prototype worked as an active dipole antenna able to transmit a gigahertz electromagnetic wave to an external receiver. In subsequent reports, Irazoqui and coauthors validated the transcutaneous emission of the stent-based transmitter in multiple scenarios (such as free space, saline solution phantoms, and *ex vivo*/*in*

vivo porcine animal models), reporting a communication range up to 50 cm. In later works, they successfully correlated experimental and computational results by running high-fidelity simulations[6] [68]. Further technical optimizations, such electronics miniaturization and the use of remote powering by electromagnetic wave propagation, ultimately enabled them to present a fully wireless-pressure-sensing prototype (see Figure 1.7d) [69]. They have also proposed additional innovations inspired on the same stent-based transmitter, such as a wireless piezoelectric microcantilever-based sensor able to monitor the endothelization process after stenting [70].

Finally, despite not having reached the maturation level of Takahata's and Irazoqui's approaches, the proposal of Gaetano Marrocco and his colleagues also results noteworthy. In 2012, and using the well-establish radio frequency identification (RFID) technology, they develop the "STENTag" [71], a passive device with an operating frequency slightly below the gigahertz. This STENTag comprises a stent, an inductor, and an integrated circuit whose impedance is sensitive to variations in the dielectric properties of the surrounding medium (see Figure 1.7e). In their paper, Marrocco and coauthors provided some preliminary results exploring the use of this STENTag to report the onset of ISR.

1.5 Aim and structure of this thesis

Although they present some differences, such as the communication directionality or the operating frequency window, the approaches led by Takahata, Irazoqui and Marrocco pursued a similar goal: the monitoring of a previously stented vessel by means of a microwave-based technique. To a lesser or a greater extent, these works have shown the ability of using microwaves to establish a wireless link between an implanted stent and an external device (emitter or receiver). However, all these approaches rely on the implementation of complex electronic elements on the stent scaffold. This fact may restrict their use in mid-to-low caliber vessel segments. In addition, the possible adverse effects arising from the presence of such bulky foreign bodies within the vessel lumen are completely unknown. Starting from the

[6] HFSS™ HBM (High Frequency Structural Simulator Human Body Model), Ansoft Corporation, Pittsburgh, PA, USA.

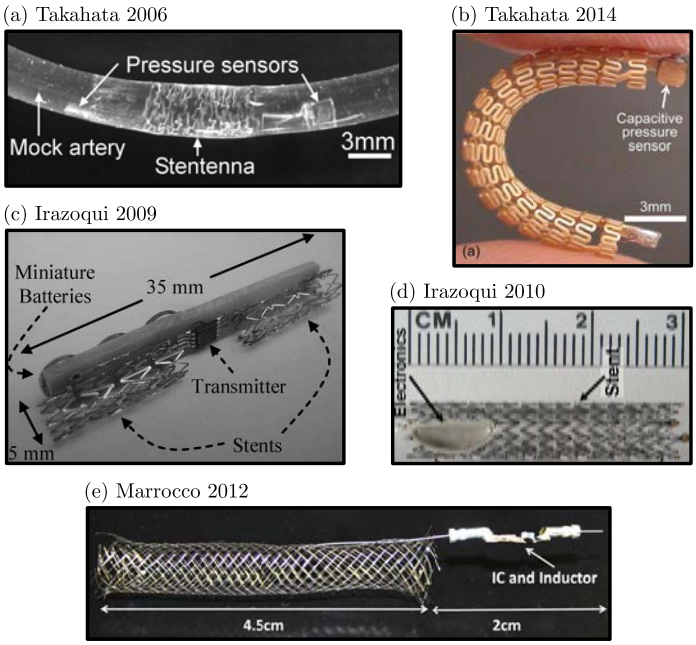

Figure 1.7: Emerging microwave-based approaches for stent monitoring. (a) and (b) Initial and advanced versions of the stentenna developed by Takahata *et al.*, respectively. (c) and (d) First and final prototypes of the implantable wireless monitoring platform elaborated by Irazoqui *et al.*, respectively. (e) First version of the STENTag proposed by Marrocco *et al.* Figures extracted from Refs. [60], [63], [67], [69] and [71], respectively.

premise of not incorporating any modification to the stent scaffold, could it be possible to check the stent status using a microwave-based technique? If so, what information could we obtain? Our goal is to assess the prospects of a microwave-based technique, that we have called microwave spectrometry (MWS), as a non-ionizing non-invasive monitoring alternative for patients with vascular stents.

Since every chapter of this thesis starts with its own brief introduction, here we will just highlight the main aspects regarding its general structure. In Chapter 2, we will present our MWS setup and its working principle. We will introduce the concept of stent resonance frequency, and we will acquaint the reader with the absorbance diagram, a type of plot that will appear very frequently throughout the following chapters. In Chapter 3, we will characterize

a large number of stents with a wide variety of sizes. The data will enable us to propose a formal framework which will help us to better understand the interaction between microwave electromagnetic waves and stents. Finally, in Chapters 4 and 5, we will take advantage of our modest half-theoretical half-empirical model to test MWS in two scenarios: stent fracture and in-stent neoatherosclerosis. In addition to representing a risk *per se*, there are emerging evidences that these two conditions play an important role in the onset of several stent-related complications such ISR and stent thrombosis. Therefore, their early detection would potentially improve the stenting outcome.

Driven, perhaps, by our inclination to experimental physics, our work followed a deeply empirical approach. As a matter of fact, we used the experimental results we gradually collected as a source of inspiration to propose very simple models that allowed us to interpret the physics underlying the observed phenomena. Additionally, as the reader may have already note, the overall tone of this text is quite interdisciplinary. This may cause the thesis content to appear "too medical" or "too technical" depending on the background of the particular reader. As physicists, we have made a great effort to combine both approaches in a fair measure. We wish to be able to transmit our work to any reader regardless of its original experience, while hoping not to make it seem "too physical".

References

[1] R. Lozano, M. Naghavi, K. Foreman, S. Lim, K. Shibuya, V. Aboyans, J. Abraham, T. Adair, R. Aggarwal, S. Y. Ahn, M. A. AlMazroa, M. Alvarado, H. R. Anderson, L. M. Anderson, K. G. Andrews, C. Atkinson, L. M. Baddour, S. Barker-Collo, D. H. Bartels, M. L. Bell, E. J. Benjamin, D. Bennett, K. Bhalla, B. Bikbov, A. B. Abdulhak, G. Birbeck, F. Blyth, I. Bolliger, S. Boufous, C. Bucello, M. Burch, P. Burney, J. Carapetis, H. Chen, D. Chou, S. S. Chugh, L. E. Coffeng, S. D. Colan, S. Colquhoun, K. E. Colson, J. Condon, M. D. Connor, L. T. Cooper, M. Corriere, M. Cortinovis, K. C. de Vaccaro, W. Couser, B. C. Cowie, M. H. Criqui, M. Cross, K. C. Dabhadkar, N. Dahodwala, D. De Leo, L. Degenhardt, A. Delossantos, J. Denenberg, D. C. Des Jarlais, S. D. Dharmaratne, E. R. Dorsey, T. Driscoll, H. Duber, B. Ebel, P. J. Erwin, P. Espindola, M. Ezzati, V. Feigin, A. D. Flaxman, M. H. Forouzanfar, F. G. R. Fowkes, R. Franklin, M. Fransen, M. K. Freeman, S. E. Gabriel, E. Gakidou, F. Gaspari, R. F. Gillum, D. Gonzalez-Medina, Y. A. Halasa, D. Haring, J. E. Harrison, R. Havmoeller, R. J. Hay, B. Hoen, P. J. Hotez, D. Hoy, K. H. Jacobsen, S. L. James, R. Jasrasaria, S. Jayaraman, N. Johns, G. Karthikeyan, N. Kassebaum, A. Keren, J.-P. Khoo, L. M. Knowlton, O. Kobusingye, A. Koranteng, R. Krishnamurthi, M. Lipnick, S. E. Lipshultz, S. L. Ohno, J. Mabweijano, M. F. MacIntyre, L. Mallinger, L. March, G. B. Marks, R. Marks, A. Matsumori, R. Matzopoulos, B. M. Mayosi, J. H. McAnulty, M. M. McDermott, J. McGrath, Z. A. Memish, G. A. Mensah, T. R. Merriman, C. Michaud, M. Miller, T. R. Miller, C. Mock, A. O. Mocumbi, A. A. Mokdad, A. Moran, K. Mulholland, M. N. Nair, L. Naldi, K. M. V. Narayan, K. Nasseri, P. Norman, M. O'Donnell, S. B. Omer, K. Ortblad, R. Osborne, D. Ozgediz, B. Pahari, J. D. Pandian, A. P. Rivero, R. P. Padilla, F. Perez-Ruiz, N. Perico, D. Phillips, K. Pierce, I. Pope, C Arden, E. Porrini, F. Pourmalek, M. Raju, D. Ranganathan, J. T. Rehm, D. B. Rein, G. Remuzzi, F. P. Rivara, T. Roberts, F. R. De León, L. C. Rosenfeld, L. Rushton, R. L. Sacco, J. A. Salomon, U. Sampson, E. Sanman, D. C. Schwebel, M. Segui-Gomez, D. S. Shepard, D. Singh, J. Singleton, K. Sliwa, E. Smith, A. Steer, J. A. Taylor, B. Thomas,

I. M. Tleyjeh, J. A. Towbin, T. Truelsen, E. A. Undurraga, N. Venketasubramanian, L. Vijayakumar, T. Vos, G. R. Wagner, M. Wang, W. Wang, K. Watt, M. A. Weinstock, R. Weintraub, J. D. Wilkinson, A. D. Woolf, S. Wulf, P.-H. Yeh, P. Yip, A. Zabetian, Z.-J. Zheng, A. D. Lopez, and C. J. Murray, "Global and regional mortality from 235 causes of death for 20 age groups in 1990 and 2010: A systematic analysis for the global burden of disease study 2010," The Lancet **380**, 2095–2128 (2012) (cit. on pp. 2, 3).

[2] J. B. Herrick, "Clinical features of sudden obstruction of the coronary arteries," The Journal of the American Medical Association **250**, 1757–1762 (1983) (cit. on p. 2).

[3] N. D. Wong, "Epidemiological studies of CHD and the evolution of preventive cardiology," Nature Reviews Cardiology **11**, 276–289 (2014) (cit. on p. 2).

[4] P. Libby, P. M. Ridker, and G. K. Hansson, "Progress and challenges in translating the biology of atherosclerosis," Nature **473**, 317–325 (2011) (cit. on p. 3).

[5] E. Gutiérrez, A. J. Flammer, L. O. Lerman, J. Elízaga, A. Lerman, and F. Fernández-Avilés, "Endothelial dysfunction over the course of coronary artery disease," European Heart Journal **34**, 3175–3181 (2013) (cit. on p. 4).

[6] S. Sitia, L. Tomasoni, F. Atzeni, G. Ambrosio, C. Cordiano, A. Catapano, S. Tramontana, F. Perticone, P. Naccarato, P. Camici, E. Picano, L. Cortigiani, M. Bevilacqua, L. Milazzo, D. Cusi, C. Barlassina, P. Sarzi-Puttini, and M. Turiel, "From endothelial dysfunction to atherosclerosis," Autoimmunity Reviews **9**, 830–834 (2010) (cit. on p. 4).

[7] *Artery (anatomy)*, Encyclopædia Britannica, (2017) `https://global.britannica.com/science/artery` (cit. on p. 4).

[8] I. Tabas, K. J. Williams, and J. Borén, "Subendothelial lipoprotein retention as the initiating process in atherosclerosis," Circulation **116**, 1832–1844 (2007) (cit. on p. 4).

[9] *Late complications of atherosclerosis*, Wikimedia Commons, (2017) `https://commons.wikimedia.org/wiki/File:Late_complications_of_atherosclerosis.PNG` (cit. on p. 5).

[10] I. Tabas, "Macrophage death and defective inflammation resolution in atherosclerosis," Nature reviews. Immunology **10**, 36–46 (2010) (cit. on p. 6).

[11] K.-H. Park, and W. J. Park, "Endothelial dysfunction: Clinical implications in cardiovascular disease and therapeutic approaches," The Korean Academy of Medical Sciences **30**, 1213–1225 (2015) (cit. on p. 6).

[12] H. K. Saini, Y.-J. Xu, A. S. Arneja, P. S. Tappia, and N. S. Dhalla, "Pharmacological basis of different targets for the treatment of atherosclerosis," Journal of Cellular and Molecular Medicine **9**, 818–839 (2005) (cit. on p. 7).

[13] J. Iqbal, J. Gunn, and P. W. Serruys, "Coronary stents: Historical development, current status and future directions," British Medical Bulletin **106**, 193 (2013) (cit. on p. 7).

[14] R. L. Mueller, and T. A. Sanborn, "The history of interventional cardiology: Cardiac catheterization, angioplasty, and related interventions," American Heart Journal **129**, 146–172 (1995) (cit. on p. 7).

[15] S. B. King, "Angioplasty from bench to bedside to bench," Circulation **93**, 1621–1629 (1996) (cit. on p. 7).

[16] *What is coronary heart disease?* National Heart, Lung, Blood Institute; National Institute of Health; U.S. Department of Health, and Human Services, (2017) `https://www.nhlbi.nih.gov/` (cit. on pp. 8, 10, 12).

[17] C. T. Dotter, and M. P. Judkins, "Transluminal treatment of arteriosclerotic obstruction," Circulation **30**, 654–670 (1964) (cit. on p. 7).

[18] A. Grüntzig, "Transluminla dilatation of coronary-artery stenosis," The Lancet **311**, 263 (1978) (cit. on p. 7).

[19] S. N. Paranandi, and E. J. Topol, "Contemporary clinical trials of restenosis," The Journal of invasive cardiology **6**, 109–124 (1994) (cit. on p. 9).

[20] U. Sigwart, J. Puel, V. Mirkovitch, F. Joffre, and L. Kappenberger, "Intravascular stents to prevent occlusion and restenosis after transluminal angioplasty," New England Journal of Medicine **316**, 701–706 (1987) (cit. on pp. 9, 11, 14).

[21] R. L. Wurdeman, D. E. Hilleman, and A. N. Mooss, "Restenosis, the Achilles' heel of coronary angioplasty," Pharmacotherapy: The Journal of Human Pharmacology and Drug Therapy **18**, 1024–1040 (1998) (cit. on p. 9).

[22] D. E. Cutlip, S. Windecker, R. Mehran, A. Boam, D. J. Cohen, G.-A. van Es, P. Gabriel Steg, M.-a. Morel, L. Mauri, P. Vranckx, E. McFadden, A. Lansky, M. Hamon, M. W. Krucoff, and P. W. Serruys, "Clinical end points in coronary stent trials," Circulation **115**, 2344–2351 (2007) (cit. on p. 9).

[23] R. Mehran, G. Dangas, A. S. Abizaid, G. S. Mintz, A. J. Lansky, L. F. Satler, A. D. Pichard, K. M. Kent, G. W. Stone, and M. B. Leon, "Angiographic patterns of in-stent restenosis," Circulation **100**, 1872–1878 (1999) (cit. on p. 9).

[24] R. Kornowski, M. K. Hong, F. O. Tio, O. Bramwell, H. Wu, and M. B. Leon, "In-stent restenosis: Contributions of inflammatory responses and arterial injury to neointimal hyperplasia," Journal of the American College of Cardiology **31**, 224–230 (1998) (cit. on p. 9).

[25] J. Gilbert, J. Raboud, and B. Zinman, "Meta-analysis of the effect of diabetes on restenosis rates among patients receiving coronary angioplasty stenting," Diabetes Care **27**, 990–994 (2004) (cit. on p. 9).

[26] J. W. Jukema, J. J. W. Verschuren, T. A. N. Ahmed, and P. H. A. Quax, "Restenosis after PCI. Part 1: Pathophysiology and risk factors," Nature Reviews Cardiology **9**, 53–62 (2012) (cit. on p. 9).

[27] W. R. Agema, J. W. Jukema, S. N. Pimstone, and J. J. Kastelein, "Genetic aspects of restenosis after percutaneous coronary interventions: Towards more tailored therapy," European heart journal **22**, 2058–2074 (2001) (cit. on p. 9).

[28] P. S. Monraats, W. R P Agema, and J. W. Jukema, "Genetic predictive factors in restenosis," Pathologie-biologie **52**, 186–195 (2004) (cit. on p. 9).

[29] V. Rajagopal, and S. G. Rockson, "Coronary restenosis: A review of mechanisms and management," The American Journal of Medicine **115**, 547–553 (2003) (cit. on p. 9).

[30] S. Garg, and P. W. Serruys, "Coronary stents: Current status," Journal of the American College of Cardiology **56**, S1–S42 (2010) (cit. on p. 11).

[31] P. J. Macander, S. K. Agrawal, and G. S. Roubin, "The Gianturco-Roubin balloon-expandable intracoronary flexible coil stent," The Journal of invasive cardiology **3**, 85–94 (1991) (cit. on p. 11).

[32] R. A. Schatz, D. S. Baim, M. Leon, S. G. Ellis, S. Goldberg, J. W. Hirshfeld, M. W. Cleman, H. S. Cabin, C. Walker, and J. Stagg, "Clinical experience with the Palmaz-Schatz coronary stent. initial results of a multicenter study," Circulation **83**, 148–161 (1991) (cit. on p. 11).

[33] P. W. Serruys, P. de Jaegere, F. Kiemeneij, C. Macaya, W. Rutsch, G. Heyndrickx, H. Emanuelsson, J. Marco, V. Legrand, P. Materne, J. Belardi, U. Sigwart, A. Colombo, J. J. Goy, P. van den Heuvel, J. Delcan, and M.-a. Morel, "A comparison of balloon-expandable-stent implantation with balloon angioplasty in patients with coronary artery disease," New England Journal of Medicine **331**, 489–495 (1994) (cit. on p. 11).

[34] D. L. Fischman, M. B. Leon, D. S. Baim, R. A. Schatz, M. P. Savage, I. Penn, K. Detre, L. Veltri, D. Ricci, M. Nobuyoshi, M. Cleman, R. Heuser, D. Almond, P. S. Teirstein, R. D. Fish, A. Colombo, J. Brinker, J. Moses, A. Shaknovich, J. Hirshfeld, S. Bailey, S. Ellis, R. Rake, and S. Goldberg, "A randomized comparison of coronary-stent placement and balloon angioplasty in the treatment of coronary artery disease," New England Journal of Medicine **331**, 496–501 (1994) (cit. on p. 11).

[35] D. R. Holmes, M. Savage, J.-M. LaBlanche, L. Grip, P. Serruys, P. Fitzgerald, D. Fischman, S. Goldberg, J. A. Brinker, A. Zeiher, L. M. Shapiro, J. Willerson, B. R. Davis, J. J. Ferguson, J. Popma, S. B. King, A. M. Lincoff, J. E. Tcheng, R. Chan, J. R. Granett, and M. Poland, "Results of prevention of restenosis with tranilast and its outcomes (presto) trial," Circulation **106**, 1243–1250 (2002) (cit. on p. 11).

[36] R. Fattori, and T. Piva, "Drug-eluting stents in vascular intervention," The Lancet **361**, 247–249 (2003) (cit. on pp. 13, 14).

[37] D. J. Moliterno, "Healing Achilles - sirolimus versus paclitaxel," New England Journal of Medicine **353**, 724–727 (2005) (cit. on p. 13).

[38] J. E. Sousa, M. A. Costa, A. Abizaid, A. S. Abizaid, F. Feres, I. M. F. Pinto, A. C. Seixas, R. Staico, L. A. Mattos, A. G. M. R. Sousa, R. Falotico, J. Jaeger, J. J. Popma, and P. W. Serruys, "Lack of neointimal proliferation after implantation of sirolimus-coated stents in human coronary arteries," Circulation **103**, 192–195 (2001) (cit. on p. 13).

[39] J. E. Sousa, M. A. Costa, A. C. Abizaid, B. J. Rensing, A. S. Abizaid, L. F. Tanajura, K. Kozuma, G. Van Langenhove, A. G. Sousa, R. Falotico, J. Jaeger, J. J. Popma, and P. W. Serruys, "Sustained suppression of neointimal proliferation by sirolimus-eluting stents," Circulation **104**, 2007–2011 (2001) (cit. on p. 13).

[40] M.-C. Morice, P. W. Serruys, J. E. Sousa, J. Fajadet, E. Ban Hayashi, M. Perin, A. Colombo, G. Schuler, P. Barragan, G. Guagliumi, F. Molnàr, and R. Falotico, "A randomized comparison of a sirolimus-eluting stent with a standard stent for coronary revascularization," New England Journal of Medicine **346**, 1773–1780 (2002) (cit. on p. 13).

[41] J. W. Moses, M. B. Leon, J. J. Popma, P. J. Fitzgerald, D. R. Holmes, C. O'Shaughnessy, R. P. Caputo, D. J. Kereiakes, D. O. Williams, P. S. Teirstein, J. L. Jaeger, and R. E. Kuntz, "Sirolimus-eluting stents versus standard stents in patients with stenosis in a native coronary artery," New England Journal of Medicine **349**, 1315–1323 (2003) (cit. on p. 13).

[42] E. Grube, S. Silber, K. E. Hauptmann, R. Mueller, L. Buellesfeld, U. Gerckens, and M. E. Russell, "TAXUS I. Six- and twelve-month results from a randomized, double-blind trial on a slow-release paclitaxel-eluting stent for de novo coronary lesions," Circulation **107**, 38–42 (2003) (cit. on p. 13).

[43] R. Piccolo, G. G. Stefanini, A. Franzone, E. Spitzer, S. Blöchlinger, D. Heg, P. Jüni, and S. Windecker, "Safety and efficacy of resolute zotarolimus-eluting stents compared with everolimus-eluting stents," Circulation: Cardiovascular Interventions **8**, 1–8 (2015) (cit. on p. 13).

[44] H. Gu, K. Hua, W. Li, Y. Wang, and J. Yang, "Safety and efficacy of everolimus-eluting stent versus zotarolimus-eluting stent: A meta-analysis of randomized controlled clinical trials and observational studies," International Journal of Cardiology **201**, 552–560 (2015) (cit. on p. 13).

[45] S. Garg, and P. W. Serruys, "Coronary stents: Looking forward," Journal of the American College of Cardiology **56**, S43–S78 (2010) (cit. on p. 13).

[46] H. M. Nef, J. Wiebe, N. Foin, F. Blachutzik, O. Dörr, S. Toyloy, and C. W. Hamm, "A new novolimus-eluting bioresorbable coronary scaffold: Present status and future clinical perspectives," International Journal of Cardiology **227**, 127–133 (2017) (cit. on p. 13).

[47] R. Piccolo, A. Nicolino, and G. B. Danzi, "The Nobori biolimus-eluting stent: Update of available evidence," Expert Review of Medical Devices **11**, 275–282 (2014) (cit. on p. 13).

[48] Y. S. Keh, J. Yap, K. K. Yeo, T. H. Koh, and E. Eeckhout, "Clinical outcomes of bioresorbable scaffold in coronary artery disease: A systematic literature review," Journal of Interventional Cardiology **29**, 57–69 (2016) (cit. on p. 13).

[49] D. Jackson, D. Tong, and J. Layland, "A review of the coronary applications of the drug coated balloon," International Journal of Cardiology **226**, 77–86 (2017) (cit. on p. 13).

[50] C. Roiron, P. Sanchez, A. Bouzamondo, P. Lechat, and G. Montalescot, "Drug eluting stents: An updated meta-analysis of randomised controlled trials," Heart **92**, 641–649 (2006) (cit. on p. 14).

[51] B. E. Claessen, J. P. Henriques, F. A. Jaffer, R. Mehran, J. J. Piek, and G. D. Dangas, "Stent thrombosis: A clinical perspective," JACC: Cardiovascular Interventions **7**, 1081–1092 (2014) (cit. on p. 14).

[52] R. D. Anderson, and C. J. Pepine, "Coronary angiography," Circulation **127**, 1760–1762 (2013) (cit. on p. 14).

[53] S. Bangalore, and D. L. Bhatt, "Coronary intravascular ultrasound," Circulation **127**, e868–e874 (2013) (cit. on p. 14).

[54] J. M. McCabe, and K. J. Croce, "Optical coherence tomography," Circulation **126**, 2140–2143 (2012) (cit. on p. 14).

[55] D. M. Pozar, *Microwave engineering* (Wiley, New York, 2011) (cit. on p. 14).

[56] A. V. Vorst, A. Rosen, and Y. Kotsuka, *RF/ microwave interaction with biological tissues* (Wiley, New York, 2006) (cit. on p. 14).

[57] E. Y. Chow, M. M. Morris, and P. P. Irazoqui, "Implantable RF medical devices: the benefits of high-speed communication and much greater communication distances in biomedical applications," IEEE Microwave Magazine **14**, 64–73 (2013) (cit. on p. 14).

[58] K. Takahata, and Y. B. Gianchandani, "Batch mode micro-electro-discharge machining," Journal of Microelectromechanical Systems **11**, 102–110 (2002) (cit. on p. 14).

[59] ——, "A planar approach for manufacturing cardiac stents: Design, fabrication, and mechanical evaluation," Journal of Microelectromechanical Systems **13**, 933–939 (2004) (cit. on p. 14).

[60] K. Takahata, Y. B. Gianchandani, and K. D. Wise, "Micromachined antenna stents and cuffs for monitoring intraluminal pressure and flow," Journal of Microelectromechanical Systems **15**, 1289–1298 (2006) (cit. on pp. 14, 15, 17).

[61] D. Lappin, A. R. Mohammadi, and K. Takahata, "An experimental study of electrochemical polishing for micro-electro-discharge-machined stainless-steel stents," Journal of Materials Science: Materials in Medicine **23**, 349–356 (2012) (cit. on p. 15).

[62] A. R. Mohammadi, M. S. M. Ali, D. Lappin, C. Schlosser, and K. Takahata, "Inductive antenna stent: Design, fabrication and characterization," Journal of Micromechanics and Microengineering **23**, 025015 (2013) (cit. on p. 15).

[63] X. Chen, D. Brox, B. Assadsangabi, Y. Hsiang, and K. Takahata, "Intelligent telemetric stent for wireless monitoring of intravascular pressure and its in vivo testing," Biomedical Microdevices **16**, 745–759 (2014) (cit. on pp. 15, 17).

[64] D. S. Brox, X. Chen, S. Mirabbasi, and K. Takahata, "Wireless telemetry of stainless-steel-based smart antenna stent using a transient resonance method," IEEE Antennas and Wireless Propagation Letters **15**, 754–757 (2016) (cit. on p. 15).

[65] Y. Luo, X. Chen, M. Dahmardeh, and K. Takahata, "RF-powered stent with integrated circuit breaker for safeguarded wireless hyperthermia treatment," Journal of Microelectromechanical Systems **24**, 1293–1302 (2015) (cit. on p. 15).

[66] Y. Luo, M. Dahmardeh, X. Chen, and K. Takahata, "A resonant-heating stent for wireless endohyperthermia treatment of restenosis," Sensors and Actuators A: Physical **236**, 323–333 (2015) (cit. on p. 15).

[67] E. Y. Chow, B. L. Beier, A. Francino, W. J. Chappell, and P. P. Irazoqui, "Toward an implantable wireless cardiac monitoring platform integrated with an FDA-approved cardiovascular stent," Journal of Interventional Cardiology **22**, 479–487 (2009) (cit. on pp. 15, 17).

[68] E. Y. Chow, Y. Ouyang, B. Beier, W. J. Chappell, and P. P. Irazoqui, "Evaluation of cardiovascular stents as antennas for implantable wireless applications," IEEE Transactions on Microwave Theory and Techniques **57**, 2523–2532 (2009) (cit. on p. 16).

[69] E. Y. Chow, A. L. Chlebowski, S. Chakraborty, W. J. Chappell, and P. P. Irazoqui, "Fully wireless implantable cardiovascular pressure monitor integrated with a medical stent," IEEE Transactions on Biomedical Engineering **57**, 1487–1496 (2010) (cit. on pp. 16, 17).

[70] K. M. Musick, A. C. Coffey, and P. P. Irazoqui, "Sensor to detect endothelialization on an active coronary stent," BioMedical Engineering OnLine **9**, 67 (2010) (cit. on p. 16).

[71] C. Occhiuzzi, G. Contri, and G. Marrocco, "Design of implanted RFID tags for passive sensing of human body: The STENTag," IEEE Transactions on Antennas and Propagation **60**, 3146–3154 (2012) (cit. on pp. 16, 17).

2

Microwave spectrometry

The principle of microwave spectrometry is the analysis of the interaction between an incident electromagnetic wave and a highly conductive object like a vascular stent. Any stent with a metallic scaffold would scatter an electromagnetic wave in a particular manner depending on the frequency and the incidence angle of the microwave fields. We will see that the said scattering is enhanced at characteristic frequencies for which the electrons from the stent alloy establish standing waves of current that resonate at microwave frequencies (similar to a guitar string that resonates at particular sound frequencies). The setup we have developed along this thesis works by scanning the frequency and the incidence angle of the microwave fields while looking for these resonances. In this chapter we will introduce the operational basis of our microwave spectrometry equipment. We will show how the frequencial and angular information obtained in a typical stent characterization can be combined in a single two-dimensional chart, and how we identify therein the characteristic resonance frequencies of stents at a glance.

2.1 Setup and data acquisition

In this section we will present our MWS setup and some data analysis methods that would be recurrently used along the following chapters. The whole equipment comprises two separated parts that, when properly combined, make possible the sweep of the frequency and the incidence angle of the microwave fields sent to the stent under

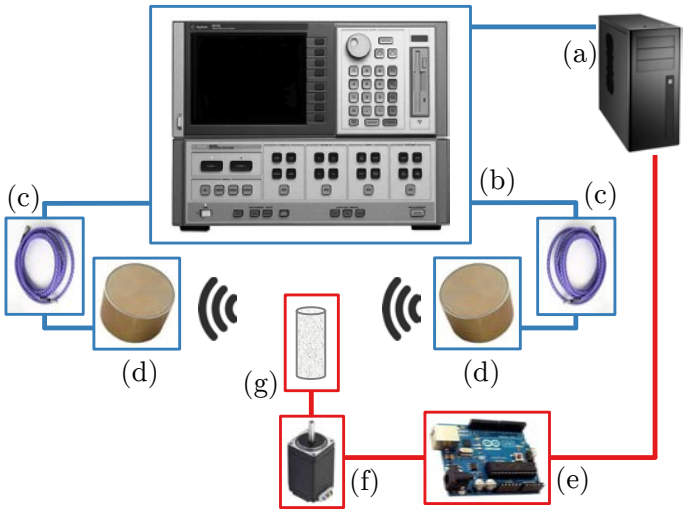

Figure 2.1: Block diagram showing the frequency- and the angle-sweeping components of the MWS setup used to characterize stents in free space conditions (blue and red wires and boxes, respectively). The elements comprising the whole setup are: Control computer (a); VNA (b); coaxial feedlines (c); microwave antennas (d); single board micro-controller (e); stepper motor (f); and sample holder (g).

study. Figure 2.1 provides a block diagram of the apparatus used along this thesis. On the one hand, blue wires and boxes in this figure highlight the frequency-sweeping components of our equipment. They consists of a two-port vector network analyzer[1] (VNA) with a couple of cavity-backed spiral antennas[2] connected via semi-flexible coaxial feedlines[3]. On the other hand, red wires and boxes in this figure denote the angle-sweeping components. They are made up of a handmade cylinder of expanded polystyrene mounted on a two hundred steps unipolar stepping motor[4] which is controlled by using a commercial single-board micro-controller[5].

[1] HP 8510C, Agilent Technologies, Santa Clara, CA, USA.
[2] JXTXLX-20180, Chengdu AINFO, Chengdu, Sichuan, China.
[3] 3GW40-0TD01D02048.0, W.L. Gore & Associates, Newark, DE, USA.
[4] ST2818M1006-B, Nanotec Electronic, Feldkirchen, Munich, Germany.
[5] Arduino® Uno, Interaction Design Institute Ivrea, Ivrea, Torino, Italy.

2.1.1 Sweeping the microwave frequency

The VNA is the cornerstone of the frequency-sweeping branch of our MWS setup. As it is usual among the VNAs from the 90s, four separated instruments form the whole equipment. These instruments are the signal generator, the test set, the receiver and the display. The signal generator provides the test stimulus required by the test set, and this redirects the signal to its output port. In order to bring the stimulus to the stent under study, a first antenna is connected to the output port. This emitter antenna transforms the signal into a propagating microwave electromagnetic field that is able to travel through free space and reach the stent. After the interaction between the incident electromagnetic wave and the stent, a second antenna collects the scattered electromagnetic wave and routes it towards the input port of the test set via another feedline. Then, the test set brings the resulting signal towards the receiver, which in turn measures its magnitude and phase. Finally, the display allows to express the signal measured in an easy way for being interpreted by the operator.

This portion of the setup is able to provide the four scattering-parameters between the ports of the VNA as a function of the microwave frequency, f. The said coefficients, also referred as S-parameters, are the reverse/forward voltage gains and the input/output voltage reflection coefficients, S_{12}, S_{21}, S_{11} and S_{22}, respectively. Therefore, just placing a stent between the antennas we can acquire any of its scattering-parameters within the desired spectral range, which is usually set between 2.00 GHz and 18.00 GHz with a resolution of 0.02 GHz. All the experiments performed along this thesis were carried out in free space conditions, setting the antennas at a constant separation of 10.0 cm. Similarly, the center of the stent under characterization was always placed right in the midpoint of the line joining the antennas (optical axis). This symmetrical configuration ensures the equivalence between input or output voltage reflection coefficient spectra, $S_{11}(f) \simeq S_{22}(f)$, and also between reverse and forward voltage gain spectra, $S_{12}(f) \simeq S_{21}(f)$. In any case, all measurements in this thesis were based on the acquisition of $S_{21}(f)$ for a given stent.

As an example, Figure 2.2a shows the typical shape for the forward voltage gain spectra obtained with and without a stent

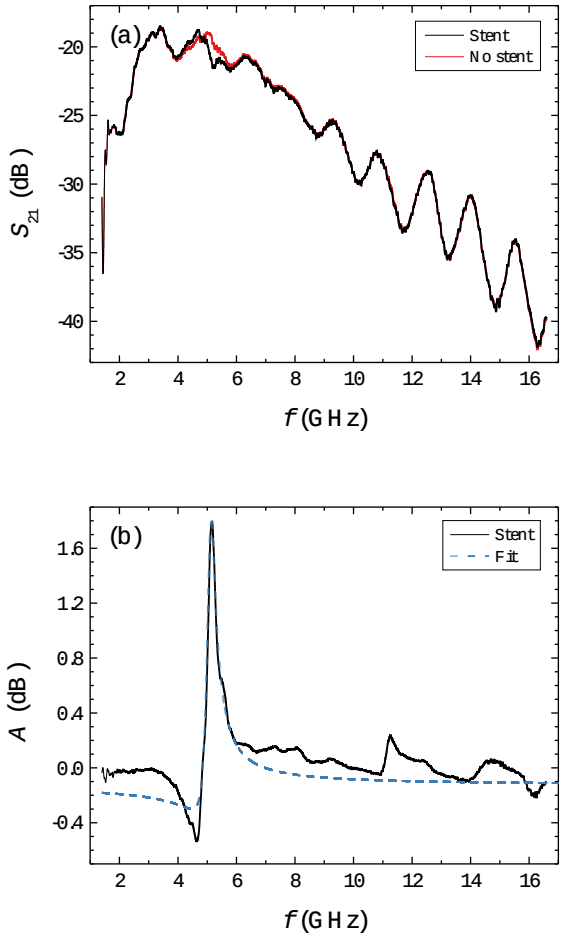

Figure 2.2: (a) Forward voltage gain as a function of the microwave frequency, $S_{21}(f)$, obtained with and without a Medtronic Driver Sprint® bare-metal stent placed in the sample holder (black and red solid lines, respectively). The stent was expanded up to $p = p_{\text{nom}} = 9.0 \pm 0.5$ atm to reach its nominal size 12 mm $\times$ 2.25 mm. (b) Absorbance spectrum of the same stent, $A(f)$, and the corresponding least squares fit obtained from the fitting function of Equation 2.2 (black solid and blue dashed lines, respectively).

placed between the antennas. The stent used was a Medtronic Driver Sprint® bare-metal stent[6] with nominal length, $\ell_{\text{nom}} = 12$ mm, and nominal diameter, $d_{\text{nom}} = 2.25$ mm [1] (hereinafter we will designate a given nominal size as $\ell_{\text{nom}} \times d_{\text{nom}}$). Notice how the signal level of both $S_{21}^{\text{st}}(f)$ and $S_{21}^{\text{no st}}(f)$ degrades as the frequency goes below 2 GHz and above 16 GHz. This is due to the nominal operating window of our antennas, whose optimum performance lies within this frequency range. At first glance, it seems there are no differences between the two $S_{21}(f)$ spectra, but if we look at the traces closely we should notice the presence of some distinctive structure around 5 GHz. We can highlight the differences between $S_{21}^{\text{st}}(f)$ and $S_{21}^{\text{no st}}(f)$ just by calculating the absorbance spectrum:

$$A(f) = S_{21}^{\text{st}}(f) - S_{21}^{\text{no st}}(f). \tag{2.1}$$

Figure 2.2b, represents such absorbance spectrum along with the corresponding fitting function obtained from a non-linear least squares fit algorithm[7]. Notice that the subtle structure around 5 GHz previously shown in Figure 2.2a, is now revealed as a true resonance-like feature which can be easily characterized just fitting a suitable function.

Due to its recurrent utilization along the following chapters, we find appropriate make a parenthesis to describe the resonance-like fitting function used to quantify resonance frequencies [2]. The stent resonances in our $A(f)$ spectra can be fitted combining a couple of properly weighted Lorentzian functions plus an additive constant:

$$\mathcal{A}(f) = \mathcal{A}_{\text{a}}\mathcal{L}_{\text{a}}(f) + \mathcal{A}_{\text{s}}\mathcal{L}_{\text{s}}(f) + \mathcal{A}_0, \tag{2.2}$$

where $\mathcal{A}_{\text{a}}$ and $\mathcal{A}_{\text{s}}$ represent the amplitudes of each Lorentzian term and, as mentioned before, $\mathcal{A}_0$ is just an additive constant which sets the ordinates. Functions $\mathcal{L}_{\text{a}}(f)$ and $\mathcal{L}_{\text{s}}(f)$ denote the antisymmetric and the symmetric Lorentzian curves, respectively:

$$\mathcal{L}_{\text{a}}(f) = \frac{(f - f_0)\frac{\omega}{2}}{(f - f_0)^2 + (\frac{\omega}{2})^2}, \tag{2.3a}$$

$$\mathcal{L}_{\text{s}}(f) = \frac{(\frac{\omega}{2})^2}{(f - f_0)^2 + (\frac{\omega}{2})^2}. \tag{2.3b}$$

[6] Medtronic, Minneapolis, NE, USA.
[7] Matlab® R2008b, The MathWorks, Natick, MA, USA.

Here, the parameters f_0 and ω are the central frequency and the bandwidth of the resonance to fit. In Figure 2.3 we have plotted both Lorentzians for a fixed f_0 and three arbitrary ω/f_0 ratios just to give an insight of their general shape. In sum, our full fitting function can be thus generally expressed as

$$\mathcal{A}(f) = \mathcal{A}_{\mathrm{a}} \frac{(f-f_0)\frac{\omega}{2}}{(f-f_0)^2+(\frac{\omega}{2})^2} + \mathcal{A}_{\mathrm{s}} \frac{(\frac{\omega}{2})^2}{(f-f_0)^2+(\frac{\omega}{2})^2} + \mathcal{A}_0, \qquad (2.4)$$

and therefore, our fitting algorithm has five parameters to determine in order to characterize a given stent resonance: $\mathcal{A}_{\mathrm{a}}$, $\mathcal{A}_{\mathrm{s}}$, $\mathcal{A}_0$, f_0 and ω. As an example, Table 2.1 provides these parameters for the $\mathcal{A}(f)$ fitting function previously shown in Figure 2.2b.

f_0 (GHz)	ω (GHz)	$\mathcal{A}_{\mathrm{s}}$ (dB)	$\mathcal{A}_{\mathrm{a}}$ (dB)	$\mathcal{A}_0$ (dB)
5.080±0.009	0.37±0.02	1.14±0.08	1.76±0.07	−0.13±0.03

Table 2.1: Parameters of the fitting function previously shown in Figure 2.2b ($r^2 = 0.98$). The fitting window was restricted between $f_0 - 0.9$ GHz and $f_0 + 1.0$ GHz.

Notice how these values turn out to be reasonable just inspecting the shape of the resonance from Figure 2.2b. First, its corresponding fit should present both antisymmetric and symmetric Lorentzian parts, with a slightly dominating antisymmetric contribution ($\mathcal{A}_{\mathrm{a}} \gtrsim \mathcal{A}_{\mathrm{s}} > 0$). Additionally, since the amplitude of the resonance raises up to 1.7 dB, the values of $\mathcal{A}_{\mathrm{a}}$ and $\mathcal{A}_{\mathrm{s}}$ shall fall in this order of magnitude ($\mathcal{A}_{\mathrm{a}} \simeq 1$ dB $\simeq \mathcal{A}_{\mathrm{s}}$). In principle we expect a small value for the additive constant ($\mathcal{A}_0 \simeq 0$) and numbers around 5 GHz and 1 GHz for f_0 and ω, respectively.

2.1.2 Sweeping the incidence angle

The frequencial and angular scanning portions of our equipment must be coordinated to make MWS work properly. This is achieved using an instrument control/data acquisition program[8] which commands at the same time the VNA and the stepping motor. On the one hand, the VNA is connected to the computer by means of a GPIB/USB

[8] LabVIEW 8.5, National Instruments, Austin, TX, USA.

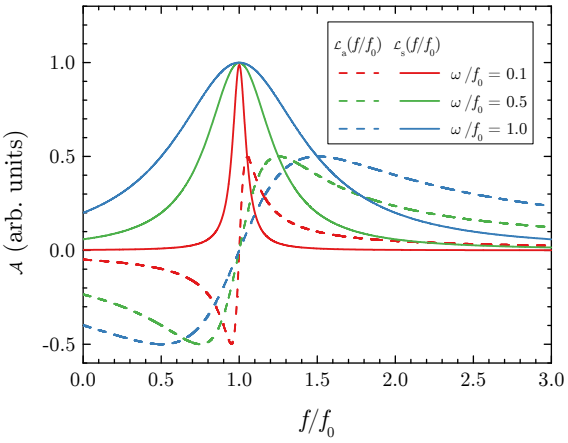

Figure 2.3: Symmetric Lorentzian function (solid lines) and anti-symmetric Lorentzian function (dashed lines) versus f/f_0 for three different ω/f_0 ratios, which are 0.1, 0.5 and 1.0 (red, green and blue lines, respectively). The central frequency of the resonance has been fixed at $f_0 = 1.0$ (in arbitrary units) in all cases.

(general purpose interface bus/universal serial bus) interface[9]. On the other hand, a homemade stepper circuit links the rotating drive with the single-board micro-controller which in turn is connected to the same computer via USB. In Figures 2.4a and 2.4b we provide respectively a schematic and a picture showing the wiring between the micro-controller and the motor. Four digital outputs from the micro-controller are connected to the base terminal of four BJT (bipolar junction transistor) switches (T_1 to T_4) through four 1.00 kΩ-resistors (R_1 to R_4). Each transistor works as an electronic switch in grounded-emitter configuration. The collector terminal of each transistor links with one of the four coil ends in the motor. Transistors T_1 and T_2 control the ends of the first coil (gray and green wires), while T_3 and T_4 do the same for the ends of the second coil (red and blue wires). Finally the common terminals of both coils are fed with a 5 V voltage.

Therefore, the stepping drive transforms our handmade cylinder of expanded polystyrene in a rotating sample holder when is

[9] 82357B, Agilent Technologies, Santa Clara, CA, USA.

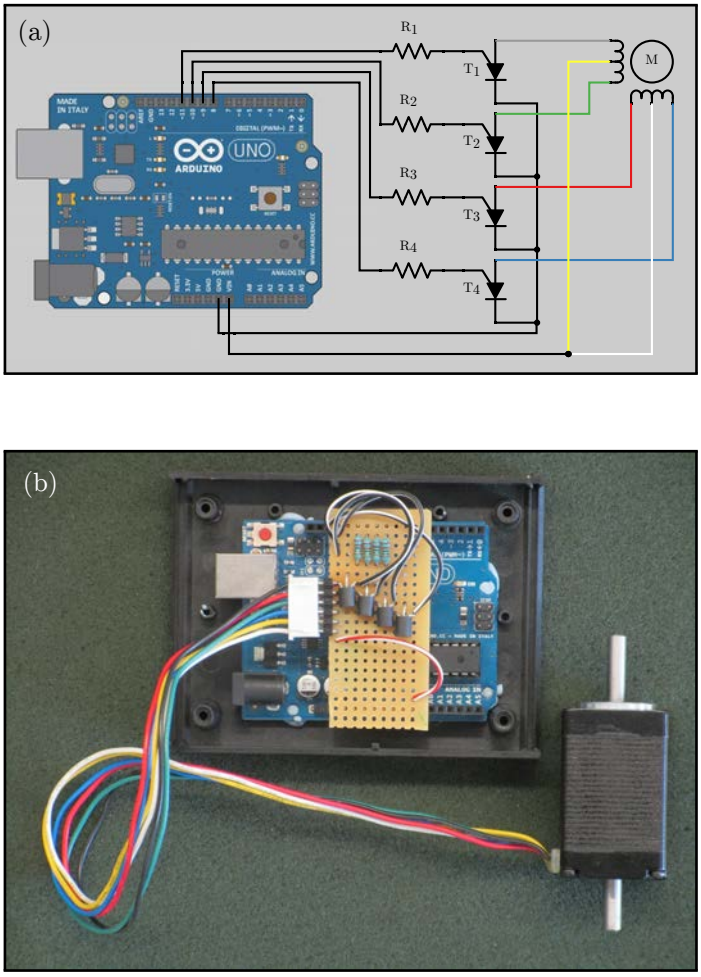

Figure 2.4: (a) Circuit schematic showing the homemade interconnections between the single-board micro-controller and the unipolar stepping motor. This circuit enables computer control of the stepper drive via a universal serial bus. (b) Picture showing the actual look of the circuit.

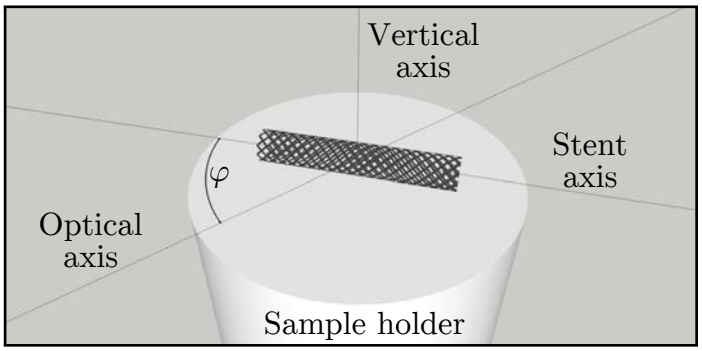

Figure 2.5: Sketch of a stent placed on the sample holder during its MWS characterization. Optical and vertical axes are perpendicular along the entire process, whereas the stent axis rotates around the vertical axis describing the azimuthal angle, φ.

mounted under it. This column-motor assemblage allows to modify the incidence angle of the microwave fields when these reach the stent under study. The platform rotates the stent around the azimuthal angle, φ, formed by the stent axis and the optical axis, enabling a full 360.0° azimuthal scan in small angular steps of 1.8°. Figure 2.5 provides a sketch to see a graphical representation of φ and its related axes. Thus, through the synchronous actions of frequency- and angle-sweeping, the MWS setup is able to provide the forward voltage gain spectra as a function of the azimuthal angle, $S_{21}^{\mathrm{st}}(f, \varphi)$. We can then compute the corresponding absorbance spectra as a function of φ as described by Equation 2.1. Note that prior acquisition of a reference forward voltage gain without stent is required:

$$A(f, \varphi) = S_{21}^{\mathrm{st}}(f, \varphi) - S_{21}^{\mathrm{no\ st}}(f). \tag{2.5}$$

Finally, the resulting $A(f, \varphi)$ data set, the so-called absorbance diagram, can be represented in a single gray scale chart using graphing software[10]. As an example, Figure 2.6 presents the $A(f, \varphi)$ chart of a stent in order to illustrate a typical MWS characterization. The stent used was a Medtronic Integrity® bare-metal stent[11] with nominal size 26 mm × 2.50 mm [3].

[10] OriginPro 8 SRO, OriginLab, Northampton, MA, USA.
[11] Medtronic, Minneapolis, NE, USA.

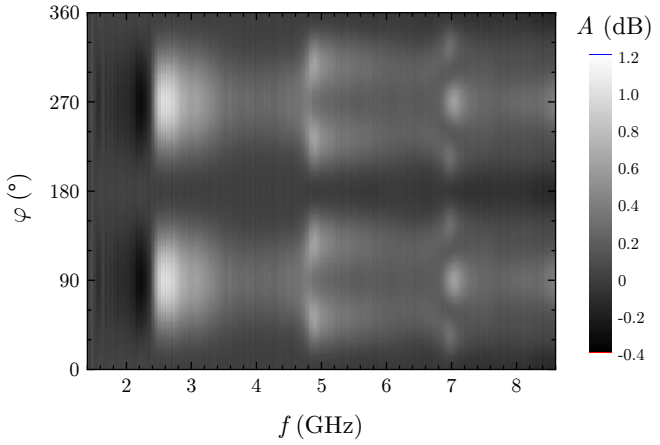

Figure 2.6: Absorbance diagram as a function of the microwave frequency and the azimuthal angle, $A(f, \varphi)$, for a Medtronic Integrity® bare-metal stent with nominal size 26 mm × 2.50 mm acquired in free space conditions. The stent was overexpanded up to $p = 22.0 \pm 0.5$ atm.

2.2 Reading a typical absorbance diagram

The combination of angular and frequencial information within the $A(f, \varphi)$ chart allows us to discern what is a true stent resonance and what is not, but this analysis may result a bit tricky at first sight. Since absorbance diagrams will be extensively used to illustrate our results along the following chapters, it is worth devoting some time to introduce their interpretation.

Figure 2.7a shows the same $A(f, \varphi)$ diagram already presented in Figure 2.6. Each horizontal line in this chart (isoangular projection) represents the absorbance spectrum for a given angle. Isoangulars at $\varphi = 0°$, 45° and 90° appear highlighted as overlayed horizontal color lines (red, green and blue, respectively). Figures 2.7b to 2.7d trace their corresponding profiles. Notice how the profile at $\varphi = 90°$ from Figure 2.7d shows a resonance whose precise frequency can be extracted, as previously established, at $f_1 = 2.446 \pm 0.007$ GHz. Additionally, another resonance can be seen at higher frequency, at $f_3 = 7.014 \pm 0.004$ GHz. Both resonances are spotted again at the

$\varphi = 45°$ profile from Figure 2.7c, but now with a reduced amplitude. In this same profile we also intuit a resonance which was not present in the previous $\varphi = 90°$ profile, at $f_2 = 4.828 \pm 0.006$ GHz. In Figure 2.7b we finally observe that all three resonances eventually disappear in the $\varphi = 0°$ profile, which becomes almost flat.

A better insight of the come-and-go behavior exhibited by these resonances is reached moving to an isofrequencial reading of the same $A(f, \varphi)$ chart, this time in Figure 2.8a. Each vertical line (isofrequencial projection) from this diagram represents the absorbance angular pattern at a certain frequency. Isofrequencials near f_1, f_2 and f_3 appear emphasized as overlayed vertical color lines (red, green and blue, respectively). Figures 2.8b to 2.8d trace their corresponding profiles. Notice how the profile of f_1 shown in Figure 2.8b exhibits two maxima at 90° and 270°, which means that the amplitude of the first resonance is specially reinforced when the incidence of the electromagnetic wave is normal with respect to the stent axis. However, the profile of f_2 shown in Figure 2.8c exhibits four maxima around 45°, 135°, 225° and 315°. Therefore, the amplitude of the second resonance is enhanced when the incidence is oblique with respect to the stent axis. Finally, the profile of f_3 presented in Figure 2.8d is more complicated, this time with six maxima located around 30°, 90°, 150°, 210°, 270° and 330°.

Such patterns are better identified when the isofrequencial profiles are plotted in polar form, as in Figure 2.9. Notice how the angular pattern is bilobular for f_1, tetralobular for f_2 and hexalobular for f_3 (red, green and blue, respectively). In general, the nth-order resonance, f_n, should exhibit a $2n$-lobed angular pattern. Thus we can determine the order of a given resonance frequency just inspecting the associated $A(\varphi)$ pattern. We will see that all stents characterized throughout this thesis show exactly these same general features regardless of their nominal size and even their particular brand or model.

Although not show here, higher resonances exhibit even more complex dependences, like octolobular patterns for the fourth resonance. In fact, we managed to identify up to sixth order resonances in some isoangular profiles, but with decreasing amplitudes. Since the fundamental resonance frequency always exhibits the highest amplitude, we will focus on its characterization along the following

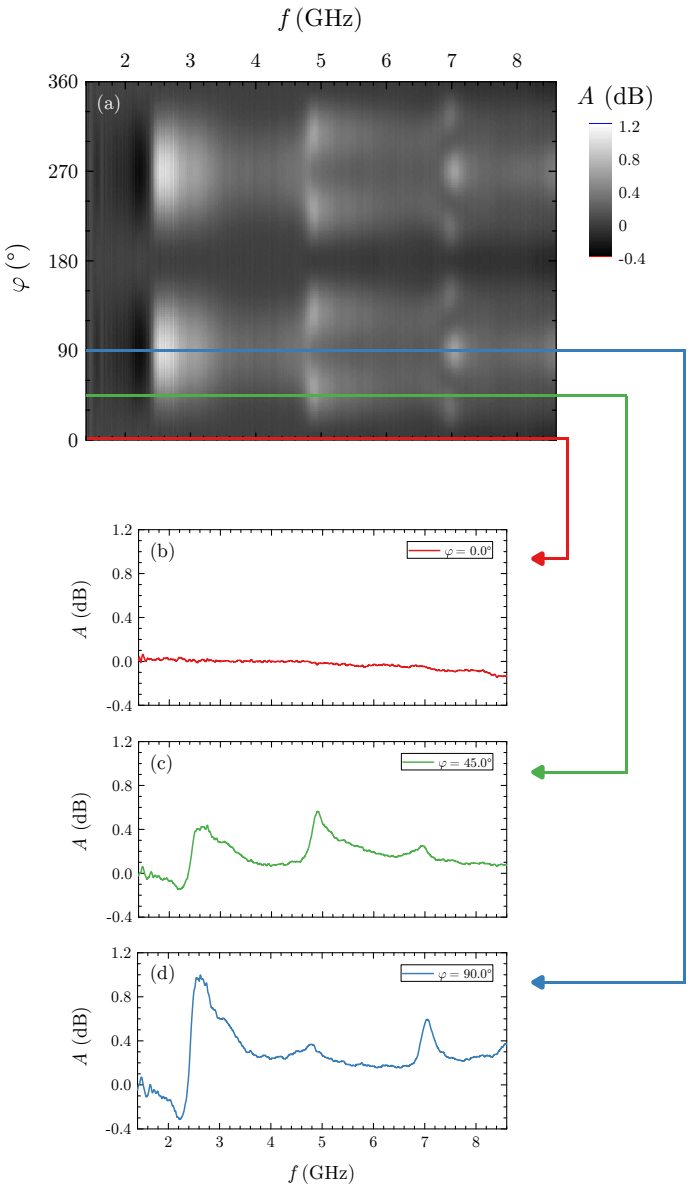

Figure 2.7: Frequencial interpretation of a MWS characterization. (a) Absorbance diagram, $A(f, \varphi)$, for a Medtronic Integrity® bare-metal stent with nominal size 26 mm × 2.50 mm. The stent was overexpanded up to $p = 22.0 \pm 0.5$ atm. (b to d) Isoangular projections of the $A(f, \varphi)$ chart at $\varphi = 0°$ (red), 45° (green) and 90° (blue).

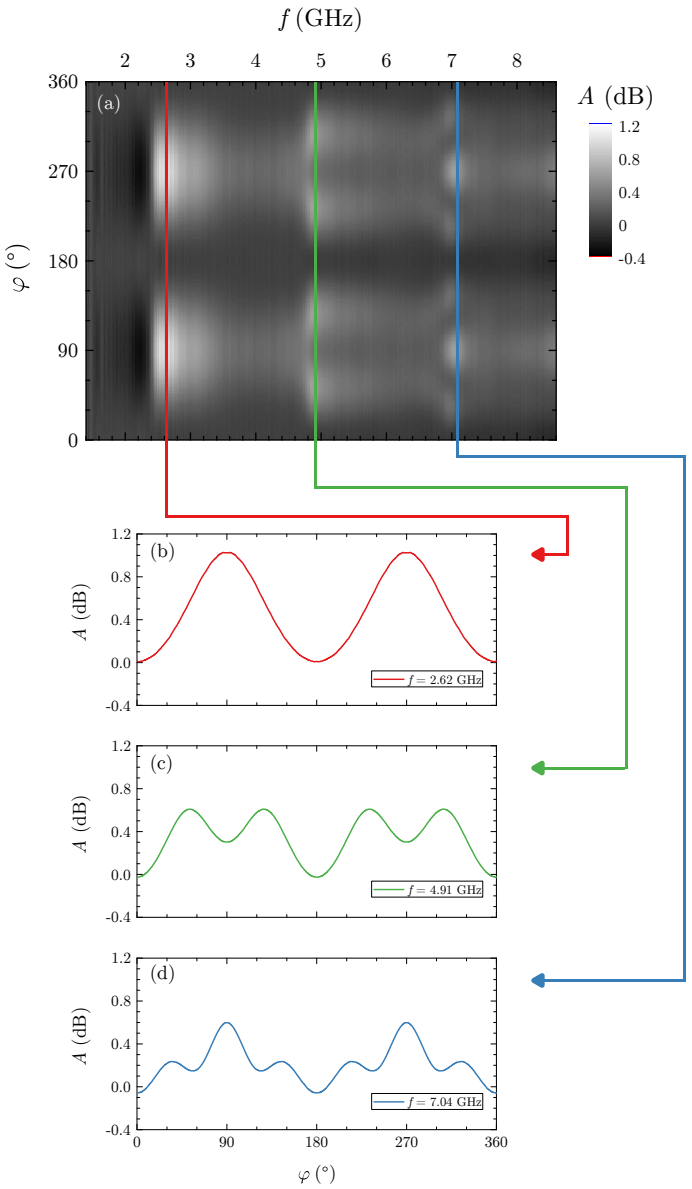

Figure 2.8: Angular interpretation of a MWS characterization. (a) Absorbance diagram, $A(f, \varphi)$, for a Medtronic Integrity® bare-metal stent with nominal size 26 mm × 2.50 mm. The stent was expanded up to $p = 22.0 \pm 0.5$ atm. (b to d) Isofrequencial projections of the $A(f, \varphi)$ chart at $f = 2.62$ GHz (red), 4.91 GHz (green) and 7.04 GHz (blue).

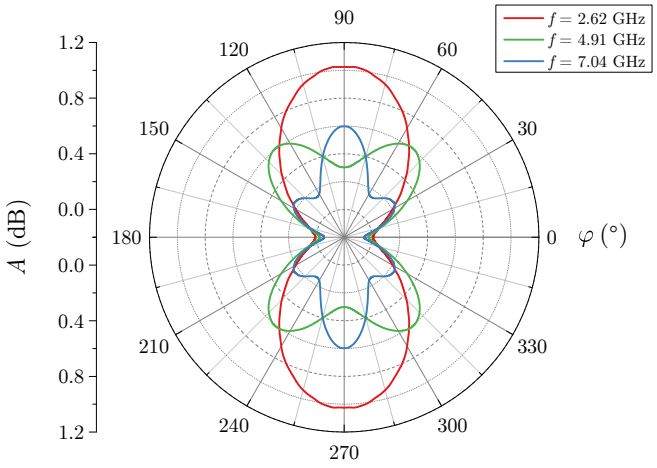

Figure 2.9: Same isofrequencial projections shown in Figure 2.8b to 2.8d represented in polar form. These isofrequencials are $f = 2.62$ GHz, 4.91 GHz and 7.04 GHz (red, green and blue, respectively).

chapters. We will see that the monitoring of f_1 is enough to illustrate our results because it already contains all the information we need.

2.3 Conclusions

Along the first half of this procedural chapter we have described the operational basis of our microwave spectrometry setup. We have shown how the angle/frequency data retrieved from a typical stent characterization can be encapsulated in a single two-dimensional chart that we have called absorbance diagram. In the second part of the chapter, we have acquainted the reader with these $A(f, \varphi)$ diagrams. We have introduced how we identify and evaluate stent characteristic resonance frequencies found in such $A(f, \varphi)$ charts by means of their isofrequencial and isoangular analysis. In particular we have highlighted that the nth-order resonance, f_n, exhibits a $2n$-lobed angular pattern. The later would be crucial along the following chapters, because it will allow us to identify the order of a given resonance frequency just by inspecting the associated angular pattern.

References

[1] *Driver sprint rapid exchange coronary stent system, Instructions for use*, Revision B (2011) (cit. on p. 33).

[2] F. V. Hunt, "Resonance versus resonant," The Journal of the Acoustical Society of America **50**, 435–435 (1971) (cit. on p. 33).

[3] *Integrity rapid exchange coronary stent system, Instructions for use*, Revision 1A (2011) (cit. on p. 37).

3

Microwave resonances in stents

In the previous chapter we have presented our MWS setup, showing how their frequency- and angle-scanning parts work together to obtain the absorbance diagram of a given stent. We have also introduced how to identify and quantify the characteristic resonance frequencies of stents found in such charts. To this end, we have just presented measurements for a couple of representative stents. In contrast, in the current chapter we will characterize a large number of stents having a wide variety of sizes in order to find a link between the resonance frequencies of stents and their corresponding geometrical magnitudes (stent length and diameter). The data retrieved using this empirical approach will serve us to establish a straightforward theoretical framework which will help us to better understand the scattering of microwave electromagnetic waves by stents. Eventually, this half-theoretical half-empirical model will enable us to link the characteristic resonance frequencies of stents with their structural integrity and their surrounding medium.

3.1 Stent description

We worked with sixty coronary stents of two different models: the Medtronic Driver Sprint® bare-metal stent[1] (MDS) and the Medtronic Endeavor Sprint® zotarolimus-eluting stent[2] (MES). The manufac-

[1] Medtronic, Minneapolis, NE, USA.
[2] Medtronic, Minneapolis, NE, USA.

MDS	ℓ_{nom} (mm)							
d_{nom} (mm)	8	9	12	14	15	18	24	30
2.25	☑		☑	☑		□	□	□
2.50	☑		☑*	☑		☑	☑	□
2.75	□		☑	☑		☑	☑	□
3.00		☑	□		□	☑	□	□
3.50		☑	☑		☑	☑	□	☑
4.00		☑	□		☑	☑	☑	☑
4.50		☑	☑		☑	☑	☑	☑

MES	ℓ_{nom} (mm)							
d_{nom} (mm)	8	9	12	14	15	18	24	30
2.25	☑		☑	☑		□	☑	☑
2.50	□		☑	☑		☑	☑	☑
2.75	□		☑	□		□	☑	□
3.00		☑	☑		☑	☑	☑	☑
3.50		☑	☑		☑	☑	☑	☑
4.00		□	☑		☑	☑	☑	☑

Table 3.1: Set of commercially available nominal sizes for the MDS and MES stent models. Horizontal and vertical numbers indicate the corresponding nominal length (ℓ_{nom}) and nominal diameter (d_{nom}), respectively. Checked boxes (☑) denote the nominal sizes at our disposal for analysis, whilst unchecked boxes (□) represent nominal sizes that were not at our disposal. The asterisked nominal size (☑*) was available twice since we had two copies of the corresponding stent.

turer offers a range of nominal lengths, ℓ_{nom}, and nominal diameters, d_{nom}, certain combinations of which comprise the full set of commercially available nominal sizes for each stent model. Table 3.1 shows the corresponding complete assortments. Checked boxes (☑) in this table denote nominal sizes at our disposal for analysis, whilst unchecked boxes (□) represent nominal sizes that were not at our disposal in spite of being commercially available. We had 30 out of 42 nominal sizes for the MDS (71%), and 29 out of 36 (81%) for the MES, representing around three quarters of the full set.

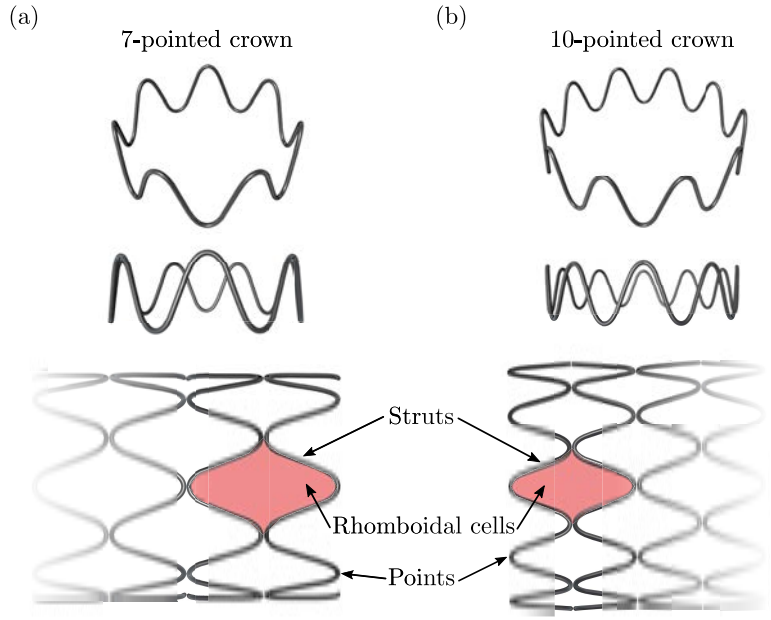

Figure 3.1: Graphical representation of the sinusoidal modular elements forming the MDS and MES stent models. The thinner stents ($d_{\text{nom}} = 2.25$, 2.50 and 2.75 mm) are assembled with seven-pointed crowns with 1.2 mm-long struts (a), whilst the thicker stents ($d_{\text{nom}} = 3.00$, 3.50, 4.00 and 4.50 mm) are assembled using ten-pointed crowns with 1.0 mm-long struts (b). Red areas highlight the characteristic rhombus-shaped cells delimited by adjacent crowns.

The sketches from Figure 3.1 illustrate the characteristic modular structure that constitutes our MDS and MES stents. Both models are formed by a certain number of individual building blocks shaped as sinusoidal crowns. Medtronic assembles each block using a 0.091-mm-thick round wire of industry standard F562-13 nickel-cobalt-chromium-molybdenum alloy (Ni 35%, Co 35%, Cr 20%, Mo 10%) [1]. The manufacturer states that this alloy also contains trace elements like iron, titanium, manganese, silicon and carbon. Medtronic commercial flip charts provide upper bounds for their concentrations which never exceed 1% (Fe 1.0%, Ti 1.0%, Mn 0.15%, Si 0.15%, C 0.025%) [2]. Every crown has several straight wire segments known as struts that in groups of four delimit rhombus-shaped cells (two pairs of struts from adjacent crowns). In general, the quantity of crowns of

a given stent varies according to ℓ_{nom} and, thus, the longer a stent is the more crowns it will present. However, crowns assembling thinner stents (d_{nom} = 2.25, 2.50 and 2.75 mm), are slightly longer than those forming thicker stents (d_{nom} = 3.00, 3.50, 4.00 and 4.50 mm). Namely, in the first case crowns are 1.2 mm long whilst in the second case are only 1.0 mm long. This means that for a same ℓ_{nom}, thinner stents have fewer crowns. In addition, long crowns are seven-pointed whilst short crowns turn out to be ten-pointed.

In order to maintain their longitudinal integrity, all building blocks forming both stent models are held together by means of a helical laser-fused welding pattern. Just three distinct motifs are found depending on d_{nom} and without regard for the precise value of ℓ_{nom}. This motif is mono-helical for thin calibers (d_{nom} = 2.25, 2.50 and 2.75 mm), bi-helical for mid calibers (d_{nom} = 3.00 and 3.50 mm) and tri-helical for thick calibers (d_{nom} = 4.00 and 4.50 mm). Figures 3.2, 3.3 and 3.4 depict planar representations of these three welding patterns. Notice how the corresponding weld points trace a single helix (red dots in Figure 3.2), a double helix (red and green dots in Figure 3.3) and a triple helix (red, green and blue dots in Figure 3.4) in each case. Besides the main helical frame just described, those stents from the first two families present additional weldings at their ends which provide extra structural stability (purple dots in Figures 3.2 and 3.3). In general, all stents of a given d_{nom} family show the same welding pattern, with the only exception of the nominal size 9 mm × 3.50 mm (see planar representation set aside in Figure 3.3). This particular stent presents a tri-helical motif instead of the bi-helical commonly exhibited by mid caliber stents.

Having described the two types of modular elements and the three welding patterns of our two stent models, we can finally establish the only three well differentiated architectures they exhibit. Let us call them architectures α, β and γ. On the one hand, stents from architecture α are built with seven-pointed long-crowns in mono-helical assemble (d_{nom} = 2.25, 2.50 and 2.75 mm). On the other hand, stents from architectures β and γ are both made with ten-pointed short-crowns, but one in bi-helical (d_{nom} = 3.00 and 3.50 mm) and the other in tri-helical assemble (d_{nom} = 4.00 and 4.50 mm), respectively. Table 3.2 provides the architecture of each stent versus its nominal size. As mentioned before, these two stent models present one architecture or another just depending on d_{nom}, no matter the

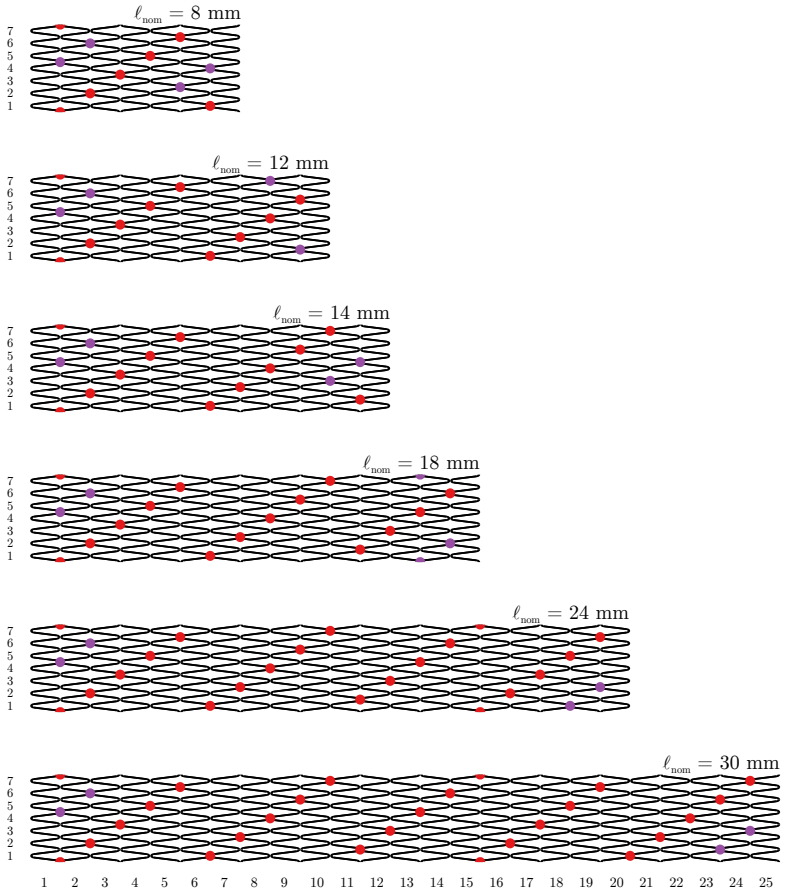

Figure 3.2: Planar representation of the modular structure for MDS and MES stent models with $d_{\text{nom}} = 2.25$, 2.50 and 2.75 mm. Horizontal and vertical numbers count the quantity of crowns for each ℓ_{nom} and the amount of tips of each crown, respectively. Red dots denote the weld points between adjacent crowns establishing the mono-helical motif, and purple dots the four supporting welds, one pair for each stent end.

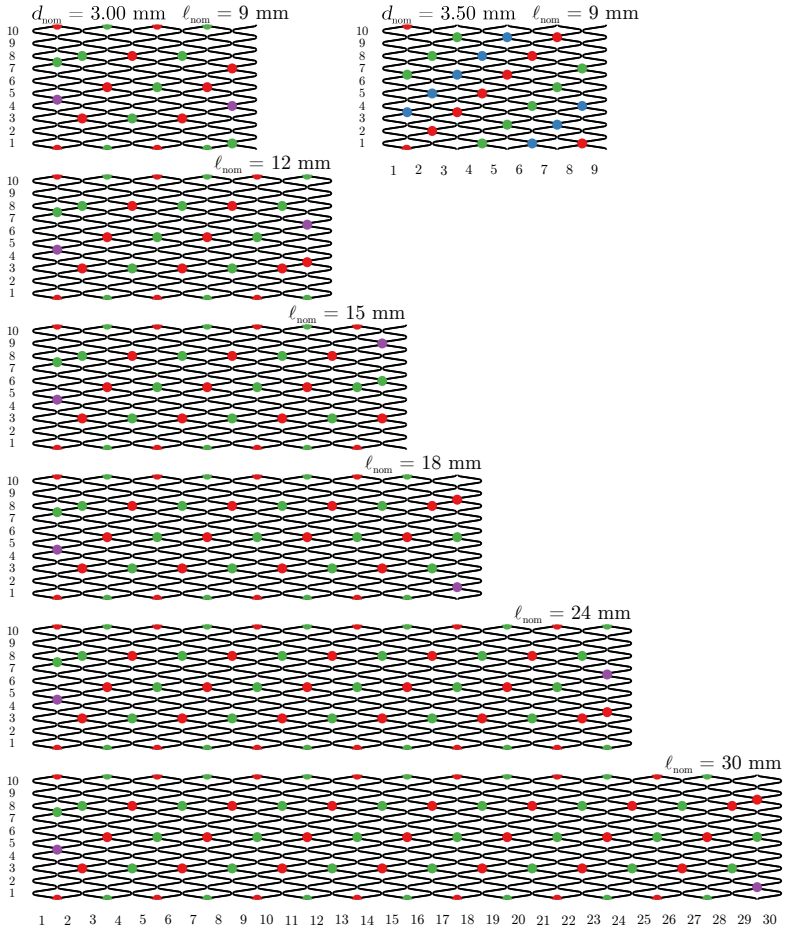

Figure 3.3: Planar representation of the modular structure for MDS and MES stent models with $d_{\text{nom}} = 3.00$ and 3.50 mm. Horizontal and vertical numbers count the quantity of crowns for each ℓ_{nom} and the amount of tips of each crown, respectively. Red and green dots denote the weld points between adjacent crowns establishing the bi-helical welding pattern, and purple dots the two supporting welds, one for each stent end. The sketch set aside depicts the tri-helical motif of the nominal size 9 mm × 3.50 mm, the only exception found among these two d_{nom} families.

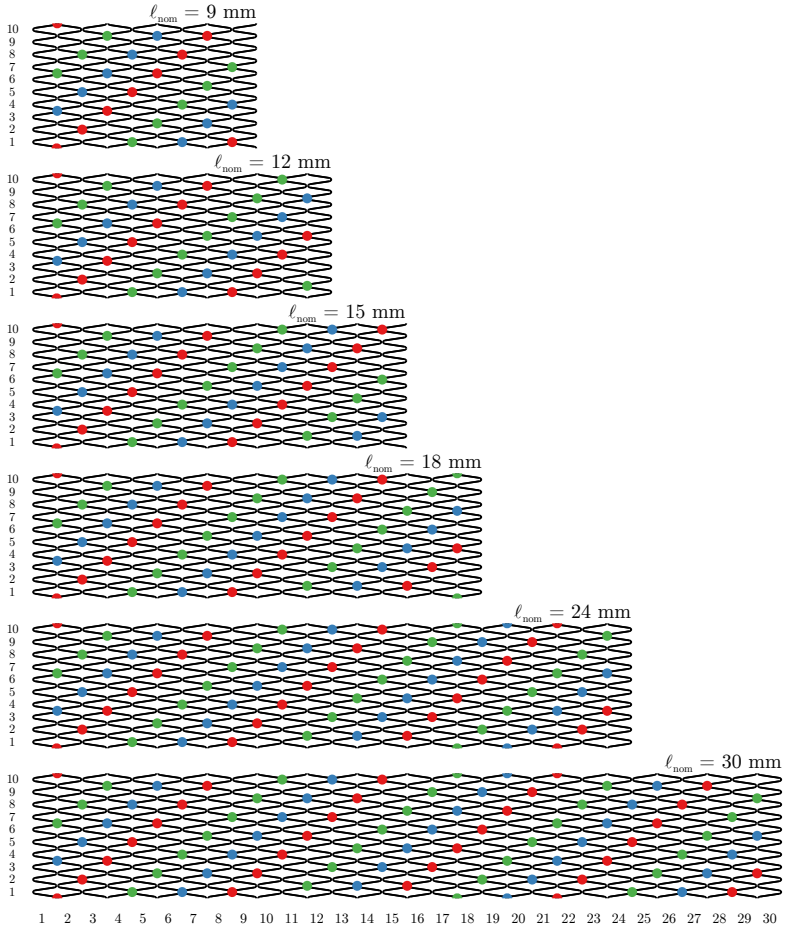

Figure 3.4: Planar representation of the modular structure for MDS and MES stent models with $d_{\text{nom}} = 4.00$ and 4.50 mm. Horizontal and vertical numbers count the quantity of crowns for each ℓ_{nom} and the amount of tips of each crown, respectively. Red, green and blue dots denote the weld points between adjacent crowns establishing the tri-helical motif.

MDS & MES		ℓ_{nom} (mm)							
		8	9	12	14	15	18	24	30
d_{nom} (mm)	2.25	α		α	α		α	α	α
	2.50	α		α	α		α	α	α
	2.75	α		α	α		α	α	α
	3.00		β	β		β	β	β	β
	3.50		γ	β		β	β	β	β
	4.00		γ	γ		γ	γ	γ	γ
	4.50		γ	γ		γ	γ	γ	γ

Table 3.2: Architectures for the MDS and the MES stent models for each nominal size of the assortment. Horizontal and vertical numbers indicate the corresponding nominal length (ℓ_{nom}) and nominal diameter (d_{nom}), respectively. Architecture α consists of seven-pointed crowns in mono-helical construction. Architectures β and γ both consists of ten-pointed crowns, but in bi-helical and in tri-helical construction, respectively. The stent with nominal size 9 mm $\times$ 3.50 mm presents architecture γ instead of β.

precise value of ℓ_{nom}. Only the architecture of the stent with nominal size 9 mm $\times$ 3.50 mm breaks this rule, as it turns out to be γ instead of β.

3.2 Resonance frequency characterization

In the previous section we have described our two stent models from a geometrical viewpoint. We know their full set of commercial available nominal sizes (Table 3.1) as well as the architecture they present depending on ℓ_{nom} and d_{nom} (Table 3.2). We are now interested in finding a link between stents geometrical magnitudes and the angle/frequency data recorded in their corresponding absorbance charts. In this section we will see that characteristic resonance frequencies of stents provide information about their geometry and even their architecture.

To this aim, the thirty-one MDS plus the twenty-nine MES stents presented in Section 3.1 were systematically characterized just after unpacking them from their commercial kits. In order to reach the

nominal size marked in each pack, we expanded the balloon catheter[3] on which each stent is mounted up to its nominal inflation pressure, $p = p_{\text{nom}} = 9.0 \pm 0.5$ atm [3, 4] using a compatible inflation device[4]. Once the expansion had been performed, we determined the actual dimensions of each stent by measuring its real length, ℓ, and its real diameter, d, directly using a digital caliper[5] and a digital micrometer[6], respectively. The final values of ℓ and d were the average of twelve measurements. After that, we acquired the absorbance diagram of each stent with our MWS setup, just as exposed in Chapter 2. For all stents, the frequency-angle characterization window was set from 1.4 GHz to 17.4 GHz and from 0.0° to 360.0°, respectively. We identified the fundamental resonance, f_1, present in each absorbance diagram by inspecting the associated isofrequencial pattern and searching for its characteristic bilobular shape.

Once identified, we selected the isoangular profile at which our resonance presented the highest amplitude, which usually matches the one at normal incidence ($\varphi \simeq 90.0°$), and we fitted it by means of a non-linear least squares fitting algorithm using the resonance-like function shown in Equation 2.4. Finally, we analyzed the dependence of the fundamental resonance frequency of stents on their length, $f_1(\ell)$, and on their diameter, $f_1(d)$, in search of an empirical link between geometrical magnitudes and resonances. In these two representations, we will make no distinction between MDS and MES relying on the fact that for a given nominal size the corresponding architecture is the same independently of the particular stent model. Although this same protocol can be followed for the second resonance, f_2, the results obtained are completely analogous to those obtained with f_1, and thus the study of the fundamental resonance is enough to fully illustrate the link between stent geometry and characteristic resonances along the next subsections.

3.2.1 Resonance frequency versus stent length

Solid and empty color symbols in Figure 3.5 represent respectively experimental $f_1(\ell)$ values for the thirty-one MDS stents plus the

[3]Rapid Exchange Stent Delivery System, Medtronic, Minneapolis, MN, USA.
[4]Encore 26 Advantage Kit, Boston Scientific, Natick, MA, USA.
[5]IP67, Vogel, Kevelaer, Nordrhein-Westfalen, Germany.
[6]IP65, Vogel, Kevelaer, Nordrhein-Westfalen, Germany.

twenty-nine MES stents investigated. Every symbol (solid and empty) denotes a d_{nom} family (see legend for details). Notice how f_1 follows a decreasing dependence on ℓ that, at first glance, seems to obey a reciprocal $1/\ell$ relationship. To clear this up, Figure 3.5b provides again the same information as Figure 3.5a, but this time with the abscissa axis represented in reciprocal scale. Now the experimental $f_1(\ell)$ data points realign, and thus provide a better insight of the $1/\ell$ behavior previously surmised. Color lines in Figure 3.5 represent the least squares fits obtained using a reciprocal function plus an additive constant for each d_{nom} series:

$$f_n(\ell) = \frac{A_n}{\ell} + B_n. \tag{3.1}$$

Here, A_n and B_n are the fitting parameters for the nth-order resonance f_n. Table 3.3 summarize A_1 and B_1 estimates in the particular case of the fundamental resonance, f_1. The relative uncertainties obtained are moderate for A_1 $(1\% - 4\%)$ but substantially greater for B_1 $(9\% - 19\%)$. In any case, from the adjusted coefficient of determination, r^2, provided in the last column of Table 3.3, we verify that the goodness of the seven fits performed is acceptable. Values found for B_1 turn out to be rather scattered whilst those found for A_1 tend to establish three separated groups. We have $A_1^{\alpha} \simeq 51$ GHz mm for thinner stents ($d_{\text{nom}} = 2.25$, 2.50 and 2.75 mm), $A_1^{\beta} \simeq 62$ GHz mm for mid caliber stents ($d_{\text{nom}} = 3.00$ and 3.50 mm) and $A_1^{\gamma} \simeq 77$ GHz mm for thicker stents ($d_{\text{nom}} = 4.00$ and 4.50 mm). Notice how these three groups coincide with those establishing the α, β and γ stent architectures. This fact can also be straightaway seen in Figures 3.5a and 3.5b, since fitting color lines tend to clump following this same distribution. In Section 3.3 we will give the proper interpretation of both fitting parameters beyond their pure empirical sense.

3.2.2 Resonance frequency versus stent diameter

Solid and empty color symbols in Figure 3.6 represent respectively the $f_1(d)$ experimental values for the thirty-one MDS stents plus the twenty-nine MES stents investigated. Every symbol (solid and empty) denotes a ℓ_{nom} family (see legend for details). Unlike what happened with ℓ, the relationship between fundamental resonance frequencies and d is not so obvious. Notice how the f_1 estimates seem to follow

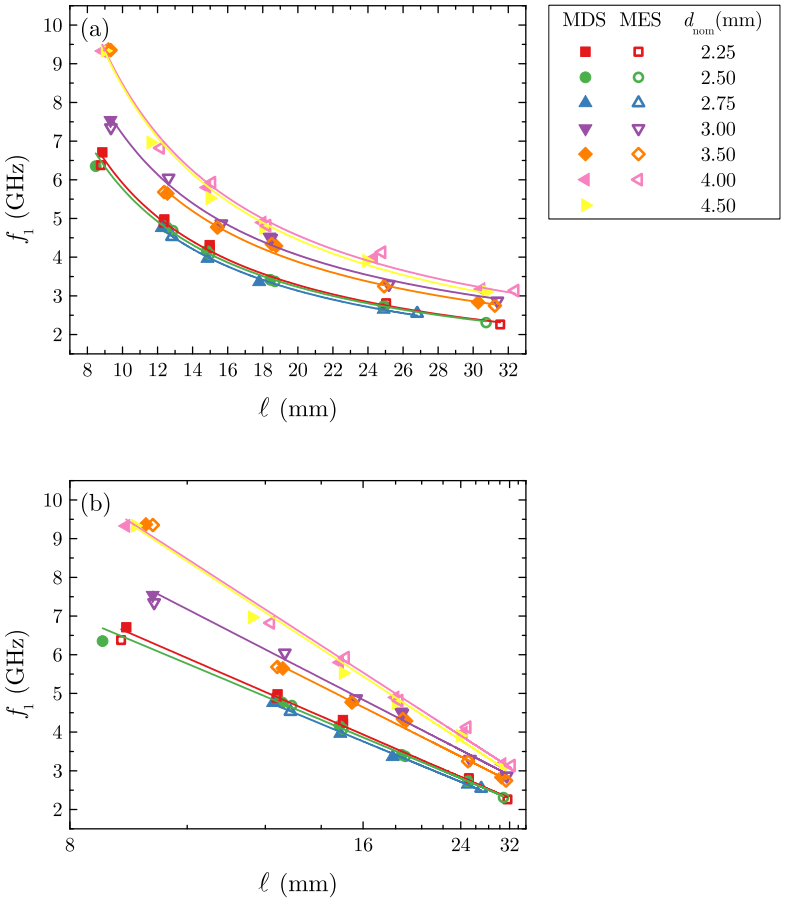

Figure 3.5: Fundamental resonance frequency for the MDS and MES stent models (solid and empty symbols, respectively) as a function of their corresponding real length, $f_1(\ell)$, for several nominal diameters, d_{nom} in normal scale (a) and reciprocal scale (b). Solid color lines are the least squares fits performed on each $f_1(\ell)$ data set using Equation 3.1. The f_1 estimates belonging to nominal size 9 mm $\times$ 3.50 mm for both stent models (solid and empty orange diamonds around 9 mm) have been dropped from the corresponding fit (orange solid line).

MDS & MES		A_1 (GHz mm)	B_1 (GHz)	r^2
d_{nom} (mm)	2.25	52.7 ± 1.4	0.64 ± 0.12	0.995
	2.50	50.8 ± 0.9	0.69 ± 0.06	0.997
	2.75	50.3 ± 1.2	0.62 ± 0.08	0.997
	3.00	62 ± 2	0.94 ± 0.14	0.990
	3.50	61.2 ± 1.7	0.82 ± 0.09	0.994
	4.00	78.3 ± 1.3	0.65 ± 0.10	0.997
	4.50	79.2 ± 1.3	0.49 ± 0.09	0.9990

Table 3.3: Results of the non-linear least squares fit obtained from the fitting function of Equation 3.1 for each $f_1(\ell)$ data set presented in Figure 3.5. From left to right, columns indicate stent nominal diameter (d_{nom}), regression parameters (A_1, B_1) and adjusted coefficient of determination (r^2).

a stepwise dependence on d with three separated rungs. Solid and dotted color lines in Figure 3.6 highlight this singular double-fault shape. However, f_1 values remain quite constant at each rung (solid color lines), until an abrupt rift takes place (dotted color lines). This makes difficult to perform a least squares fit robust enough to obtain an analytical expression from the empirical $f_1(d)$ dependence. Notice how the resonance frequencies of thinner stents ($d_{\mathrm{nom}} = 2.25$, 2.50 and 2.75 mm) are located at the first rung, those corresponding to mid caliber stents ($d_{\mathrm{nom}} = 3.00$ and 3.50 mm) are at the second one and those of thicker stents ($d_{\mathrm{nom}} = 4.00$ and 4.50 mm) are at the third one. Once again, the three groups just listed here match those establishing α, β and γ stent architectures.

3.2.3 Resonance frequency versus stent architecture

The experimental $f_1(\ell)$ and $f_1(d)$ dependences revealed suggest some kind of relation between the precise value of f_1 for a given stent and its actual architecture. From Figure 3.6 we have seen that for each ℓ_{nom} family, f_1 values form three groups according to α, β and γ stent architectures. This sorting is also followed by the fitting color lines in Figure 3.5, which tend to bunch into separated groups following the same distribution. To elucidate this conjecture, let us isolate the fitting parameter A_1 from Equation 3.1 in order to compute it

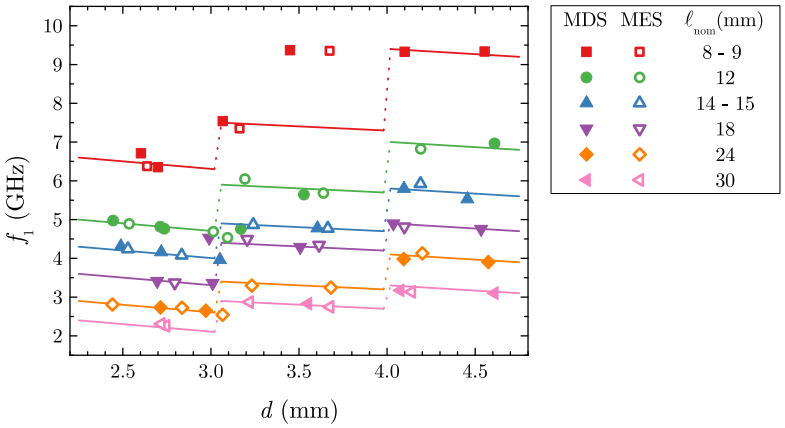

Figure 3.6: Fundamental resonance frequency for the MDS and MES stent models (solid and empty color symbols, respectively) as a function of their corresponding real diameter, $f_1(d)$, for several nominal lengths, ℓ_{nom}. Solid and dotted color lines are guides to the eye to highlight the stepped dependence followed by each ℓ_{nom} family.

directly from f_1, ℓ and B_1 estimates:

$$A_1 = (f_1 - B_1)\ell. \tag{3.2}$$

Note that for each d_{nom} family we should take the proper B_1 value from Table 3.3. Solid and empty color symbols in Figure 3.7 represent respectively the resulting $A_1(d)$ dependences for the thirty-one MDS stents plus the twenty-nine MES stents investigated. Every symbol (solid and empty) denotes a d_{nom} family (see legend for details). In addition we used red, green and blue colors to label stent architectures α, β and γ, respectively. The general shape of the $A_1(d)$ relationship obtained resembles that of $f_1(d)$ from Figure 3.6, but now data points rescale and trace a single double-fault profile with a separated rung univocally associated to each stent architecture. It is particularly striking how the two points corresponding to nominal size 9 mm $\times$ 3.50 mm (solid and empty blue diamonds) move away from the second rung and reach the level of the third rung. This is because the said nominal size is the only among $d_{\text{nom}} = 3.00$ and 3.50 mm families with architecture γ instead of β (see Table 3.2), and thus, the associated A_1 estimate fits better into those corresponding to

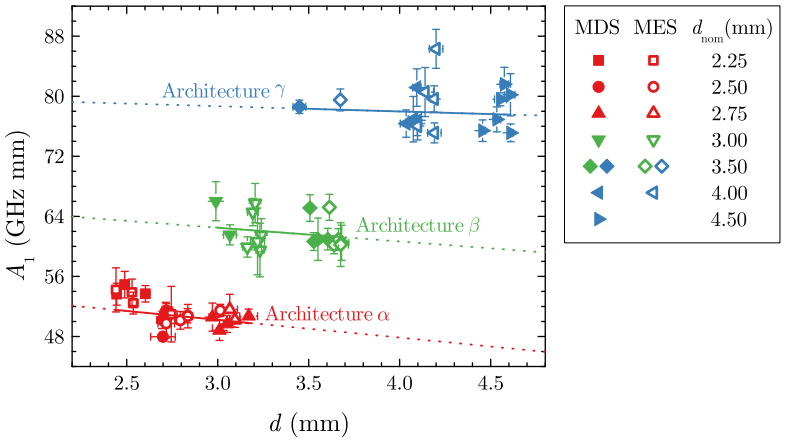

Figure 3.7: Fitting parameter from Equation 3.2 for the MDS and MES stent models (solid and empty color symbols, respectively) as a function of their corresponding real diameter, $A_1(d)$, for several nominal diameters, d_{nom}. Solid and dotted color lines are guides to the eye to highlight α, β and γ stent architectures corresponding to each nominal size (red, green and blue, respectively).

the $d_{\text{nom}} = 4.00$ and 4.50 mm families. Similarly as occurred with $f_1(d)$ in Figure 3.6, $A_1(d)$ remains mostly constant at each rung (see solid and dotted color lines). Therefore, Figure 3.7 tells us that the fitting parameter A_1 from Equation 3.1 depends strongly on the stent architecture rather than on the precise d value.

3.3 The dipole antenna model

So far, we have merely addressed the link between stents geometry and their characteristic resonances through an empirical approach. We need a theoretical framework to give a physical interpretation to the fitting parameters from Equation 3.1 and therefore reach a better understanding of the scattering process occurring between incident microwave electromagnetic fields and metallic stents. In Chapter 2 we have seen that stents exhibit discrete resonances, each one featuring a very characteristic multi-lobed angular pattern. In the present chapter we have shown that the fundamental resonance frequency of a stent follows a nice reciprocal dependence with its corresponding length.

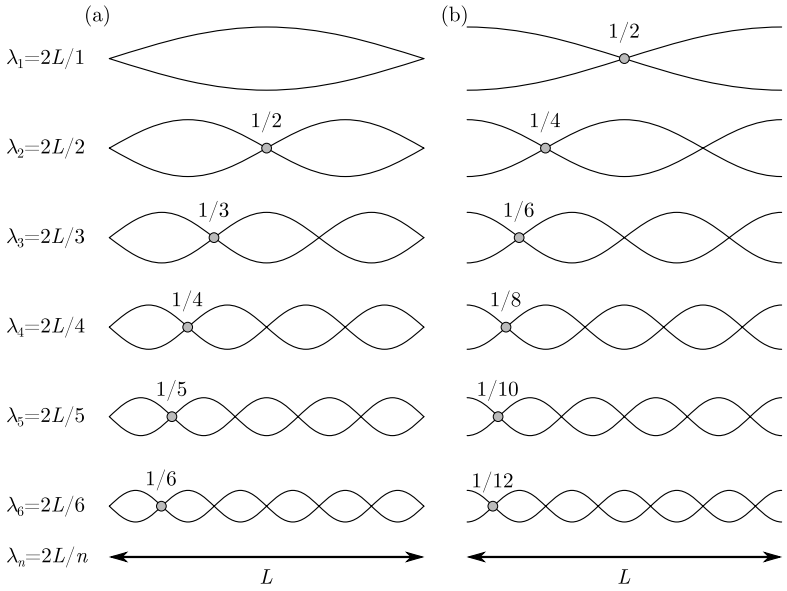

Figure 3.8: Qualitative representation of the first six vibrational modes of an ideal unidimensional resonator with characteristic length L. The wavelengths of successive nth-order overtones, λ_n, match integer divisions of twice the resonator length, $\lambda_n = 2L/n$. In the particular case of an electromagnetic resonator (like a center-fed half-wave dipole antenna) open circuit boundary conditions establish current nodes (a) and voltage anti-nodes (b) at its two ends.

These two facts strongly remind us of the typical behavior of a center-fed half-wave dipole antenna [5]. In particular, the shapes of isofrequencial projections at each resonance frequency found in absorbance diagrams (Figure 2.9) closely resemble gain patterns of such kind of antenna [6]. When these devices work as receivers, any suitable incident electromagnetic wave can couple to the dipole antenna conductive structure inducing a standing electric current along. Due to its open-circuit boundary conditions only resonant current distributions are allowed, which always present current nodes (voltage anti-nodes) at the two ends of the dipole antenna. Each possible current distribution has an associated resonance frequency which can be determined by relating the length of the dipole antenna,

L, with all possible resonating wavelengths, λ_n, as follows:

$$L = n\frac{\lambda_n}{2}, \tag{3.3}$$

where n is the resonance order and its value can take any natural number greater than zero. Alternatively, n may also be viewed as the total number of current anti-nodes (or the total number of current nodes plus one) exhibited by the standing current (see Figure 3.8). Rewriting λ_n as a function of the standing wave velocity, v, and all possible resonating frequencies, F_n, we reach

$$L = \frac{nv}{2F_n}. \tag{3.4}$$

Assuming now that the dipole antenna is embedded inside a medium with a certain electric permittivity, ε, and magnetic permeability, μ, we arrive to the following expression:

$$L = \frac{n}{2F_n\sqrt{\varepsilon\mu}} = \frac{nc}{2F_n\sqrt{\varepsilon_r\mu_r}}, \tag{3.5}$$

where ε_r and μ_r are respectively the relative permittivity and relative permeability of the dipole antenna surrounding medium and c is the speed of light in vacuum. We can finally obtain a general equation for all possible resonating frequencies of a center-fed half-wave dipole antenna surrounded by a certain material:

$$F_n(L) = \frac{nc}{2L\sqrt{\varepsilon_r\mu_r}}. \tag{3.6}$$

As mentioned before, F_n obeys a reciprocal relationship on L, just like f_1 on ℓ in Figure 3.5. Considering that the electromagnetic properties of air are similar to those of vacuum ($\varepsilon_r = \varepsilon_r^{\text{air}} \simeq 1$, $\mu_r = \mu_r^{\text{air}} \simeq 1$), we can use Equation 3.6 to compare resonance frequencies of a dipole antenna with those of metallic stents. The black dotted line in Figure 3.9 represents the theoretical $F_1(L)$ dependence along with the experimental $f_1(\ell)$ data points. Notice how resonance frequencies of dipole antennas are significantly higher than those corresponding to metallic stents or, in other words, for a same resonance frequency dipole antennas exhibit longer lengths than metallic stents. This suggests that in terms of microwave scattering, metallic stents of a given length ℓ behave akin to dipole antennas with a stretched length

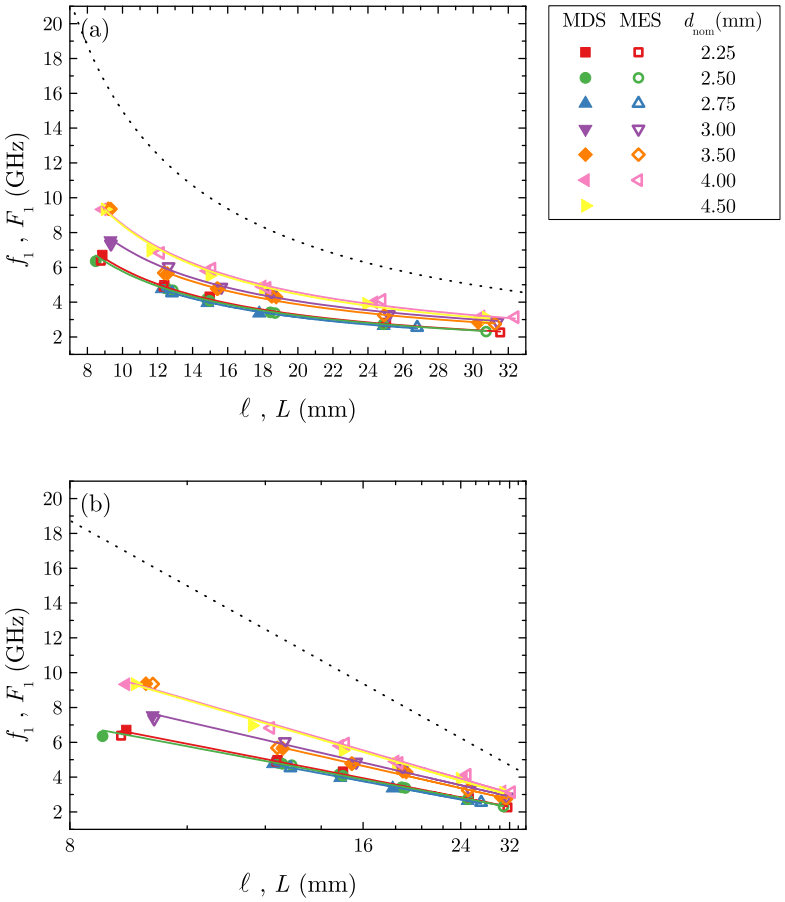

Figure 3.9: Comparison between experimental fundamental resonance frequencies versus the stent length, $f_1(\ell)$ (solid and empty color symbols), with theoretical fundamental resonance frequency versus the center-fed half-wave dipole antenna length, $F_1(L)$ (black dotted line), in normal scale (a) and reciprocal scale (b). Solid color lines are the least squares fits performed on each $f_1(\ell)$ data set using Equation 3.1.

$L = a\ell$, where a is just a dimensionless scaling factor greater than one. Taking this into account Equation 3.6 leads to

$$F_n(\ell) = \frac{nc}{2a\ell\sqrt{\varepsilon_r \mu_r}}. \tag{3.7}$$

MDS & MES		a	f_1^{off} (GHz)
d_{nom} (mm)	2.25	2.84 ± 0.08	0.64 ± 0.12
	2.50	2.95 ± 0.05	0.69 ± 0.06
	2.75	2.98 ± 0.07	0.62 ± 0.08
	3.00	2.40 ± 0.09	0.94 ± 0.14
	3.50	2.45 ± 0.07	0.82 ± 0.09
	4.00	1.91 ± 0.03	0.65 ± 0.10
	4.50	1.89 ± 0.03	0.49 ± 0.09

Table 3.4: Values of the scaling factor, a, and the frequency offset, f_1^{off}, calculated by means of Equations 3.8 and 3.9 using the estimates for the fitting parameters A_1 and B_1, summarized in Table 3.3 for each d_{nom} family.

At this point, by juxtaposing and comparing Equations 3.1 and 3.7, the fitting parameter A_n can be expressed as

$$A_n = \frac{nc}{2a\sqrt{\varepsilon_r \mu_r}}. \tag{3.8}$$

Notice how, besides depending on the nature of the surrounding medium through ε_r and μ_r, A_n also depends on the precise value of the scaling factor a. Keeping in mind this equation and looking back at Figure 3.7, we understand that the dependence with the stent architecture we previously assigned to A_1 is ultimately attributed to a.

Since $L = a\ell$, we envisage that this scaling factor should be proportional to how circuitous the architecture of a given stent is. Recovering the A_1 values summarized in Table 3.3 and considering again $\varepsilon_r = \varepsilon_r^{\text{air}} \simeq 1$, $\mu_r = \mu_r^{\text{air}} \simeq 1$, we can compute a for each d_{nom} family. Table 3.4 provides the corresponding estimates, which turn out to be greater than one for every d_{nom} family, just as previously surmised. As average values for each stent architecture we have $a_\alpha \simeq 2.9$, $a_\beta \simeq 2.4$ and $a_\gamma \simeq 1.9$, respectively. According to that ($a_\alpha > a_\beta > a_\gamma$), architecture α should be more circuitous than β, which in turn should be more circuitous than γ. This explanation results reasonable remembering the number of welding points between adjacent crowns of each architecture: the more connecting welds a certain architecture has, the more straight the path of the

standing electric current induced along the stent should be, and as a consequence, the smaller the associated scaling factor would be. Therefore, stents with mono-helical architecture α (one weld) would have higher a values than stents with bi-helical architecture β (two welds), which in turn would have higher a values than stents with tri-helical architecture γ (three welds), just as we have found.

Modeling a stent of length ℓ as a stretched dipole antenna of length $a\ell$ has proven useful to read the physical meaning of A_n. However, interpreting B_n beyond its pure empirical sense is harder because Equation 3.7 does not consider any additive term. Looking at Equation 3.1, we see that the contribution of B_n to f_n becomes dominant for large ℓ values and thus, B_n would act as some kind of frequency offset, f_n^{off}, which adds to the nth-order resonance frequency and should be determined for each mode separately. In any case, we are only able to just redefine B_n as

$$B_n \equiv f_n^{\text{off}}. \tag{3.9}$$

Table 3.4 provides the corresponding f_1^{off} values, which range from 0.5 GHz to 0.9 GHz without any clear dependence on d_{nom}. At this stage, using the A_n and B_n expressions provided in Equations 3.8 and 3.9, we can finally rewrite Equation 3.1 as follows:

$$f_n(\ell) = \frac{nc}{2a\ell\sqrt{\varepsilon_r\mu_r}} + f_n^{\text{off}}. \tag{3.10}$$

In sum, our half-theoretical half-empirical model inspired by a dipole antenna tells us that the characteristic resonance frequency of a stent depends on ℓ in a reciprocal manner. In addition, the particular stent architecture also plays a role in such resonance frequency through the empirical scaling factor a. Last but not least, the electromagnetic nature of the material surrounding the stent would affect its resonance frequency through ε_r and μ_r. In this regard, since we carried out the experiments in free space conditions, it is worth to consider (at least qualitatively) how the biological tissue around an implanted stent would affect its resonance frequency. According to Equation 3.10, the *in vivo* resonance frequency of an implanted stent, f_n^{in}, should obey the relationship

$$f_n^{\text{in}} \propto \frac{nc}{2a\ell\sqrt{\varepsilon_r^{\text{in}}\mu_r^{\text{in}}}} \simeq \frac{nc}{2a\ell\sqrt{\varepsilon_r^{\text{in}}}}, \tag{3.11}$$

where $\varepsilon_r^{\text{in}}$ and μ_r^{in} are respectively the *in vivo* relative permittivity and the *in vivo* relative permeability evaluated at the *in vivo* resonance frequency itself. In this expression we have approximated $\mu_r^{\text{in}} \lesssim 1$ just remembering the slightly diamagnetic nature of the human body [7]. We can proceed analogously to write the same relationship for free space conditions:

$$f_n \propto \frac{nc}{2a\ell\sqrt{\varepsilon_r^{\text{air}}\mu_r^{\text{air}}}} \simeq \frac{nc}{2a\ell}, \tag{3.12}$$

where, as usual, we have considered that the electromagnetic properties of air are similar to those of vacuum, $\varepsilon_r^{\text{air}} \simeq 1$ and $\mu_r^{\text{air}} \simeq 1$. Now we can combine expressions 3.11 and 3.12 in order to find the link between any free space resonance frequency and its *in vivo* counterpart:

$$f_n^{\text{in}}(f_n) \propto \frac{f_n}{\sqrt{\varepsilon_r^{\text{in}}(f_n^{\text{in}})}}. \tag{3.13}$$

Here we have explicitly indicated that the *in vivo* relative permittivity must be evaluated at the *in vivo* resonance frequency, $\varepsilon_r^{\text{in}}(f_n^{\text{in}})$. At this point, we foresee that f_n^{in} would be downshifted with respect to f_n by an amount proportional to $\varepsilon_r^{\text{in}}$ simply because typical permittivities of biological tissues are considerably greater than one in such frequency range [7]. From this expression we also realize that, in order to estimate f_n^{in}, we first need the value of $\varepsilon_r^{\text{in}}$ at that precise *in vivo* resonance frequency f_n^{in}, which is exactly what we intend to determine. We numerically solved this catch 22 situation with the very simple iterative method outlined in Figure 3.10.

This algorithm starts by searching the permittivity of a certain biological tissue [8–11] at a given free space resonance frequency, $\varepsilon_r(f_n)$ (first $\downarrow$). Once found, we use Equation 3.13 to find f_n', the initial approximation to f_n^{in} (first $\nearrow$). At this point we use f_n' to correct the starting permittivity election and thus find $\varepsilon_r'(f_n')$, the initial approximation to $\varepsilon_r^{\text{in}}$ (second $\downarrow$). This process can be repeated again until the algorithm converges towards f_n^{in} and $\varepsilon_r^{\text{in}}$, which usually happens in less than ten iterations.

As an example, in Figure 3.11a we represent the *in vivo* downshift dependence, $f_n^{\text{in}}(f_n)$, for some representative tissues typically found around an implanted stent (see legend for details). In this same plot, and just as a reference, we also provide such relationship for water. Notice how blood, blood vessel and myocardium tissues (red, green

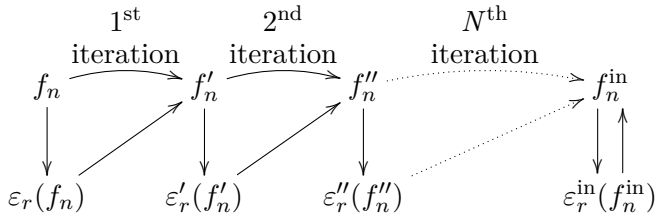

Figure 3.10: Algorithm used to compute the *in vivo* resonance frequency, f_n^{in}, starting from a certain free space resonance frequency, f_n, and the relative dielectric permittivity of a given biological tissue, ε_r.

and blue solid lines, respectively) produce larger *in vivo* downshifts when compared with adipose tissue (orange solid line). In the first case the original free space frequency window moves from $2-10$ GHz to $0.2-1.6$ GHz, whilst in the second case only reaches $0.8-4.2$ GHz. This is because the permittivity of a biological tissue strongly depends on the average polarity of the molecules that compose it. In general, tissues with highly polar molecular content (such water) have higher permittivities, while those with highly apolar molecular content (such lipids) have lower permittivities and thus would induce minor *in vivo* downshifts. Finally, in order to better illustrate this reasoning, Figure 3.11b provides the $\varepsilon_r(f)$ data used to compute the $f_n^{\text{in}}(f_n)$ relationships shown in Figure 3.11a.

3.4 Conclusions

In this chapter we have followed an empirical approach to study the dependence of f_1 on the two major geometrical stent parameters, ℓ and d. To this aim we have characterized thirty-one MDS plus twenty-nine MES stents with varied nominal sizes. On the one hand, we have shown that f_1 follows a reciprocal dependence on ℓ for each d_{nom} family. Through a least squares fit of experimental data we have managed to get an empirical expression for $f_1(\ell)$ introducing the fitting parameters A_1 and B_1. On the other hand, the $f_1(d)$ dependence was not so straightforward and we could not get any empirical expression. However, the study of $A_1(d)$ has revealed that

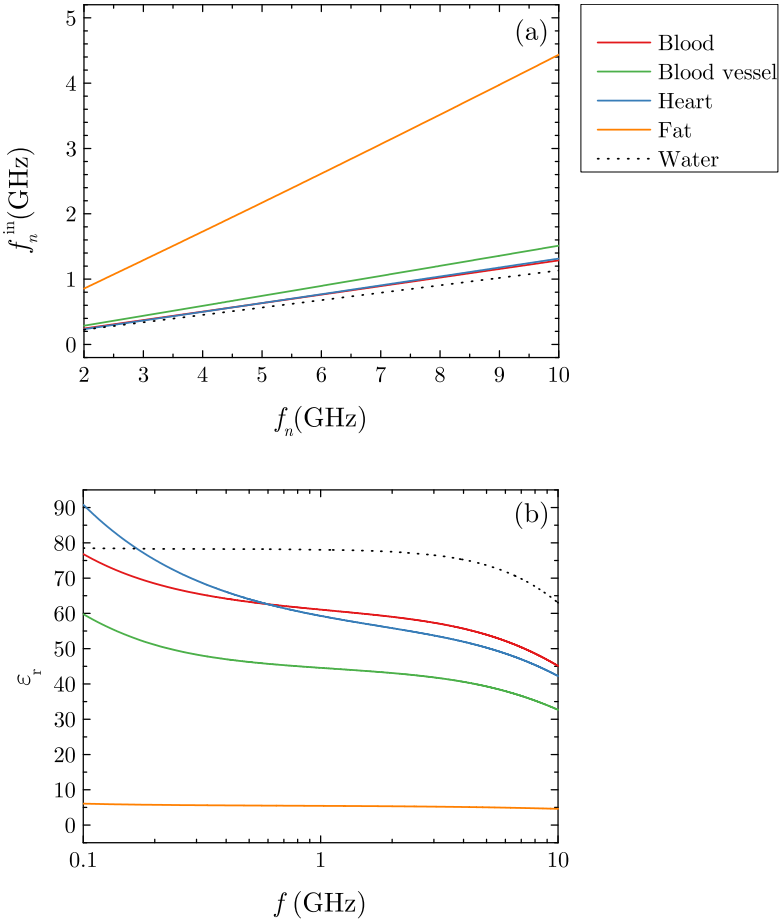

Figure 3.11: (a) *In vivo* resonance frequency versus the free space resonance frequency, $f_n^{\text{in}}(f_n)$, for some representative tissues typically found around an implanted stent (solid color lines) and water (dashed black line). (b) Relative dielectric permittivity versus the microwave frequency, $\varepsilon_r(f)$, for the same tissues (data taken from Ref. [8]) and water (experimentally obtained with a commercial probe-based instrument[7]). The frequency has been expressed in logarithmic scale.

[7] 85070C Dielectric Probe Kit, Agilent Technologies, Santa Clara, CA, USA.

the stent architecture also defines the precise resonance frequency of a given stent.

These results have laid the foundations to establish a half-theoretical half-empirical model able to explain the characteristic resonance frequencies of stents from a fundamental viewpoint. To do that we have recovered the general equation for the resonance frequencies of a center-fed half-wave dipole antenna of length L, and have juxtapose our $f_1(\ell)$ empirical expression. This has shown that, in terms of microwave scattering, stents of length ℓ behave just like dipole antennas with a stretched length $L = a\ell$, being a a dimensionless scaling factor greater than one. We have also provided an interpretation for this scaling factor, suggesting that it should be proportional to how intricate the architecture of a given stent is. Finally, we have taken advantage of our model to estimate the resonance frequencies of implanted stents from their corresponding values in free space conditions $f_n^{\text{in}}(f_n)$. We have seen that, for usual surrounding tissues such as blood, blood vessel or myocardium, *in vivo* resonance frequencies are around one order of magnitude smaller than their free space counterparts.

References

[1] *Standard specification for wrought 35 cobalt - 35 nickel - 20 chromium - 10 molybdenum alloy for surgical implant applications (UNS R30035)*, ASTM International, (2016) `http://www.astm.org/Standards/F562.htm` (cit. on p. 47).

[2] *Driver flipchart, Medtronic coronary stent system, design for life*, Obtained from the official medtronic website. Currently not available (2007) (cit. on p. 47).

[3] *Driver sprint rapid exchange coronary stent system, Instructions for use*, Revision B (2011) (cit. on p. 53).

[4] *Endeavor sprint rapid exchange zotarolimus-eluting coronary stent system, Instructions for use*, Revision A (2011) (cit. on p. 53).

[5] C. A. Balanis, *Antenna theory: Analysis and design* (Wiley, New York, 1997) (cit. on p. 59).

[6] S. J. Orfanidis, *Electromagnetic waves and antennas* (Rutgers University, New Jersey, 2002) (cit. on p. 59).

[7] A. V. Vorst, A. Rosen, and Y. Kotsuka, *RF/ microwave interaction with biological tissues* (Wiley, New York, 2006) (cit. on p. 64).

[8] *An internet resource for the calculation of the dielectric properties of body tissues in the frequency range 10 Hz - 100 GHz*, Italian National Research Council, Institute for Applied Physics Nello Carrara, (2016) `http://niremf.ifac.cnr.it/tissprop/` (cit. on pp. 64, 66).

[9] C. Gabriel, S. Gabriel, and E. Corthout, "The dielectric properties of biological tissues: I. Literature survey," Physics in Medicine and Biology **41**, 2231 (1996) (cit. on p. 64).

[10] S. Gabriel, R. W. Lau, and C. Gabriel, "The dielectric properties of biological tissues: II. Measurements in the frequency range 10 Hz to 20 GHz," Physics in Medicine and Biology **41**, 2251 (1996) (cit. on p. 64).

[11] ——, "The dielectric properties of biological tissues: III. Parametric models for the dielectric spectrum of tissues," Physics in Medicine and Biology **41**, 2271 (1996) (cit. on p. 64).

4

Stent fractures

Physicians have studied the health impact of carrying a fractured stent. Even if not necessarily involving clinical sequelae, medical doctors state that fractured stents may represent a risk factor for sundry stent-related complications. Therefore, the early detection of stent fractures would improve the stenting outcome. In Chapter 3 we have found that the characteristic resonance frequencies of stents depend on their length in a reciprocal manner. Since a stent fracture usually involves a dramatic variation in the stent length, we expect significant changes in the absorbance diagrams generated by fractured stents. In this chapter we assess the prospects of microwave spectrometry in a stent fracture scenario by means of a couple of "fracture tests". The idea of these tests is to submit a stent to a series of controlled cuts and, after each rupture, characterize the damaged stent with the microwave spectrometry setup. By comparing the resulting absorbance diagrams with those generated by intact stents, we will be able to identify therein the characteristic traits of broken stents. Eventually, we will see that from the characteristic frequencies of these features we will be able to find the precise locations on which the stent suffered the rupture.

4.1 Stent fracture

In 2002, Chowdhury and Ramos used cardiac XRA to report the first stent fracture (SF) [1]. The ruptured BMS was originally deployed in a saphenous vein bypass graft to the first obtuse marginal coro-

nary artery. A couple of years later, in 2004, Sianos and coauthors used cardiac XRA and IVUS to report the first two patients with DES ruptures [2]. In both cases the fractured stents were originally deployed at the right coronary artery. Since then, SF has been gradually recognized as a relevant cause of stenting failure, prompting the publication of several reviews [3–10]. In this regard, a successful implementation of MWS for the early diagnosis of SFs would enable to anticipate the onset of the several SF-related complications.

4.1.1 Incidence and medical implications

Extensive studies quantifying the incidence of SF continue to be lacking. Reported values range from 0.84% to 18.6% [11–24]. This battle of percentages is caused by the different conditions of each work. For example, some studies use XRA, some use IVUS and some others combine both techniques to report their SFs cases. This two follow-up modalities may present varying rates of SF detection due to their different accuracies (the corresponding spatial resolutions are 300 μm and 150 μm, respectively). Moreover, the SF definition criteria were not the same in all works. In any case, the true incidence of SF could have been underestimated because detection rates raise up to 29% in postmortem studies [25].

The medical implications of SF are widely varied. Despite patients with SFs may remain asymptomatic, there are many stent-related complications directly associated with the structural failure of the stent. Several studies have demonstrated that SFs significantly increase the risk of ISR, especially in DES [16–21, 26–28]. The mechanisms for smooth muscle cells proliferation around SF sites may be a combination of mechanical irritation and a reduced presence of anti-proliferative drug, both triggered by the disrupted stent geometry [23]. The alteration of the local hemodynamic factors around SF sites may also play a role in the onset of ISR [29]. Additionally, several studies have shown that SF goes hand in hand with stent thrombosis [23, 30, 31]. Figure 4.1 exemplifies this with an XRA picture of a fractured stent originally deployed at the right coronary artery [11]. It has been proposed that the direct contact between metallic broken struts and the luminal surface may cause platelet activation and trigger a subsequent blood clot formation [32]. Other stent-related complications associated with SFs are target lession

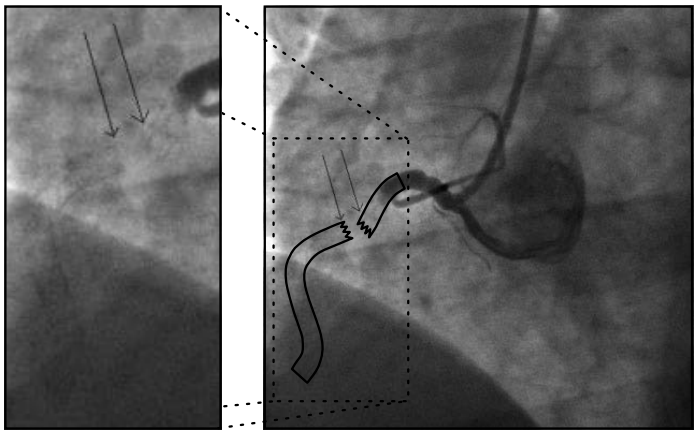

Figure 4.1: XRA showing a stent thrombosis induced by a SF. A Cordis Cypher® sirolimus-eluting stent[1] with nominal size 33 mm × 3.50 mm (black line silhouette) experienced a complete transverse linear rupture in its proximal one-third (black arrows). Eventually, this geometrical disruption triggered a stent thrombosis at the right coronary artery. The additional zoom-in picture highlights the region where the stent is located. Figure adapted from Ref. [11].

recurrence [19, 20, 23, 33] and, to a lesser extent, aneurysm formation [13, 33] and myocardial infarction [23].

4.1.2 Risk factors and mechanism

The risk factors associated with the development of SF are multifactorial and extremely heterogeneous. After having a look at the literature, trying to group them in related categories might be even more puzzling. Nevertheless, the mechanisms responsible for such factors are always mechanical in essence. We have classified the risk factors depending on whether the mechanism behind the SF is lesion-related, stent-related or procedure-related. Once we review SF risk factors and their underlying mechanisms, we will understand that any ingredient able to expose stent struts to a repetitive mechanical load will play an important role in the onset of SF, especially for those stents particularly vulnerable.

[1]Cordis Corporation, Fremont, CA, USA.

The most important lesion-related risk factor is target lesion location at sinuous vessels. In general, stents are more likely to break if deployed at excessively tortuous arteries. As prime examples we have the right coronary artery and the left anterior descending coronary artery [14–16, 21, 22]. Moreover, these two coronary arteries are particularly pulsating, exhibiting exaggerated motion and significant angulations in each heartbeat. Curved vessels promote the onset of hinge points along the stent [21–23, 34]. This fact combined with the millions of repetitive flexions induced by the cardiac cycle end up wearing the stent alloy out until its rupture [18, 19, 21]. The presence of calcification in the target lesion has also been linked with an increased risk of SF. It is believed that this high-density accumulation induces an inhomogeneous distribution of stresses along the vessel wall which may be the nidus for the onset of hinge points [35].

Among the stent-dependent risk factors the particular design of a given stent model stands out. Some stent models are more prone to experience a SF than others depending on their strut thickness, alloy and architecture [36, 37]. The best example of this is the Cordis Cypher® sirolimus-eluting stent[2], which by far is the model with more predisposition to break according to the literature [18, 21]. Each crown pair forming this stent is held together by six S-shaped wire links. In general, stents of architectures with high number of connectors between their modular elements present more structural stability but, nevertheless, they are less flexible and thus less adaptable to the native anatomy of the artery [38]. From this viewpoint, the tradeoff for any stent architecture should be to combine an optimum longitudinal and radial stability with a high degree of conformability after expansion. It has been suggested that the low adaptability of the Cypher stents accounts for their tendency to break [34], especially at their characteristic S-shaped wire links [31]. Another important stent-dependent risk factor is the nominal length of the stent. Longer stents are more prone to fracture, predominantly at their mid portion [13, 19, 21, 22]. This fact results reasonable from a mechanical viewpoint, because for a given bending strain the central region of longer stents experience a more pronounced mechanical deformation than that of shorter stents [18, 21].

[2]Cordis Corporation, Fremont, CA, USA.

Finally, the most important procedure-dependent risk factor is stent overlap. The deployment of a new stent in a previously stented vessel usually involves partial or complete overlap between them. This situation represents an increased risk of SF [33]. As a whole, the resulting overlapped stent is more rigid and its effective conformability is reduced. Moreover, the points where struts from overlapping stents touch act as fulcrums and promote the formation of hinge points [11, 22, 39]. Once a hinge point appears, the repetitive movement associated to the cardiac cycle will do the rest. Another important procedure-dependent risk factor is the application of an excessive pressure during deployment or post dilatation, which has been associated with an increased risk of SF in several studies [11, 17, 21].

4.1.3 Stent fracture classification

The first attempt to systematically classify the different types of SF exhibited by implanted vascular stents dates from 2004 and is attributed to Allie and coauthors [40]. This original standardization, baptized as "*The Cardiovascular Institute of the South nitinol stent fracture classification system*" (let us call it Allies's scale), established four types of fractures:

- Type I: Single strut fracture.
- Type II: Multiple strut fractures.
- Type III: Complete transverse linear stent fracture.
- Type IV: Multiple complete transverse linear stent fractures.

In spite of being published in a non-peer reviewed journal, this classification gradually became the reference standard adopted to grade fractured stents along the following years. Allies's scale remained almost unchanged until 2007, when Jaff and coauthors added a fifth grade [41]: Stent spiral dissection (Type V). In the meantime, Scheinert and coauthors suggested an alternative classification, but it consisted in merely renaming type I, II and III degrees from Allie's scale as "minor", "moderate" and "severe", respectively [42]. Along subsequent years many more classification criteria appeared in the literature [12, 13, 26, 31, 33]. Again, some of these proposals partially reword the degree names of Allie's scale, some incorporated subtleties

like the presence or absence of stent deformation and stent displacement, and some others were devised to be used with specific imaging techniques only. Therefore, we take the classification introduced by Allie and complemented by Jaff as our standard SF grading.

4.2 Fracture test description

We performed two fracture tests, each on a separated stent chosen among those presented in Table 3.1 from Chapter 3. As usual, we used a compatible inflation device[3] to expand the two selected stents up to nominal inflation pressure, $p = p_{\text{nom}} = 9.0 \pm 0.5$ atm, in order to reach their corresponding nominal sizes [43, 44]. We carried out the first fracture test (let us call it FT1) on the MES stent with nominal size 30 mm $\times$ 2.50 mm, and the second one (FT2) on the MDS stent with nominal size 24 mm $\times$ 2.75 mm. Each stent was submitted to a series of cuts using a customized precision pliers and a hand lens. We planned these tests with increasing complexities: one cut for FT1 and a four cut sequence for FT2. In the first test the sole cut straightly led the stent to a type III fracture, whereas in the second test the cutting sequence was devised to make the stent go gradually through type I, II, III and IV fractures. The careful performance of each cut without distorting the stent geometry will be crucial to ensure the validity of both tests.

4.2.1 FT1: Type III stent fracture

The planar representation shown in Figure 4.2 illustrates the single cut performed on the MES stent with nominal size 30 mm $\times$ 2.50 mm. One simple cut directly over the weld linking crowns #15 and #16 (see yellow dot in Figure 4.2a) led this stent to a complete transverse linear rupture that split it in two segments, a situation graded as a type III fracture. Before practicing the cut, we labeled the intact stent segment as AB and we measured its actual length, $\ell^{0\text{AB}} = 30.77 \pm 0.04$ mm, using a digital caliper[4]. Then, we acquired its absorbance diagram. Right after the cutting, we labeled the resulting two stent segments as A and B (see Figure 4.2b) and we measured

[3] Encore 26 Advantage Kit, Boston Scientific, Natick, MA, USA.
[4] IP67, Vogel, Kevelaer, Nordrhein-Westfalen, Germany.

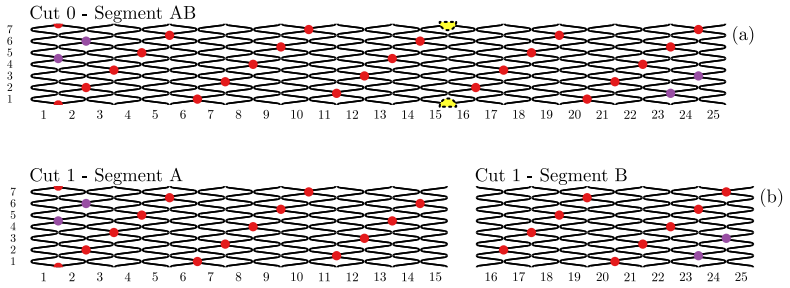

Figure 4.2: Cutting of the MES stent with nominal size 30 mm × 2.50 mm along FT1. (a) Representation of the intact stent segment (named AB). The yellow dot between crowns #15 and #16 denotes the weld where the cut was applied. (b) Representation of the resulting fractured stent segments (named A and B, respectively).

their actual lengths, $\ell^{1A} = 18.58 \pm 0.05$ mm and $\ell^{1B} = 12.16 \pm 0.03$ mm. Finally, we recorded the absorbance diagram of the fractured stent placing both segments together on the sample holder with 1, 2, 5, and 10 mm gaps in between. We also acquired the absorbance diagram of each segment separately.

At this point, we already had all the information needed to analyze this fracture test. Figure 4.3 summarizes FT1 by comparing two absorbance diagrams, the first taken before the cut, and the second after. The longitudinal micro-pictures in Figures 4.3a and 4.3b show the stent before and after the cutting. The additional zoom-in micro-picture from Figure 4.3c highlights the cut zone. Notice how the weld was neatly split in half without distorting the adjacent crowns. Figures 4.3d and 4.3e beside each longitudinal micro-picture present the corresponding absorbance diagrams. The fundamental resonance of the intact stent with its typical bilobular pattern is easily spotted at $f_1^{0AB} = 2.309 \pm 0.005$ GHz. However, when the stent is broken, this initial resonance vanishes and a pair of new split resonances appear at $f_1^{1A} = 3.407 \pm 0.006$ GHz and $f_1^{1B} = 4.778 \pm 0.008$ GHz. We obtained identical results for the entire span of gaps between segments A and B.

4.2.2 FT2: Type I, II, III and IV stent fractures

The planar representation shown in Figure 4.4 illustrates the cutting sequence performed on the MDS stent with nominal size 24 mm ×

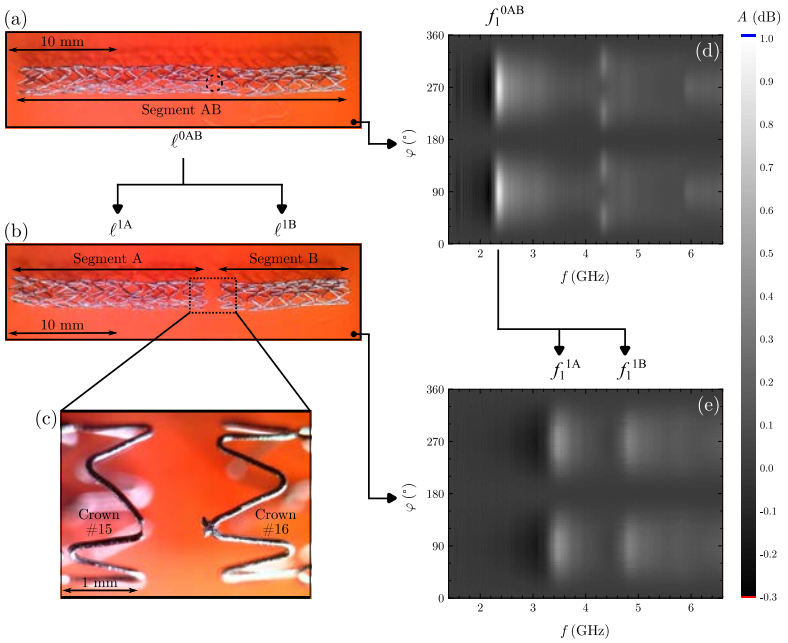

Figure 4.3: Summary of FT1. (a) and (b) Longitudinal micro-pictures of the stent before and after the fracture. (c) Zoom-in micro-picture highlighting the weld were the cut was applied. (d) and (e) Absorbance diagrams of the intact stent and the two emerging stent pieces (gap of 1 mm).

2.75 mm. We devised this succession of four cuts to make the stent go gradually through I, II, III and IV fracture types. Similarly to what it had been done along the previous fracture test, we recorded the lengths of the emerging stent segments and their corresponding absorbance diagrams at each stage. After those cuts generating multiple stent segments, we acquired the absorbance diagram of the fractured stent placing all pieces together on the sample holder and fixing all gaps at 1, 2, 5, and 10 mm. Again, we also recorded the absorbance diagram of each segment separately.

Before practicing the first cut we labeled the intact stent segment as ABC (see Figure 4.4a). Its length was $\ell^{0ABC} = 24.91 \pm 0.03$ mm. Cut 1 was carried out on the strut close to the weld between crowns #9 and #10 (see left yellow dot in Figure 4.4a). As a result the stent presented a single broken strut, a state graded as a type I

fracture (see Figure 4.4b). At this stage, the length of segment ABC, $\ell^{1\mathrm{ABC}} = 24.72 \pm 0.04$ mm, was slightly shorter than $\ell^{0\mathrm{ABC}}$. Cut 2 was executed on the strut near the weld holding together crowns #15 and #16 (see right yellow dot in Figure 4.4a). Hence, the stent presented multiple broken struts, a situation graded as a type II fracture (see Figure 4.4c). Now the length of segment ABC, $\ell^{2\mathrm{ABC}} = 24.66 \pm 0.04$ mm, remained nearly invariant with respect to $\ell^{1\mathrm{ABC}}$ but was still significantly shorter than $\ell^{0\mathrm{ABC}}$. Cut 3 was performed again on crown #9, in the strut just beneath the one where cut 1 had been done. This resulted in a complete transverse linear rupture that divided the stent into two segments, which is graded as a type III fracture. We labeled the resulting two stent segments as A and BC (see Figure 4.4d). Their lengths were $\ell^{3\mathrm{A}} = 11.17 \pm 0.03$ mm and $\ell^{3\mathrm{BC}} = 14.40 \pm 0.03$ mm, respectively. In a similar manner, cut 4 was applied on crown #15 in segment BC. Finally the stent presented two complete transverse linear fractures that split it in three segments, a situation graded as a type IV fracture. We labeled the two stent pieces emerging from segment BC as B and C (see Figure 4.4e). Their lengths were $\ell^{4\mathrm{B}} = 7.93 \pm 0.05$ mm and $\ell^{4\mathrm{C}} = 6.64 \pm 0.02$ mm, respectively.

Figure 4.5 summarizes the first half of FT2 (types I and II stages) by comparing three absorbance diagrams, the first one measured before starting the cutting sequence and the next two acquired after cuts 1 and 2, respectively. Figures 4.5a, 4.5b and 4.5c depict the cut sequence applied from the intact stent to a type II fracture. Figures 4.5d, 4.5e and 4.5f beside each planar representation show the corresponding evolution of the absorbance diagrams. The fundamental resonance of the intact stent is clearly identified in Figure 4.5d, $f_1^{0\mathrm{ABC}} = 2.647 \pm 0.004$ GHz. In Figure 4.5e we note that this resonance significantly shifts down once the first cut is made, $f_1^{1\mathrm{ABC}} = 2.332 \pm 0.004$ GHz. Similarly, Figure 4.5f shows that the resonance decreases again after the second cut, $f_1^{2\mathrm{ABC}} = 2.203 \pm 0.003$ GHz.

Figure 4.6 summarizes the second half of FT2 (types III and IV stages) by comparing three absorbance diagrams, the first one measured before starting the cutting sequence and the next two acquired after cuts 3 and 4, respectively. Figures 4.6a, 4.6b and 4.6c represent the cut sequence applied from the intact stent to a type IV fracture (skipping type I and II stages). Additional micro-pictures in Figures 4.6d and 4.6e detail the final look of the cutting zones.

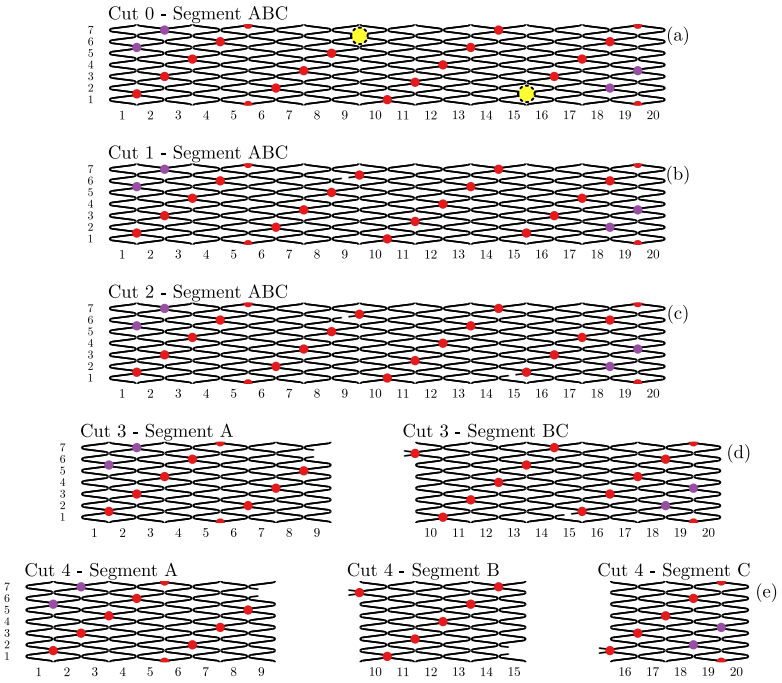

Figure 4.4: Cutting of the MES stent with nominal size 24 mm × 2.75 mm along FT2. (a) Representation of the intact stent (named ABC). The yellow dots between crowns #9/#10, and #15/#16 denote the welds where the successive four cuts were applied. (b) Representation of the fractured stent after cut 1. (c) Representation of the fractured stent after cut 2. (d) Representation of the fractured stent pieces after cut 3 (named A and BC, respectively). (e) Representation of the fractured stent pieces after cut 4 (named A, B and C, respectively).

The left micro-picture shows the region between crowns #9 and #10 where cuts 1 and 3 were made, while the right micro-picture the region between crowns #15 and #16 where cuts 2 and 4 were practiced. Beside each planar representation, Figures 4.6f, 4.6g and 4.6h show the evolution of the corresponding absorbance diagrams from the intact stent to type III and IV fractures. In Figure 4.6g we note that after cut 3, $f_1^{0\mathrm{ABC}}$ splits producing a couple of new resonances at higher frequencies, $f_1^{3\mathrm{A}} = 4.643 \pm 0.008$ GHz and $f_1^{3\mathrm{BC}} = 3.162 \pm 0.004$ GHz, respectively. This fact is completely analogous to what happened in the previous fracture test. One step forward, in Figure 4.6h we now observe how after cut 4, $f_1^{3\mathrm{BC}}$ also splits producing a couple of new resonances at even higher frequencies, $f_1^{4\mathrm{B}} = 5.830 \pm 0.007$ GHz and $f_1^{4\mathrm{C}} = 7.491 \pm 0.007$ GHz. It is also striking how this last cut left $f_1^{3\mathrm{A}}$ invariant, being $f_1^{4\mathrm{A}} = 4.648 \pm 0.007$ GHz. We found analogous results for all gaps between segments A, B and C.

4.3 Fracture test control check

Just by contrasting absorbance diagrams of intact and type I-, II-, III- and IV-fractured stents, we evidence that even the slightest rupture degree leaves a significant footprint in the characteristic resonance frequencies of stents. Higher fracture types III and IV seem to have a different effect on stent resonances than lower fracture types I and II. While lower types shift the fundamental resonance frequency down, higher types apparently split it and shift it up. The individual MWS characterization of the segments emerging from FT1 (after cut 1) and FT2 (after cuts 3 and 4) could help us to understand the origin of the split resonances emerging from higher fracture types. First we will take advantage of these control check measurements to evaluate higher fracture types from a quantitative viewpoint. Indirectly, this analysis also will be useful as a starting point to interpret lower fracture types, at least from a qualitative perspective.

4.3.1 FT1: Control check

Figure 4.7 provides the absorbance diagrams produced by segments A and B when they were measured simultaneously (twinned panel 4.7a) and separately (panels 4.7b and 4.7c). We note that there is no sign of $f_1^{1\mathrm{B}}$ in the absorbance diagram produced by segment A and, vice

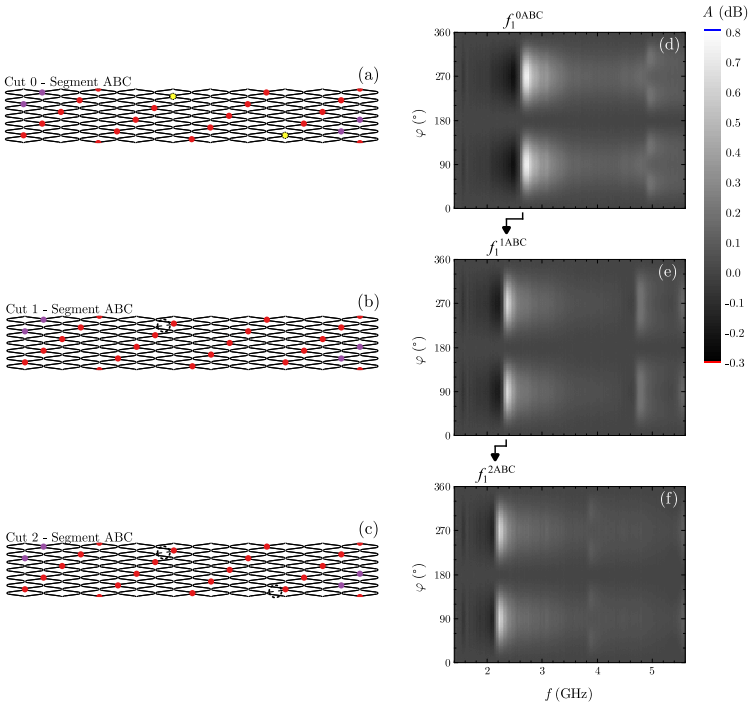

Figure 4.5: Summary of the first two cuts in FT2. (a to c) Cutting sequence performed to gradually bring the intact stent to type I and type II fractures, respectively. (d) Absorbance diagram of the intact stent. (e) and (f) Absorbance diagrams obtained after cuts 1 and 2.

versa, there is no trace of f_1^{1A} in the absorbance diagram produced by segment B. Our simple control check strongly confirms that f_1^{1A} and f_1^{1B} are univocally due to segments A and B, respectively. This suggests that, even when the gap between segments is only 1 mm wide, both stent pieces behave as independent entities when it comes to scatter incident microwaves. As a result, the absorbance diagram produced by the fractured stent is just the addition of the absorbance diagrams generated by the individual elements in which the stent is divided. Moreover, we also check that, within the uncertainty range, the resonance frequencies produced by each segment separately, $f_1^{1A*} = 3.391 \pm 0.007$ GHz and $f_1^{1B*} = 4.746 \pm 0.006$ GHz, are both compatible with their corresponding counterparts produced

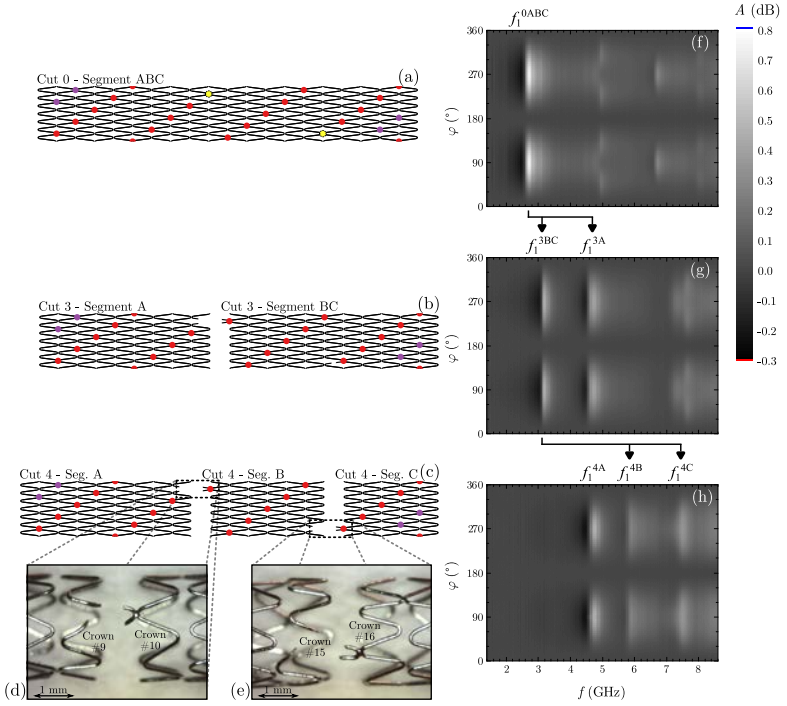

Figure 4.6: Summary of the last two cuts in FT2. (a to c) Cutting sequence performed to gradually bring the intact stent to type III and type IV fractures, respectively. (d) and (e) Zoom-in micro-pictures highlighting the regions where cuts 1/3, and cuts 2/4 were respectively performed. (f) Absorbance diagram of the intact stent. (g) and (h) Absorbance diagrams obtained after cuts 3 (gap of 1 mm) and 4 (both gaps of 1 mm).

by both segments simultaneously, $f_1^{1A} = 3.407 \pm 0.006$ GHz and $f_1^{1B} = 4.778 \pm 0.008$ GHz.

4.3.2 FT2: Control check

Figure 4.8 provides the absorbance diagrams generated by segments A, B and C when they are measured simultaneously (triplicated panel 4.8a) and separately (panels 4.8b, 4.8c and 4.8d). Comparing panels 4.8a and 4.8b, we note that there are no signs of f_1^{4B} and f_1^{4C} in the diagram of segment A. Analogously, neither f_1^{4A} and f_1^{4C} are present in the diagram of segment B nor f_1^{4A} and f_1^{4B} in the diagram of

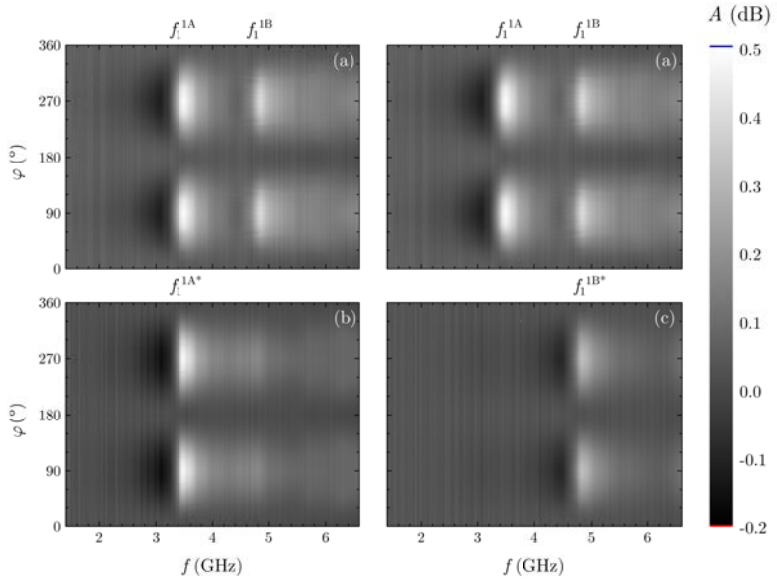

Figure 4.7: Control check measurements for FT1. (a) Absorbance diagram of segments A and B when both are characterized together (gap of 1 mm). (b) and (c) Absorbance diagrams of segments A and B when each is characterized apart, respectively. Each resonance is univocally associated to each one emerging segment: $f_1^{1A} \simeq f_1^{1A*}$ and $f_1^{1B} \simeq f_1^{1B*}$.

segment C. This fact reinforces the idea that the absorbance diagram produced by a segmented stent is the addition of the individual absorbance diagrams generated by each piece in which the stent is divided. Furthermore, we may also check that the resonance frequencies produced by each segment separately, $f_1^{4A*} = 4.631 \pm 0.006$ GHz, $f_1^{4B*} = 5.861 \pm 0.010$ GHz, and $f_1^{4C*} = 7.514 \pm 0.012$ GHz, are all compatible within the uncertainty range with their corresponding counterparts generated by the three segments simultaneously, $f_1^{4A} = 4.648 \pm 0.007$ GHz, $f_1^{4B} = 5.830 \pm 0.007$ GHz, and $f_1^{4C} = 7.491 \pm 0.007$ GHz.

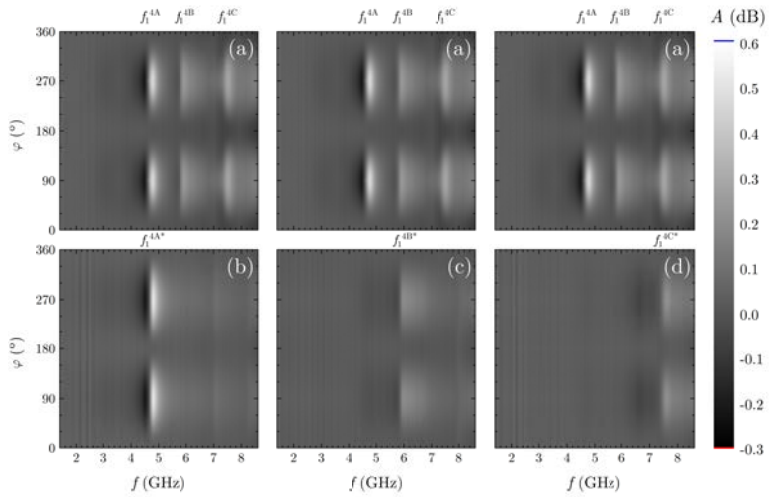

Figure 4.8: Control check measurements for FT2. (a) Absorbance diagram of segments A, B and C when they are all characterized together (both gaps of 1 mm). (b), (c) and (d) Absorbance diagrams of segments A, B and C when each is characterized apart, respectively. Each resonance is univocally associated to one emerging segment: $f_1^{4A} \simeq f_1^{4A*}$, $f_1^{4B} \simeq f_1^{4B*}$ and $f_1^{4C} \simeq f_1^{4C*}$.

4.4 Fracture test analysis

Before addressing the downshift behavior of fracture types I and II, first we will deal with the split and upshift phenomenon exhibited by fracture types III and IV. After analyzing the control check measurements, we understand that fracturing the stent in a number of pieces, makes the fundamental resonance of the intact stent split in the same number of new fundamental resonances, each of which is independent of each other and univocally caused by the corresponding segment.

Once we have figured out the mechanism behind the split of the fundamental resonance frequency, understanding its subsequent upshift is a straightforward step. We just need to recover the semi-empirical model condensed in Equation 3.10:

$$f_n(\ell) = \frac{nc}{2a\ell\sqrt{\varepsilon_r \mu_r}} + f_n^{\text{off}}. \tag{4.1}$$

According to the reciprocal $1/\ell$ dependence in this equation, the fundamental resonance frequencies from the emerging segments shall shift up with respect to the original resonance. Let us go one step further and try to get quantitative information about the status of type III- and IV-fractured stents from the estimates of their split frequencies. In order to do that, we need to isolate ℓ from Equation 4.1:

$$\ell(f_n) \equiv \ell_{\mathrm{MWS}}(f_n) = \frac{nc}{2a\sqrt{\varepsilon_r \mu_r}} \frac{1}{(f_n - f_n^{\mathrm{off}})}. \tag{4.2}$$

This expression provides the length of a given stent segment according to MWS, ℓ_{MWS}, in terms of the scaling factor a, the frequency offset f_n^{off} (whose values appear in Table 3.4) and the estimates of any of its characteristic nth-order split frequencies, f_n. Therefore, in addition to qualitatively detect the onset of fracture types III and IV (split and upshift of f_1), we may use Equation 4.2 to compute the lengths of the emerging stent segments and thus provide a quantitative evaluation of single or multiple complete transverse linear ruptures in stents.

4.4.1 FT1: Type III quantitative analysis

We will particularize Equation 4.2 for f_1^{1A} and f_1^{1B} to obtain $\ell_{\mathrm{MWS}}^{\mathrm{1A}}$ and $\ell_{\mathrm{MWS}}^{\mathrm{1B}}$. For completeness, we will particularize also for f_1^{0AB}, $f_1^{\mathrm{1A}^*}$ and $f_1^{\mathrm{1B}^*}$ to compute $\ell_{\mathrm{MWS}}^{\mathrm{0AB}}$, $\ell_{\mathrm{MWS}}^{\mathrm{1A}^*}$ and $\ell_{\mathrm{MWS}}^{\mathrm{1B}^*}$, respectively. Table 4.1 summarizes the quantitative analysis of the type III fracture induced in FT1. In spite of being slightly overestimated, all ℓ_{MWS} values are in good agreement with the corresponding ℓ counterparts obtained using the digital caliper. In all cases, the relative discrepancies between ℓ and ℓ_{MWS} estimates are below the 3% or, talking in absolute terms, below 0.4 mm. This error is below the characteristic strut length, which for the stent used in this fracture test was 1.2 mm. Therefore, according to FT1 we could state that MWS was able to detect a type III SF with "sub-strut length" accuracy and thus, this technique is capable of locating the precise crown on which the stent suffered a transverse linear rupture.

Cut	Segment	f_1 (GHz)	ℓ_{MWS} (mm)	ℓ (mm)
0	AB	2.309 ± 0.005	31.3 ± 1.3	30.77 ± 0.04
1	A	3.407 ± 0.006	18.7 ± 0.6	18.58 ± 0.05
	A*	3.391 ± 0.007	18.8 ± 0.6	
	B	4.778 ± 0.008	12.4 ± 0.3	12.16 ± 0.03
	B*	4.746 ± 0.006	12.5 ± 0.3	

Table 4.1: Summary of the data obtained from FT1. From left to right, columns indicate cut number, segment label, fundamental resonance frequency (f_1), stent length determined using Equation 4.2 (ℓ_{MWS}), and stent length measured using a digital caliper (ℓ). Asterisks (*) indicate stent segments individually characterized.

4.4.2 FT2: Types III and IV quantitative analysis

For FT2 we can proceed analogously as we have done for FT1. First we will particularize Equation 4.2 for the frequencies found after cuts 3 and 4, $f_1^{3\mathrm{A}}$, $f_1^{3\mathrm{BC}}$, $f_1^{4\mathrm{A}}$, $f_1^{4\mathrm{B}}$ and $f_1^{4\mathrm{C}}$, to obtain the corresponding lengths according to MWS, $\ell_{\mathrm{MWS}}^{3\mathrm{A}}$, $\ell_{\mathrm{MWS}}^{3\mathrm{BC}}$, $\ell_{\mathrm{MWS}}^{4\mathrm{A}}$, $\ell_{\mathrm{MWS}}^{4\mathrm{B}}$ and $\ell_{\mathrm{MWS}}^{4\mathrm{C}}$. Once again and just for completeness, we will also use $f_1^{3\mathrm{BC}*}$, $f_1^{4\mathrm{A}*}$, $f_1^{4\mathrm{B}*}$ and $f_1^{4\mathrm{C}*}$, to compute the associated $\ell_{\mathrm{MWS}}^{3\mathrm{BC}*}$, $\ell_{\mathrm{MWS}}^{4\mathrm{A}*}$, $\ell_{\mathrm{MWS}}^{4\mathrm{B}*}$ and $\ell_{\mathrm{MWS}}^{4\mathrm{C}*}$, respectively. Table 4.2 summarizes the quantitative analysis of type III and type IV ruptures induced in FT2. This time we notice that all ℓ_{MWS} values are significantly overestimated with respect to the corresponding ℓ counterparts obtained from direct measurement. In most cases we found relative discrepancies ranging from 10% to 22%, with only $\ell_{\mathrm{MWS}}^{3\mathrm{BC}}$ exceeding this last value with a remarkable 37%. In any case, unless this exception, we consider all relative discrepancies moderate because in absolute terms they never exceed 1.8 mm. This means an uncertainty below two strut lengths (the strut length for the stent used in this fracture test was 1.2 mm). From FT2 we first could conclude that MWS is able to provide signs of presence of both fracture types III and IV. In addition, the location of each transverse linear rupture present after the fourth cut has been obtained with an uncertainty around one crown. However, the position of the single transverse linear rupture after the third cut has not been as accurate, predominantly on the part of $\ell_{\mathrm{MWS}}^{3\mathrm{BC}}$. The

Cut	Segment	f_1 (GHz)	ℓ_{MWS} (mm)	ℓ (mm)
0	ABC	2.647 ± 0.004	24.8 ± 1.1	24.91 ± 0.03
1	ABC	2.332 ± 0.004	29.3 ± 1.5	24.72 ± 0.04
2	ABC	2.203 ± 0.003	31.7 ± 1.7	24.66 ± 0.04
3	A	4.643 ± 0.008	12.5 ± 0.4	11.17 ± 0.03
	A*	4.631 ± 0.006	12.5 ± 0.4	
	BC	3.162 ± 0.004	19.8 ± 0.8	14.40 ± 0.03
	BC*	3.236 ± 0.003	19.2 ± 0.7	
4	A	4.648 ± 0.007	12.5 ± 0.4	11.17 ± 0.03
	A*	4.631 ± 0.006	12.5 ± 0.4	
	B	5.830 ± 0.007	9.6 ± 0.3	7.93 ± 0.05
	B*	5.861 ± 0.010	9.6 ± 0.3	
	C	7.491 ± 0.007	7.3 ± 0.2	6.64 ± 0.02
	C*	7.514 ± 0.012	7.3 ± 0.2	

Table 4.2: Summary of the data obtained from FT2. From left to right, columns indicate cut number, segment label, fundamental resonance frequency (f_1), stent length determined using Equation 4.2 (ℓ_{MWS}), and stent length measured using a digital caliper (ℓ). Asterisks (*) indicate stent segments individually characterized.

reasons for this mismatch will be better understood after analyzing fracture types I and II.

4.4.3 FT2: Types I and II qualitative analysis

Our hypothesis to explain the downshift behavior observed at fracture types I and II is that the natural path followed by the standing electric current induced along stent crowns becomes partially truncated by each cut. According to this, the resonant current distribution would be compelled to take an alternative route around cutting points, which always would be longer than the original. Therefore, this effective lengthening experienced by the current path would result in the observed f_1 downshift. Alternatively, we can read this in terms of the stent characteristic scaling factor a. In Chapter 3 we have shown that a is proportional to how circuitous the architecture of a given stent is; the more truncated the architecture is, the higher a would be. With this in mind, it results reasonable to think that the

effective architecture resulting from cut 1 would be more intricate than the original, especially when we remember that this first cut was applied just beneath a welding point (see Figure 4.4b). Similarly, the effective architecture emerging after cut 2 (see Figure 4.4c) would be a bit more tortuous.

In agreement with that, along FT2 we would have $a_\alpha \simeq a_\alpha^{0\mathrm{ABC}} \lesssim a_\alpha^{1\mathrm{ABC}} \lesssim a_\alpha^{2\mathrm{ABC}}$, where $a_\alpha = 2.98 \pm 0.08$ is the scaling factor of the intact stent determined in Chapter 3, and super-index tags on subsequent effective scaling factors denote corresponding FT2 stages. According to Equation 4.1, one might think that the downshift could be due to an occasional increase of the stent length caused by mechanical stress during the cutting process. This can be immediately disregarded just by checking Table 4.2, where we may notice how cuts 1 and 2 cause instead a slight decrease of the stent length, $\ell^{0\mathrm{ABC}} \gtrsim \ell^{1\mathrm{ABC}} \gtrsim \ell^{2\mathrm{ABC}}$. In particular, the length of the intact stent diminishes from $\ell^{0\mathrm{ABC}} = 24.91 \pm 0.03$ mm to $\ell^{1\mathrm{ABC}} = 24.72 \pm 0.04$ mm after cut 1, reaching $\ell^{2\mathrm{ABC}} = 24.66 \pm 0.04$ mm after cut 2. Therefore, the hypothetical upshift of stent resonance frequencies caused by this mechanical shortening is eventually overcome by the downshift associated with the electric current detouring.

After this reasoning, we can now jump back to the unusual mismatch between $\ell^{3\mathrm{BC}}$ and $\ell_{\mathrm{MWS}}^{3\mathrm{BC}}$ mentioned in the previous subsection. In contrast to segments A and B emerging after cut 1 in FT1, segment BC arising from cut 3 in FT2 carries a fractured strut produced by preceding cut 2. Therefore, we should better consider segment BC as a type I-fractured stent piece (single strut fracture on crown #15). Thus, in line with our conjecture accounting for the downshift behavior observed at lower fracture types, this simple observation would explain the unexpectedly low value obtained for $f_1^{3\mathrm{BC}}$ and the subsequent mismatch between $\ell^{3\mathrm{BC}}$ and $\ell_{\mathrm{MWS}}^{3\mathrm{BC}}$.

4.5 Conclusions

Along this chapter we have tested the ability of our MWS-based approach for the detection of SFs. We have shown that absorbance diagrams generated by ruptured stents provide indicators for fracture types I, II, III and IV:

- Type I: Downshift of f_1.

- Type II: Downshift of an already downshifted f_1.
- Type III: Split and upshift of f_1.
- Type IV: Split and upshift of an already split-and-upshifted f_1.

On the one hand, the downshift marker established for fracture types I and II is merely qualitative at this stage and therefore MWS just warns of single or multiple broken struts. In any case, the door leading to a quantitative assessment of lower fracture types could be opened. We believe that the key is hidden in the interconnection between stent architecture and its characteristic scaling factor a. We can empirically estimate a for a certain stent architecture but, it is possible to do it numerically from the geometrical characteristics of that architecture (modular element design, welding pattern, etcetera)? If that were the case, how would the value of a increase for a given broken strut distribution? Is this hypothetical increase univocally associated with each possible broken strut distribution?

On the other hand, the split and upshift marker established for fracture types III and IV has enabled the quantitative assessment of higher fracture types from the beginning. The results achieved in both FT1 and FT2 demonstrate that, in the worst case, MWS is able to establish the precise site on which the stent has suffered a transverse linear rupture with an uncertainty of a single crown. In addition, we think that the numerical approach previously surmised for fracture types I and II would actually enhance the accuracy of the evaluation of fracture types III and IV. However, there is work pending in regard to the study of fracture type V or more complex geometrical distortions such as arbitrary combinations of fracture types I, II, III and IV.

References

[1] P. S. Chowdhury, and R. G. Ramos, "Coronary-stent fracture," New England Journal of Medicine **347**, 581–581 (2002) (cit. on p. 69).

[2] G. Sianos, S. Hofma, J. M. Ligthart, F. Saia, A. Hoye, P. A. Lemos, and P. W. Serruys, "Stent fracture and restenosis in the drug-eluting stent era," Catheterization and Cardiovascular Interventions **61**, 111–116 (2004) (cit. on p. 70).

[3] H. Tizón-Marcos, R. De Larochellière, and E. Larose, "Breakpoint: left main stent fracture - review of the literature," Journal of Interventional Cardiology **22**, 362–367 (2009) (cit. on p. 70).

[4] A. K. Chhatriwalla, A. Cam, S. Unzek, D. L. Bhatt, R. E. Raymond, A. M. Lincoff, P. L. Whitlow, S. G. Ellis, E. M. Tuzcu, and S. R. Kapadia, "Drug-eluting stent fracture and acute coronary syndrome," Cardiovascular Revascularization Medicine **10**, 166–171 (2009) (cit. on p. 70).

[5] S. Adlakha, M. Sheikh, J. Wu, M. W. Burket, U. Pandya, W. Colyer, E. Eltahawy, and C. J. Cooper, "Stent fracture in the coronary and peripheral arteries," Journal of interventional cardiology **23**, 411–419 (2010) (cit. on p. 70).

[6] T. Canan, and M. S. Lee, "Drug-eluting stent fracture: incidence, contributing factors, and clinical implications," Catheterization and Cardiovascular Interventions **75**, 237–245 (2010) (cit. on p. 70).

[7] T. Chakravarty, A. J. White, M. Buch, H. Naik, N. Doctor, J. Schapira, S. Kar, J. S. Forrester, R. E. Weiss, and R. Makkar, "Meta-analysis of incidence, clinical characteristics and implications of stent fracture," American Journal of Cardiology **106**, 1075–1080 (2010) (cit. on p. 70).

[8] M. Chinikar, and P. Sadeghipour, "Coronary stent fracture: a recently appreciated phenomenon with clinical relevance," Current Cardiology Reviews **10**, 349–354 (2014) (cit. on p. 70).

[9] R. Acar, M. Bulut, and M. Akcakoyun, "Are we aware of stent fracture?" Herz **40**, 417–422 (2015) (cit. on p. 70).

[10] A. Omar, L. K. Pendyala, J. A. Ormiston, and R. Waksman, "Review: stent fracture in the drug-eluting stent era," Cardiovascular Revascularization Medicine **17**, 404–411 (2016) (cit. on p. 70).

[11] M. S. Lee, D. Jurewitz, J. Aragon, J. Forrester, R. R. Makkar, and S. Kar, "Stent fracture associated with drug-eluting stents: clinical characteristics and implications," Catheterization and Cardiovascular Interventions **69**, 387–394 (2007) (cit. on pp. 70, 71, 73).

[12] W.-S. Chung, C.-S. Park, K.-B. Seung, P.-J. Kim, J.-M. Lee, B.-K. Koo, Y.-S. Jang, J.-Y. Yang, J.-H. Yoon, D.-I. Kim, Y.-W. Yoon, J.-S. Park, Y.-H. Cho, and S.-J. Park, "The incidence and clinical impact of stent strut fractures developed after drug-eluting stent implantation," International Journal of Cardiology **125**, 325–331 (2008) (cit. on pp. 70, 73).

[13] H. Doi, A. Maehara, G. S. Mintz, K. Tsujita, T. Kubo, C. Castellanos, J. Liu, J. Yang, C. Oviedo, J. Aoki, T. Franklin-Bond, N. Dasgupta, A. J. Lansky, G. D. Dangas, G. W. Stone, J. W. Moses, R. Mehran, and M. B. Leon, "Classification and potential mechanisms of intravascular ultrasound patterns of stent fracture," American Journal of Cardiology **103**, 818–823 (2009) (cit. on pp. 70–73).

[14] H.-S. Kim, Y.-H. Kim, S.-W. Lee, D.-W. Park, C. W. Lee, M.-K. Hong, S.-W. Park, J.-K. Ko, J.-H. Park, J.-H. Lee, S. W. Choi, I.-W. Seong, Y. H. Cho, N.-H. Lee, J. H. Kim, K.-J. Chun, and S.-J. Park, "Incidence and predictors of drug-eluting stent fractures in long coronary disease," International Journal of Cardiology **133**, 354–358 (2009) (cit. on pp. 70, 72).

[15] T. Kawai, H. Umeda, M. Ota, K. Hattori, M. Ishikawa, M. Okumura, S. Kan, T. Nakano, H. Naruse, S. Matsui, J. Ishii, H. Hishida, and Y. Ozaki, "Do drug elution components increase the risk of fracture of sirolimus-eluting stents?" Coronary artery disease **21**, 298–303 (2010) (cit. on pp. 70, 72).

[16] H. Umeda, T. Kawai, N. Misumida, T. Ota, K. Hayashi, M. Iwase, H. Izawa, S. Sugino, T. Shimizu, Y. Takeichi, R. Ishiki, H. Inagaki, Y. Ozaki, and T. Murohara, "Impact of sirolimus-eluting stent fracture on 4-year clinical outcomes," Circulation:

Cardiovascular Interventions **4**, 349–354 (2011) (cit. on pp. 70, 72).

[17] J. Aoki, G. Nakazawa, K. Tanabe, A. Hoye, H. Yamamoto, T. Nakayama, Y. Onuma, Y. Higashikuni, S. Otsuki, A. Yagishita, S. Yachi, H. Nakajima, and K. Hara, "Incidence and clinical impact of coronary stent fracture after sirolimus-eluting stent implantation," Catheterization and Cardiovascular Interventions **69**, 380–386 (2007) (cit. on pp. 70, 73).

[18] F. Shaikh, R. Maddikunta, M. Djelmami-Hani, J. Solis, S. Allaqaband, and T. Bajwa, "Stent fracture, an incidental finding or a significant marker of clinical in-stent restenosis?" Catheterization and Cardiovascular Interventions **71**, 614–618 (2008) (cit. on pp. 70, 72).

[19] Y. Ino, Y. Toyoda, A. Tanaka, S. Ishii, Y. Kusuyama, T. Kubo, S. Takarada, H. Kitabata, T. Tanimoto, M. Mizukoshi, T. Imanishi, and T. Akasaka, "Predictors and prognosis of stent fracture after sirolimus-eluting stent implantation," Circulation Journal **73**, 2036–2041 (2009) (cit. on pp. 70–72).

[20] S. E. Lee, M. H. Jeong, I. S. Kim, J. S. Ko, M. G. Lee, W. Y. Kang, S. H. Kim, D. S. Sim, K. H. Park, N. S. Yoon, H. J. Yoon, K. H. Kim, Y. J. Hong, H. W. Park, J. H. Kim, Y. k. Ahn, J. G. Cho, J. C. Park, and J. C. Kang, "Clinical outcomes and optimal treatment for stent fracture after drug-eluting stent implantation," Journal of Cardiology **53**, 422–428 (2009) (cit. on pp. 70, 71).

[21] K. W. Park, J. J. Park, I.-H. Chae, J.-B. Seo, H.-M. Yang, H.-Y. Lee, H.-J. Kang, Y.-S. Cho, T.-J. Yeon, W.-Y. Chung, B.-K. Koo, D.-J. Choi, B.-H. Oh, Y.-B. Park, and H.-S. Kim, "Clinical characteristics of coronary drug-eluting stent fracture: insights from a two-center des registry," Journal of Korean Medical Science **26**, 53–58 (2011) (cit. on pp. 70, 72, 73).

[22] M.-W. Park, K. Chang, S. H. Her, J.-M. Lee, Y.-S. Choi, D.-B. Kim, P. J. Kim, J. S. Cho, M. S. Choi, J. Y. Baek, C.-S. Park, S. G. Yoon, W. S. Chung, and K. B. Seung, "Incidence and clinical impact of fracture of drug-eluting stents widely used in current clinical practice: comparison with initial platform

of sirolimus-eluting stent," Journal of Cardiology **60**, 215–221 (2012) (cit. on pp. 70, 72, 73).

[23] S. Kuramitsu, M. Iwabuchi, T. Haraguchi, T. Domei, A. Nagae, M. Hyodo, K. Yamaji, Y. Soga, T. Arita, S. Shirai, K. Kondo, K. Ando, K. Sakai, M. Goya, Y. Takabatake, S. Sonoda, H. Yokoi, F. Toyota, H. Nosaka, and M. Nobuyoshi, "Incidence and clinical impact of stent fracture after everolimus-eluting stent implantation," Circulation: Cardiovascular Interventions **5**, 663–671 (2012) (cit. on pp. 70–72).

[24] K. Kozuma, T. Kimura, K. Kadota, S. Suwa, K. Kimura, M. Iwabuchi, K. Kawai, A. Miyazawa, M. Kawamura, K. Nakao, R. Asano, T. Yamamoto, N. Suzuki, J. Aoki, H. Kyono, G. Nakazawa, K. Tanabe, Y. Morino, and K. Igarashi, "Angiographic findings of everolimus-eluting as compared to sirolimus-eluting stents: angiographic sub-study from the randomized evaluation of sirolimus-eluting versus everolimus-eluting stent trial (RESET)," Cardiovascular Intervention and Therapeutics **28**, 344–351 (2013) (cit. on p. 70).

[25] J. Giri, and M. D. Saybolt, "Coronary stent fracture: a new form of patient-prosthesis mismatch?" JACC: Cardiovascular Interventions **9**, 1124–1126 (2016) (cit. on p. 70).

[26] H. S. Hecht, S. Polena, V. Jelnin, M. Jimenez, T. Bhatti, M. Parikh, G. Panagopoulos, and G. Roubin, "Stent gap by 64-detector computed tomographic angiography: relationship to in-stent restenosis, fracture, and overlap failure," Journal of the American College of Cardiology **54**, 1949–1959 (2009) (cit. on pp. 70, 73).

[27] D. Alexopoulos, and I. Xanthopoulou, "Coronary stent fracture: how frequent it is? does it matter?" Hellenic journal of cardiology **52**, 1–5 (2011) (cit. on p. 70).

[28] M. Kashiwagi, A. Tanaka, H. Kitabata, Y. Ino, H. Tsujioka, K. Komukai, Y. Ozaki, K. Ishibashi, T. Tanimoto, S. Takarada, T. Kubo, K. Hirata, M. Mizukoshi, T. Imanishi, and T. Akasaka, "Oct-verified neointimal hyperplasia is increased at fracture site in drug-eluting stents," JACC: Cardiovascular Imaging **5**, 232–233 (2012) (cit. on p. 70).

[29] K. C. Koskinas, Y. S. Chatzizisis, A. P. Antoniadis, and G. D. Giannoglou, "Role of endothelial shear stress in stent restenosis and thrombosis: pathophysiologic mechanisms and implications for clinical translation," Journal of the American College of Cardiology **59**, 1337–1349 (2012) (cit. on p. 70).

[30] J. Shite, D. Matsumoto, and M. Yokoyama, "Sirolimus-eluting stent fracture with thrombus, visualization by optical coherence tomography," European Heart Journal **27**, 1389–1389 (2006) (cit. on p. 70).

[31] G. Nakazawa, A. V. Finn, M. Vorpahl, E. Ladich, R. Kutys, I. Balazs, F. D. Kolodgie, and R. Virmani, "Incidence and predictors of drug-eluting stent fracture in human coronary artery: a pathologic analysis," Journal of the American College of Cardiology **54**, 1924–1931 (2009) (cit. on pp. 70, 72, 73).

[32] S.-H. Lee, J.-S. Park, D.-G. Shin, Y.-J. Kim, G.-R. Hong, W. Kim, and B.-S. Shim, "Frequency of stent fracture as a cause of coronary restenosis after sirolimus-eluting stent implantation," American Journal of Cardiology **100**, 627–630 (2007) (cit. on p. 70).

[33] J. J. Popma, K. Tiroch, A. Almonacid, S. Cohen, D. E. Kandzari, and M. B. Leon, "A qualitative and quantitative angiographic analysis of stent fracture late following sirolimus-eluting stent implantation," American Journal of Cardiology **103**, 923–929 (2009) (cit. on pp. 71, 73).

[34] R. Rieu, P. Barragan, V. Garitey, P. O. Roquebert, J. Fuseri, P. Commeau, and J. Sainsous, "Assessment of the trackability, flexibility, and conformability of coronary stents: a comparative analysis," Catheterization and Cardiovascular Interventions **59**, 496–503 (2003) (cit. on p. 72).

[35] D. O. Halwani, P. G. Anderson, B. C. Brott, A. S. Anayiotos, and J. E. Lemons, "The role of vascular calcification in inducing fatigue and fracture of coronary stents," Journal of Biomedical Materials Research Part B: Applied Biomaterials **100B**, 292–304 (2012) (cit. on p. 72).

[36] J. A. Ormiston, B. Webber, and M. W. Webster, "Stent longitudinal integrity bench insights into a clinical problem," JACC: Cardiovascular Interventions **4**, 1310–1317 (2011) (cit. on p. 72).

[37] J. A. Ormiston, B. Webber, J. White, B. Ubod, and M. W. Webster, "Stent susceptibility to fracture. An independent bench comparison of 6 contemporary stent designs using a repetitive bend test," in EuroPCR 2013 (2013) (cit. on p. 72).

[38] K. Iwasaki, S. Kishigami, J. Arai, T. Ohba, T. Yamamoto, Y. Hikichi, and U. M., "Flexibility and stent fracture potentials against cyclically bending coronary artery motions: comparison between 2-link and 3-link DESs," in EuroPCR 2013 (2013) (cit. on p. 72).

[39] D. Leong, B. Dundon, R. Puri, and R. Yeend, "Very late stent fracture associated with a sirolimus-eluting stent," Heart, Lung and Circulation **17**, 426–428 (2008) (cit. on p. 73).

[40] D. Allie, C. Hebert, and C. Walker, "Nitinol stent fractures in the SFA: The biomechanical forces exerted on the SFA provide a "stiff" challenge to endovascular stenting," Endovascular Today **3**, 22–24 (2004) (cit. on p. 73).

[41] M. Jaff, M. Dake, J. Pompa, G. Ansel, and T. Yoder, "Standardized evaluation and reporting of stent fractures in clinical trials of noncoronary devices," Catheterization and Cardiovascular Interventions **70**, 460–462 (2007) (cit. on p. 73).

[42] D. Scheinert, S. Scheinert, J. Sax, C. Piorkowski, S. Bräunlich, M. Ulrich, G. Biamino, and A. Schmidt, "Prevalence and clinical impact of stent fractures after femoropopliteal stenting," Journal of the American College of Cardiology **45**, 312–315 (2005) (cit. on p. 73).

[43] *Driver sprint rapid exchange coronary stent system, Instructions for use*, Revision B (2011) (cit. on p. 74).

[44] *Endeavor sprint rapid exchange zotarolimus-eluting coronary stent system, Instructions for use*, Revision A (2011) (cit. on p. 74).

5

In-stent neoatherosclerosis

In Chapter 1 we have briefly introduced how atherosclerosis alters the normal layered organization of a healthy artery wall. We have shown how their native cells and extracellular matrix are gradually replaced by large lipidic accumulations as the atherosclerotic lesion progresses. Consequently, the initial polar character of the tissue should switch to a rather apolar one resulting in a gradual reduction of its average relative permittivity, just as we have discussed at the end of Chapter 3. Since, changes in the dielectric properties around a stent are able to alter its corresponding resonances, in principle microwave spectrometry could report the advent of in-stent neoatherosclerosis: the relapse of a completely *de novo* atherosclerotic lesion around an implanted stent. In this chapter, we assess the prospects of microwave spectrometry in a worsening in-stent neoatherosclerosis scenario by means of a "cholesterol test". The idea of this test is to submit a stent to a staged process of increasing cholesterol deposition and, after each step, characterize the stent-cholesterol construct with the microwave spectrometry setup. By monitoring the course of the resulting absorbance diagrams, we will see that the presence of a few milligrams of cholesterol around the stent is enough to alter its characteristic resonances.

5.1 In-stent neoatherosclerosis

In Chapter 1 we introduced the problem of atherosclerosis and how stenting became the preferred medical intervention to revascularize

atherosclerotic vessels. Since the onset of atherosclerosis precedes the stent deployment, one might think that the atherosclerotic transformation of the neointima artery layer should be independent of whether the stent is already present or not. At the present time, however, it is well known that an implanted stent may trigger a completely *de novo* atherosclerosis process around target lesion location [1–3]. This phenomenon, baptized by Kang and coauthors as in-stent neoatherosclerosis [4], has recently attracted considerable attention [5–7]. In-stent neoatherosclerosis (ISNA) is defined as the transformation process of the neointima artery layer around a stent from normal to atherosclerotic. Figure 5.1 sketches the course of the atherosclerotic transformation inside a previously deployed stent. This situation results in chronic neointimal inflammation and a subsequent lumen area reduction due to the formation of a type of vulnerable atheroma plaque known as thin-cap fibroatheroma [8]. In addition to representing a risk *per se*, there is emerging evidence that ISNA also plays an important role in the onset of several late stent-related complications. Nowadays, the presence of ISNA is assessed using invasive methods, mainly with angioscopy and OCT [9]. In this regard, a successful implementation of MWS for a non-invasive diagnosis of the atherosclerotic transformation would enable to anticipate the onset of ISNA-induced stent-related complications.

5.1.1 Incidence and medical implications

At present there is lack of comprehensive studies reviewing the incidence of ISNA. In a retrospective study using OCT, Yonetsu and coauthors provided rates of 33% for BMSs and 57% for DESs [11]. In a retrospective autopsy study Nakazawa and coauthors found rates of 16% for BMSs and 31% for DESs [12]. Despite the different rate values, both works indicated a significantly higher incidence of ISNA among DESs when compared with BMSs. In their subsequent works, Yonetsu *et al.* [13] and Vergallo *et al.* [14] studied the time course of ISNA by quantifying its incidence at three temporal phases of the follow-up period. Counting from the stenting date, they established an early phase (less than 9 months), a mid phase (between 9 and 48 months) and a late phase (beyond 48 months). Table 5.1 summarizes the early, mid and late ISNA incidence rates for BMSs and DESs reported in these works. Notice how the incidence for both stent

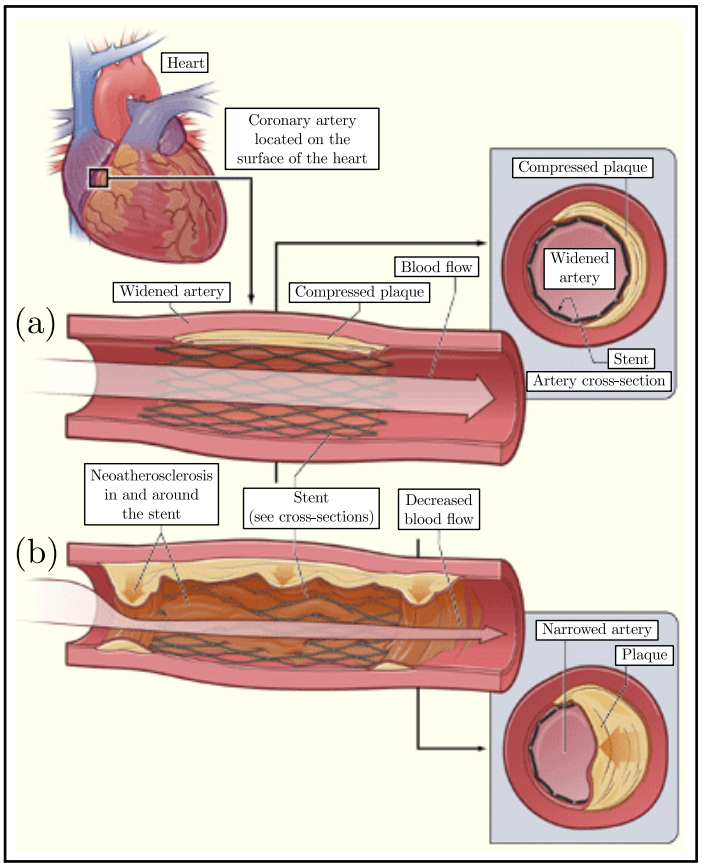

Figure 5.1: Sketch of ISNA development. (a) After stent deployment, the atheroma plaque is compressed and stabilized. (b) Eventually, the neointima artery layer of the stented artery segment may experience a new atherosclerotic transformation, and as a consequence, the blood flow is decreased. Adapted from the National Heart, Lung, and Blood Institute; National Institute of Health; U.S. Department of Health and Human Services [10].

Author	Stent type	Incidence rate (%)		
		Early	Mid	Late
Yonetsu [13]	BMS	8	28	77
	DES	37	63	75
Vergallo [14]	BMS	11.8	25.8	71.4
	DES	36.9	59.3	76.0

Table 5.1: Time course of ISNA according to the bibliography. Early (< 9 months), mid ($9 - 48$ months) and late (> 48 months) ISNA incidence rates for BMSs and DESs reported by Yonetsu [13] and Vergallo [14].

types increases with time up to over a 70%. In addition, the incidence of ISNA at early and mid phases is significantly larger for DESs than for BMSs. These results confirm previous findings stating that ISNA occurs earlier and more frequently in modern DESs than in BMSs [11, 12].

Many stent failure modalities are directly associated with the advent of ISNA, especially at late and very late stages of stent lifetime. Several studies have demonstrated that ISNA significantly increases the risk of ISR [14, 15]. The mechanism for the neointimal hyperplasia following the onset of atherosclerotic transformation is not fully understood. It has been suggested that both processes might be provoked by similar mechanisms, such as chronic inflammation and intravascular injury [16]. The accumulation of lipids and foamy macrophages typical of ISNA is presumably associated with the increase of plaque burden, which in turn would contribute to the development of ISR. Additionally, ISNA has also been linked with late (between 1 and 12 months) and very late (beyond 12 months) stent thrombosis [17–19]. It is fairly accepted that the underlying mechanism behind these ISNA-induced late thrombotic events is the disruption of the thin-cap fibroatheroma [20–22].

5.1.2 Risk factors and mechanism

The risk factors and the mechanism for the onset of ISNA are unclear. As native and *de novo* atherosclerotic transformations lead to plaque formation, one might think that both should be sustained by analogous processes. However, while native atherosclerosis evolves

over decades, ISNA may manifest just a few months after stenting [12]. This fact suggests different underlying principles in each case. It is believed that the major mechanism behind ISNA is a synergistic combination of the arterial injury produced during stent deployment and the local blood flow disturbances caused by the stent presence itself [23].

On the one hand, arterial injury is an inevitable consequence of all interventional coronary procedures which ultimately lead to the disruption of the endothelium artery layer [24–26]. As we introduced in Chapter 1, endothelial dysfunction creates a proinflammatory and procoagulant environment with impaired vasodilatation capability. In addition, the cellular denudation of the endothelium increases its permeability and this allows plasma lipoproteins to easily penetrate into the artery wall. The presence of these molecules within the neointima would actually make a perfect substrate for the onset of ISNA. On the other hand, stents alter the normal hemodynamics in the artery lumen locally [27]. The mere presence of a stent strut in the path of the bloodstream promotes the formation of turbulent flow regions with recirculation and prolonged residence time. At this point it is easy to understand that the combined effects of the endothelial dysfunction and the alteration of normal hemodynamics conspire to induce atherosclerotic transformation. An extended residence time around an endothelium with exaggerated permeability would provide an uncontrolled lipoprotein uptake for the neointima which in turn would finally trigger its atherosclerotic transformation. This hypothesis would also explain the different time course of the atherosclerotic transformation between BMSs and DESs. The antiproliferative drugs delivered by DESs might block the normal arterial healing. This would lead to an extended period with endothelial dysfunction which in turn would eventually precipitate the onset of ISNA.

5.2 Cholesterol test description

We choose cholesterol as a representative component of the plaque resulting from the atherosclerotic transformation. Within an atherosclerotic neointima we can found this organic molecule mainly as a cholesteryl ester, such as cholesteryl linoleate, but also as aggregates of tiny crystals of pure cholesterol. We performed four choles-

terol tests, each on a separated stent chosen among those presented in Table 3.1. All selected stents were MDS with nominal diameter $d_{\text{nom}} = 2.50$ mm. Their corresponding nominal lengths were $\ell_{\text{nom}} = 12$ mm (two duplicates tagged as A and B), 14 mm and 18 mm. We carried out the first cholesterol test (CT1) on the stent with nominal length 12 mm (duplicate A) and the remaining ones (CT2, CT3 and CT4) on the stents with nominal lengths 12 mm (duplicate B), 14 mm and 18 mm, respectively. As usual, we used a compatible inflation device[1] to expand each stent up to nominal inflation pressure, $p = p_{\text{nom}} = 9.0 \pm 0.5$ atm, with the aim of reaching the corresponding nominal size [28]. The four stents were submitted to a gradual process of increasing cholesterol deposition in order to simulate a worsening ISNA scenario. We devised this procedure with three separated phases: A first Pre-cholesterol phase (Pre-phase), a second Cholesterol phase (Ch-phase) divided in several subphases, and a third Post-cholesterol phase (Post-phase). Figure 5.2 sketches the entire cholesterol test protocol.

In the initial Pre-phase, we acquired the absorbance diagram of the running stent directly in order to extract its fundamental resonance frequency, f_1^{Pre}. We also used a digital balance[2] to measure the initial cholesterol mass, m_{Pre}, as well as a digital caliper[3] and a digital micrometer[4] to determine its actual length, ℓ_{Pre}, and diameter, d_{Pre}. The cholesterol deposition process itself began at the subsequent Ch-phase, which was divided in several subphases. The first Cholesterol subphase (Ch1-subphase) began by pouring droplets of a saturated dilution of cholesterol[5] in ethanol[6] directly over the stent and waiting for solvent evaporation. We applied a constant nitrogen gas flow around the dilution-soaked stent with the aim of speeding solute deposition. As ethanol evaporated, the cholesterol precipitated and formed crystals that grew between stent struts and thus filled the stent cells. The resulting construct contained a few milligrams of cholesterol arranged in a well-shaped cylindrical shell that resembled a tube with stained glass walls. The micropicture shown in Figure 5.3

[1] Encore 26 Advantage Kit, Boston Scientific, Natick, MA, USA.
[2] MI 220 CBC, Cobos Precision, L'Hospitalet de Llobregat, Barcelona, Spain.
[3] IP67, Vogel, Kevelaer, Nordrhein-Westfalen, Germany.
[4] IP65, Vogel, Kevelaer, Nordrhein-Westfalen, Germany.
[5] Cholesterol 94%, Sigma-Aldrich, St. Louis, MO, USA.
[6] Ethanol 96%, Panreac Química, Castellar del Vallès, Barcelona, Spain.

highlights the growth of the cholesterol crystals around stent crowns. Then we measured the cholesterol mass deposited in the construct, m_{Ch1}, and we recorded its fundamental resonance frequency, f_1^{Ch1}, from the corresponding absorbance diagram. This protocol can be repeated since the initial cholesterol glassy-like layer serves as a scaffold for the second Cholesterol subphase (Ch2-subphase), and so forth for the subsequent subphases up to the last Cholesterol subphase (ChN-subphase). The dendritic growth of crystals upon the previous ones will gradually thicken the cylindrical shell until a porous cholesterol crust forms. The ChN-subphase is set when the crust is around 1 mm thick, which for $d_{\mathrm{nom}} = 2.50$ mm corresponds to a stent lumen occlusion of about 2/3. Each stent may require a different number of Cholesterol subphases to reach this endpoint due to the random growth of crystals.

Finally, in the Post-phase we used repeated baths of ethanol at 60°C to remove the whole crust present at the end of the process. Once completely cleaned, we collected the absorbance diagram of the stent and extracted its fundamental resonance frequency, f_1^{Post}. In the same way as we had done in the Pre-phase, we also acquired the final cholesterol mass present in the stent, m_{Post}, and its dimensions, ℓ_{Post} and d_{Post}. These last measurements along with the ones performed in the starting phase served as a control check for the entire test. The analysis of this control check will allow us to ensure that only the presence of cholesterol is responsible for the results obtained and thus to discard possible uncontrolled effects like accidental mechanical deformation of the stent.

5.2.1 CT1: Frequency downshift

With the aim of representing the general results found in the four cholesterol test performed, we decided to address CT1 in more detail. This first cholesterol test was conducted on the MDS stent with nominal length 12 mm (duplicate A). The Ch-phase of this test comprised a total of ten subphases ($N = 10$). Figure 5.4 summarizes CT1 by showing five illustrative steps reached along the process. Represented stages are the initial Pre-phase, the subsequent Ch3-, Ch6- and Ch9-subphases, and the final Post-phase. For each stage, the absorbance diagram between 4.2 GHz and 5.2 GHz highlights the region in which the fundamental resonance of this stent takes

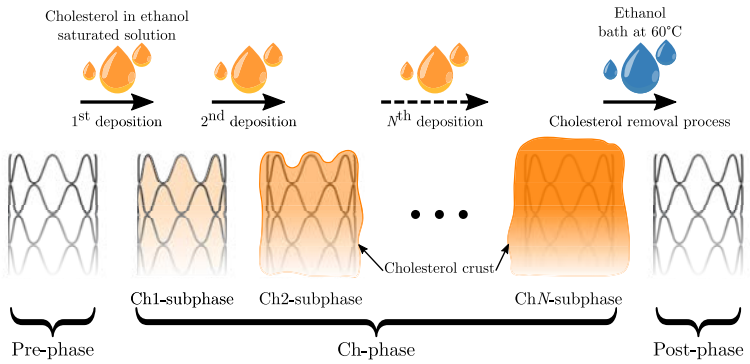

Figure 5.2: Cholesterol test protocol. Series of sketches for the process of cholesterol deposition followed to emulate ISNA. This procedure starts at the Pre-phase, continues with a gradual Ch-phase divided in several subphases, and ends at the Post-phase.

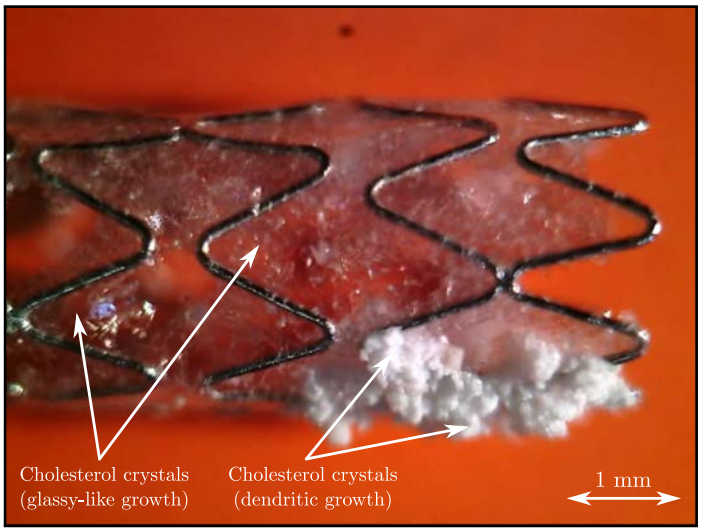

Figure 5.3: Microphotograph of the extreme of a MDS with nominal size 18 mm × 2.50 mm at the Ch1-subphase. Notice the two types of growth exhibited by cholesterol crystals, glassy-like and dendritic.

place. Side and axial micropictures illustrating the progress of the cholesterol crust during the test are also included.

By comparing those absorbance diagrams going from the Pre-phase to the Ch10-subphase, we first observe that the resonance smoothly shifts down as m increases (see Figures 5.4a1 to 5.4d1). Figure 5.5 provides a better insight into this downshift behaviour by detailing the evolution of the resonance along the entire cholesterol test. Figure 5.5a shows the isoangular spectrum at $\varphi = 90°$ for each absorbance diagram measured through CT1. Notice how the resonance gradually tends to lower frequencies as the cholesterol test progresses. Their corresponding f_1 values are represented as a function of m in Figure 5.5b. Notice how the $f_1(m)$ data points establish a decreasing dependence which at the last Ch10-subphase reaches a minimum value of $f_1^{\mathrm{Ch10}} = 4.659 \pm 0.002$ GHz.

5.2.2 CT2, CT3 and CT4

Subsequent CT2, CT3 and CT4 were performed on the stents with nominal lengths 12 mm (duplicate B), 14 mm and 18 mm, respectively. The number of Cholesterol subphases in each case were $N = 6$, 8 and 9, respectively. The results obtained in these three additional cholesterol tests were similar to those of CT1. In all cases, the fundamental resonance of the running stent experienced a gradual drift towards lower frequencies as its corresponding cholesterol test progressed. In order to compare the downshift behavior exhibited by the four stents investigated, we may define the relative frequency displacement of the fundamental resonance (let us call it relative downshift) as

$$\Delta f_1(m) \equiv \frac{f_1(m) - f_1^{\mathrm{Pre}}}{f_1^{\mathrm{Pre}}}, \tag{5.1}$$

where f_1^{Pre} is the fundamental resonance frequency at the Pre-phase, and $f_1(m)$ represents any fundamental resonance frequency measured along a cholesterol test. Figure 5.6 summarizes the four cholesterol tests carried out by representing their $\Delta f_1(m)$ downshift curves. Notice how the experimental data points decrease at similar rates for the two stents sharing the same nominal length of 12 mm (see red squares and green circles). However, the $\Delta f_1(m)$ downshift curves of the stents with nominal lengths 14 mm and 18 mm seem to drop

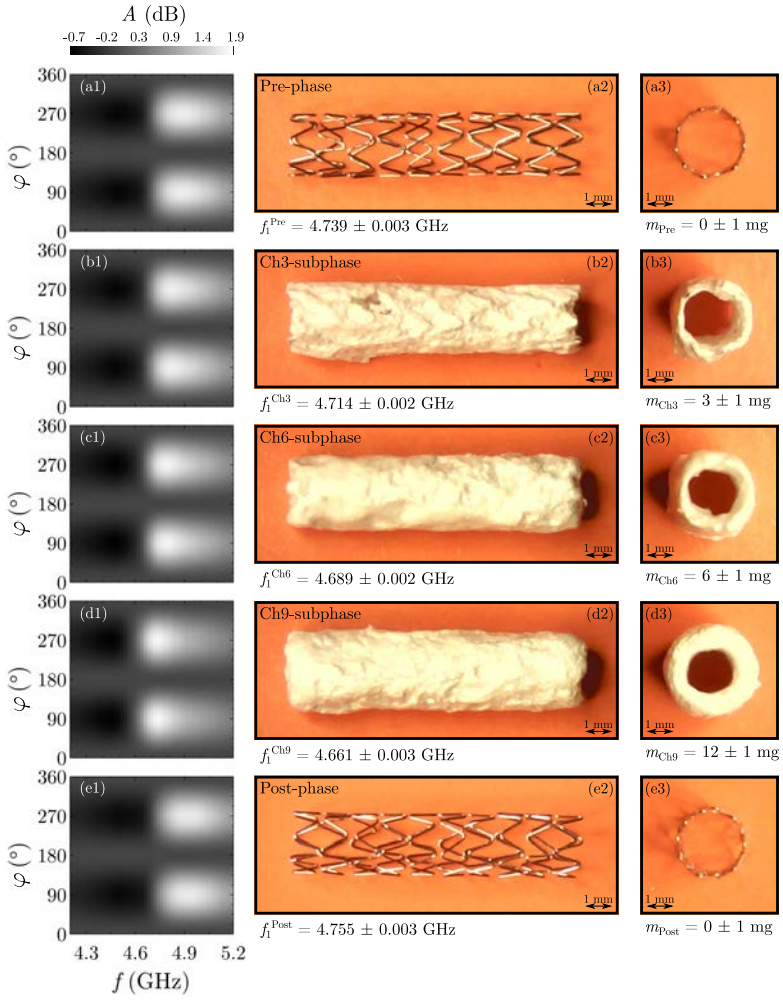

Figure 5.4: Summary of the cholesterol test performed on the MDS with nominal size 12 mm × 2.50 mm (duplicate A). Represented stages are the Pre-phase, the Ch3-, Ch6- and Ch9-subphases, and the Post-phase [labeled top to bottom as (a) to (e), respectively]. For each stage the absorbance diagram showing the fundamental resonance is provided [labeled as (1)]. Side and axial micropictures of the corresponding constructs are also included [labeled left to right as (2) and (3), respectively].

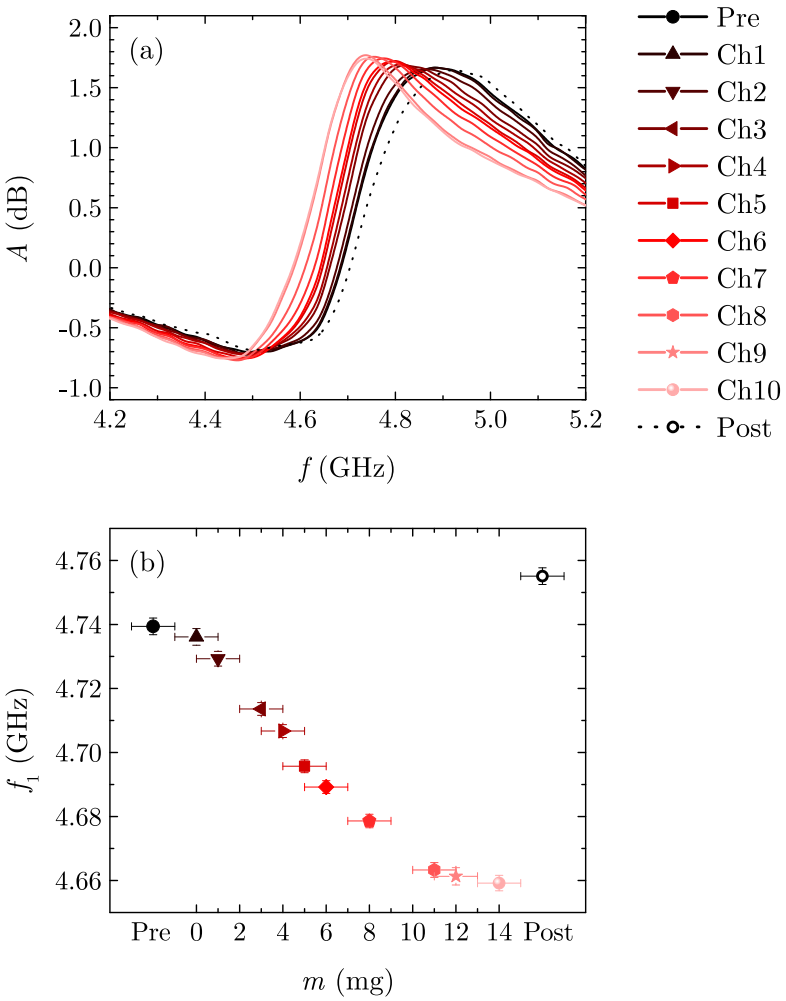

Figure 5.5: Evolution of the fundamental resonance of the MDS with nominal size 12 mm × 2.50 mm (duplicate A) along CT1 (see legend for details). (a) Absorbance spectra at normal incidence ($\varphi = 90°$) for each stage reached during CT1. (b) Fundamental resonance frequency versus the deposited mass of cholesterol, $f_1(m)$.

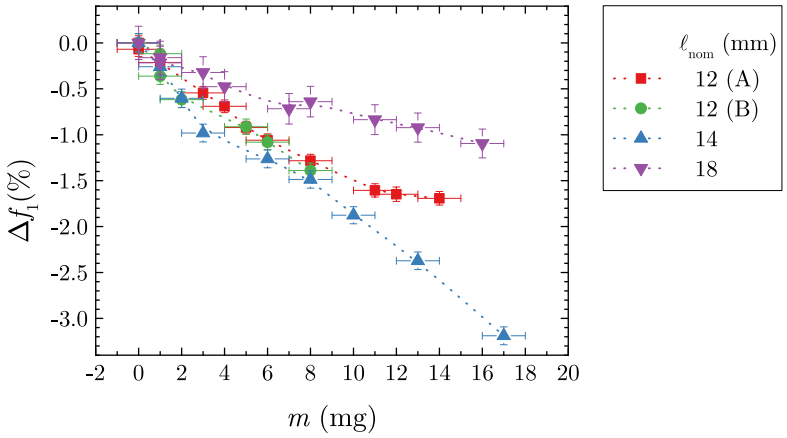

Figure 5.6: Summary of cholesterol tests performed. Relative frequency displacement of the fundamental resonance frequency versus the deposited mass of cholesterol, $\Delta f_1(m)$, for the four MDS stents investigated (see legend for details).

at different paces (see blue up triangles and purple down triangles). Additionally, Table 5.2 compiles the corresponding maximum relative downshifts, $\Delta f_1^{\mathrm{Ch}N}$. Notice how their estimates turn out to be very diverse, ranging from -1.1% to -3.2%. However, in spite of being always small, the four $\Delta f_1^{\mathrm{Ch}N}$ values are significant considering the uncertainties involved.

5.3 Cholesterol tests control check

We know that the characteristic resonance frequency of a stent is very sensitive to its size. Thus, one may think that an eventual variation in stent geometry occurred along a cholesterol test might be behind the downshift behavior observed. Since a hypothetical elongation of stent length could have caused a displacement of the resonance towards lower frequencies, we are interested in validating whether this downshift is truly due to cholesterol presence or not. To this aim, three characteristic stent magnitudes were submitted to cross-check measurements. In particular, we compared the d, ℓ and f_1 estimates measured at the initial Pre-phase with their corresponding counterparts measured at the final Post-phase. In a similar way to what we made to quantify the relative frequency displacement of

ℓ_{nom} (mm)	Phase	f_1 (GHz)	$\Delta f_1^{\text{Ch}N}$ (%)
12 (A)	Pre	4.739 ± 0.003	-1.69 ± 0.07
	Ch10	4.659 ± 0.002	
12 (B)	Pre	4.756 ± 0.003	-1.39 ± 0.08
	Ch6	4.690 ± 0.002	
14	Pre	4.077 ± 0.003	-3.19 ± 0.10
	Ch8	3.947 ± 0.003	
18	Pre	3.360 ± 0.004	-1.10 ± 0.16
	Ch9	3.324 ± 0.003	

Table 5.2: Summary of the maximum relative downshift found in the cholesterol tests performed. From left to right, columns indicate nominal length (ℓ_{nom}), phase label, fundamental resonance frequency (f_1), and maximum relative downshift ($\Delta f_1^{\text{Ch}N}$).

the fundamental resonance, we define the relative discrepancy of the actual diameter, the actual length and the fundamental resonance frequency, respectively, as follows:

$$\Delta d_{\text{Post}} \equiv \frac{d_{\text{Post}} - d_{\text{Pre}}}{d_{\text{Pre}}}, \tag{5.2a}$$

$$\Delta \ell_{\text{Post}} \equiv \frac{\ell_{\text{Post}} - \ell_{\text{Pre}}}{\ell_{\text{Pre}}}, \tag{5.2b}$$

$$\Delta f_1^{\text{Post}} \equiv \frac{f_1^{\text{Post}} - f_1^{\text{Pre}}}{f_1^{\text{Pre}}}. \tag{5.2c}$$

Table 5.3 summarizes the cross-check measurements for d, ℓ and f_1. When we compare d_{Pre} and d_{Post} (top of the table), we first notice that the four stents experienced a slight reduction in d. In any case, Δd_{Post} estimates never exceeded -1% and the difference between d_{Pre} and d_{Post} resulted not significant considering the uncertainties involved. Similarly, ℓ also experienced a systematic reduction in all cases (mid table). This time, however, the difference between ℓ_{Pre} and ℓ_{Post} resulted significant. Notice how $\Delta \ell_{\text{Post}}$ values exceed -1% and raise up to almost -3%. We presume that this size reduction could be ascribed to a compression strain exerted by the repeated crystallization of cholesterol crust. Therefore, we may immediately disregard that an eventual increase in ℓ can lie behind the downshift

ℓ_{nom} (mm)	Phase	d (mm)	Δd_{Post} (%)
12 (A)	Pre	2.763 ± 0.006	-0.9 ± 0.3
	Post	2.739 ± 0.006	
12 (B)	Pre	2.732 ± 0.007	-0.8 ± 0.4
	Post	2.711 ± 0.006	
14	Pre	2.794 ± 0.007	-0.7 ± 0.4
	Post	2.774 ± 0.009	
18	Pre	2.782 ± 0.007	-0.8 ± 0.3
	Post	2.760 ± 0.006	

ℓ_{nom} (mm)	Phase	ℓ (mm)	$\Delta \ell_{\text{Post}}$ (%)
12 (A)	Pre	12.442 ± 0.012	-1.42 ± 0.14
	Post	12.265 ± 0.013	
12 (B)	Pre	12.547 ± 0.012	-2.89 ± 0.16
	Post	12.184 ± 0.016	
14	Pre	15.078 ± 0.013	-2.74 ± 0.12
	Post	14.665 ± 0.013	
18	Pre	18.931 ± 0.011	-1.06 ± 0.08
	Post	18.731 ± 0.011	

ℓ_{nom} (mm)	Phase	f_1 (GHz)	Δf_1^{Post} (%)
12 (A)	Pre	4.739 ± 0.003	0.33 ± 0.08
	Post	4.755 ± 0.003	
12 (B)	Pre	4.756 ± 0.003	0.58 ± 0.10
	Post	4.783 ± 0.004	
14	Pre	4.077 ± 0.003	1.43 ± 0.10
	Post	4.135 ± 0.003	
18	Pre	3.360 ± 0.004	0.62 ± 0.19
	Post	3.381 ± 0.005	

Table 5.3: Summary of the relative discrepancies found for the four MDS stents submitted to cholesterol tests. From left to right, columns indicate nominal length (ℓ_{nom}), phase label, cross-checked magnitude and its corresponding relative discrepancy [d and Δd_{Post} (top), ℓ and $\Delta \ell_{\text{Post}}$ (mid), f_1 and Δf_1^{Post} (bottom), respectively].

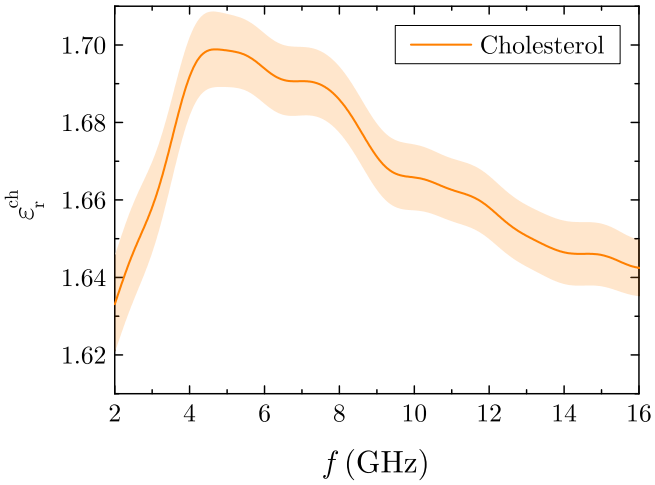

Figure 5.7: Relative dielectric permittivity of cholesterol versus the microwave frequency, $\varepsilon_r^{\mathrm{ch}}(f)$. The shaded band represents the corresponding uncertainty region.

behavior observed in cholesterol tests. We just need to recall the reciprocal dependence between f_n and ℓ in Equation 3.10. As for the behavior of f_1 (bottom of the table), after removing the cholesterol crust and measuring f_1^{Post}, we always recover original f_1^{Pre} values. Nevertheless, the resulting f_1^{Post} estimates systematically overcome f_1^{Pre}. The values of $\Delta f_1^{\mathrm{Post}}$ range from 0.3% to 1.5%, and despite being moderate, the mismatch between f_1^{Pre} and f_1^{Post} is always significant. Finally, we understand that the longitudinal shrinkage previously discussed is behind the mismatch between f_1^{Pre} and f_1^{Post}.

5.4 The dielectric perturbation model

In view of the control check results, we can ensure that the presence of cholesterol around a stent shifts its fundamental resonance frequency down. This fact stands reasonable just remembering the $1/\sqrt{\varepsilon_r}$ factor in Equation 3.10. As other biomolecules typically present in biological tissues, cholesterol should exhibit a relative dielectric permittivity, $\varepsilon_r^{\mathrm{ch}}$, greater than one in the microwave range. We took advantage of a commercial instrument[7] in order to have a first-

[7] 85070C Dielectric Probe Kit, Agilent Technologies, Santa Clara, CA, USA.

hand estimation of the dielectric properties of cholesterol. We used this probe-based device to measure $\varepsilon_r^{\text{ch}}(f)$ from a sample made of compressed crystalline cholesterol powder. Figure 5.7 provides the corresponding characterization between 2 GHz and 16 GHz. In this frequency span, $\varepsilon_r^{\text{ch}}(f)$ ranges from 1.61 to 1.71, which turns out just moderately higher than $\varepsilon_r^{\text{air}} \simeq 1$.

Since we have seen that $\varepsilon_r^{\text{ch}}$ is not much greater than $\varepsilon_r^{\text{air}}$, let us think in terms of a perturbation of an electromagnetic resonator [29]. With this idea in mind, we can understand the process of progressive cholesterol deposition like an increasing dielectric material perturbation dependent on the cholesterol mass applied, $\Delta\varepsilon_r^{\text{ch}}(m)$. Thus, the relative permittivity seen by the stent should become

$$\varepsilon_r(m) = \varepsilon_r^{\text{air}} + \Delta\varepsilon_r^{\text{ch}}(m). \tag{5.3}$$

Additionally, let us assume that for a cholesterol mass large enough the dielectric perturbation saturates and matches the relative permittivity of cholesterol. Taking this into account we can rewrite $\Delta\varepsilon_r^{\text{ch}}(m)$ as follows:

$$\Delta\varepsilon_r^{\text{ch}}(m) = \frac{m}{m_{\text{sat}}}\left(\varepsilon_r^{\text{ch}} - \varepsilon_r^{\text{air}}\right), \tag{5.4}$$

where $0 \leq m \leq m_{\text{sat}}$ and m_{sat} is the saturation cholesterol mass. Intuitively, we foresee that m_{sat} should be proportional to the stent size. The larger the ℓd product for a given stent, the higher its associated m_{sat} should be. Merging Equations 5.3 and 5.4 we can express the relative permittivity seen by the stent as cholesterol deposition advances:

$$\varepsilon_r(m) = \varepsilon_r^{\text{air}}\left[1 + \frac{m}{m_{\text{sat}}}\left(\frac{\varepsilon_r^{\text{ch}} - \varepsilon_r^{\text{air}}}{\varepsilon_r^{\text{air}}}\right)\right]. \tag{5.5}$$

Notice the way in which $\varepsilon_r(m)$ rules the whole downshift course. Before starting cholesterol deposition $\varepsilon_r(0) = \varepsilon_r^{\text{air}}$, whilst once reached the saturation mass $\varepsilon_r(m_{\text{sat}}) = \varepsilon_r^{\text{ch}}$. Now, by combining Equations 5.5 and 3.10, we are able to link the nth-order resonance frequency of a given stent with the cholesterol mass deposited in it:

$$f_n(m) = \frac{nc\xi(m)}{2a\ell\sqrt{\varepsilon_r^{\text{air}}\mu_r^{\text{air}}}} + f_n^{\text{off}}, \tag{5.6}$$

where we have defined $\xi(m)$ as follows:

$$\xi(m) \equiv \frac{1}{\sqrt{1 + \frac{m}{m_{\text{sat}}} \left(\frac{\varepsilon_r^{\text{ch}} - \varepsilon_r^{\text{air}}}{\varepsilon_r^{\text{air}}} \right)}}. \tag{5.7}$$

At this point, we can find a theoretical expression for the relative frequency downshift as a function of the cholesterol mass deposited in the stent:

$$\Delta f_n(m) \equiv \frac{f_n(m) - f_n(0)}{f_n(0)}, \tag{5.8}$$

which using Equation 5.6 becomes:

$$\Delta f_n \left({}^{m}\!/_{m_{\text{sat}}} \right) = - \frac{1 - \xi\left({}^{m}\!/_{m_{\text{sat}}} \right)}{\left(1 + \frac{2a\ell f_n^{\text{off}} \sqrt{\varepsilon_r^{\text{air}} \mu_r^{\text{air}}}}{nc} \right)}. \tag{5.9}$$

In this last step we have switched the independent variable from m ($0 \leq m \leq m_{\text{sat}}$) to the ratio ${}^{m}\!/_{m_{\text{sat}}}$ ($0 \leq {}^{m}\!/_{m_{\text{sat}}} \leq 1$). This will allow us to represent such theoretical dependence without the prior assessment of m_{sat}. By inspecting the denominator of Equation 5.9, we understand that the relative downshift of a given stent should be proportional to n and inversely proportional to ℓ, a and f_n^{off}. For completeness, we can finally obtain the analytical expression for the maximum relative downshift theoretically achievable, $\Delta f_n^{\max}$, just by particularizing Equation 5.9 for ${}^{m}\!/_{m_{\text{sat}}} = 1$:

$$\Delta f_n^{\max} = - \frac{1 - \sqrt{{}^{\varepsilon_r^{\text{air}}}\!/_{\varepsilon_r^{\text{ch}}}}}{\left(1 + \frac{2a\ell f_n^{\text{off}} \sqrt{\varepsilon_r^{\text{air}} \mu_r^{\text{air}}}}{nc} \right)}. \tag{5.10}$$

If we read the dependence between $\Delta f_n^{\max}$ and $\varepsilon_r^{\text{ch}}$ in this last equation carefully, we realize that the larger the relative dielectric permittivity of the perturbing material is, the higher its associated maximum relative downshift would be.

5.5 Cholesterol tests analysis

Color lines in Figure 5.8 represent the theoretical relative downshift curves for the four stents investigated. Table 5.4 summarizes the values of the empirical parameters introduced in Equation 5.9 to obtain

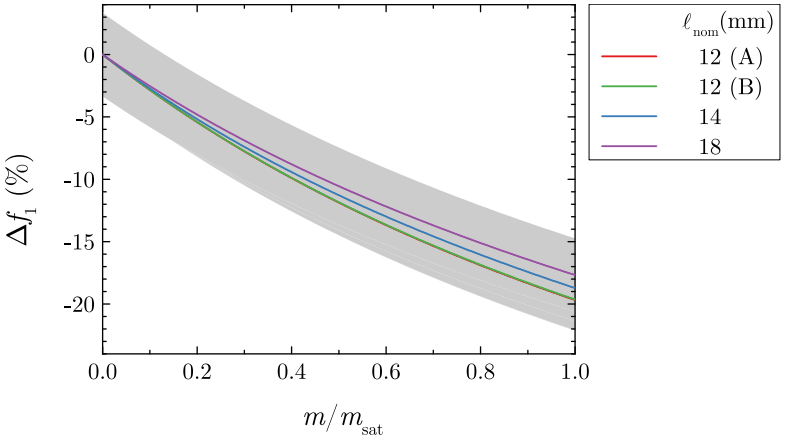

Figure 5.8: Theoretical relative downshift of the fundamental resonance frequency versus the actual cholesterol mass deposited in the stent divided by the saturation cholesterol mass, $\Delta f_1(m/m_{\text{sat}})$, for the four stents investigated in cholesterol tests. The shaded band represents the corresponding uncertainty region.

ℓ_{nom} (mm)	ℓ (mm)	a	f_1^{off} (GHz)
12 (A)	12.442±0.012	2.95±0.05	0.69±0.06
12 (B)	12.547±0.012		
14	15.078±0.013		
18	18.931±0.011		

Table 5.4: Parameters introduced in Equation 5.9 to obtain the theoretical relative downshift curves shown in Figure 5.8. From left to right, columns indicate nominal length (ℓ_{nom}), actual length (ℓ), scaling factor (a) and frequency offset (f_1^{off}). For ℓ we took ℓ_{Pre} [see Table 5.3 (mid)]. For a and f_1^{off} we used the estimates previously determined in Chapter 3 corresponding to the stent family $d_{\text{nom}} = 2.50$ mm (see Table 3.4).

ℓ_{nom} (mm)	$\Delta f_1^{\max}$ (%)	$\Delta f_1^{\text{Ch}N}$ (%)
12 (A)	-20 ± 2	-1.69 ± 0.07
12 (B)	-20 ± 2	-1.39 ± 0.08
14	-19 ± 3	-3.19 ± 0.10
18	-18 ± 3	-1.10 ± 0.16

Table 5.5: Comparison between theoretical and experimental maximum relative downshifts for the four stents submitted to cholesterol tests. From left to right, columns indicate nominal length (ℓ_{nom}), theoretical maximum relative downshift ($\Delta f_1^{\max}$) and experimental maximum relative downshifts reached at the last Cholesterol subphase ($\Delta f_1^{\text{Ch}N}$).

such curves. It should be mentioned that the relative permittivity of cholesterol we took to plot each line was numerically obtained from the $\varepsilon_r^{\text{ch}}(f)$ data shown in Figure 5.7. As usual, we also considered that $\varepsilon_r^{\text{air}} \simeq 1 \simeq \mu_r^{\text{air}}$. From Figure 5.8 we note that shorter stents exhibit slightly faster downshift rates. In general, the experimental results we provided in Figure 5.6 seem to be in good agreement with this. However, the data series $\ell_{\text{nom}} = 14$ mm presents an unexpectedly high downshift slope. We think that this anomaly could emerge from the cholesterol deposition process itself. The random growth of cholesterol crystals around stent crowns can give slightly different porosities to each cholesterol crust. Such porosity fluctuations would ultimately give account of the variability among the downshift rates experimentally found.

In addition, from Figure 5.8 we also notice that the theoretical estimates for the maximum relative downshift range between -17% and -20%, resulting much higher than the experimental values obtained, which ranged between -1% and -3%. Table 5.5 compares theoretical and experimental maximum relative downshifts ($\Delta f_1^{\max}$ and $\Delta f_1^{\text{Ch}N}$, respectively) for the four stents submitted to cholesterol tests. Notice how $\Delta f_1^{\max}$ is significantly higher than $\Delta f_1^{\text{Ch}N}$ in all cases. This fact strongly suggests that the m values we have handled along the four cholesterol tests performed have fallen far short from m_{sat} and thus we never get close to the saturation regime.

Figure 5.9: Micropictures showing the actual look of a real ISNA situation. The longitudinally transected arterial section shows a translucent neointima containing a Cordis Cypher® sirolimus-eluting stent[8]. Eventually, the atherosclerotic transformation of the neointima artery layer inside the stent triggered the formation of a small thrombus at the distal end (see dark reddish spot on the top image). Figure adapted from Ref. [23].

5.6 Conclusions

Along this chapter we have tested the ability of our MWS-based approach for the detection of in-stent neoatherosclerosis. We have emulated the atherosclerotic transformation inside a stent by means of a staged process of increasing cholesterol deposition in free space conditions. The absorbance diagrams generated by a stent submitted to this procedure have provided an indicator for a growing presence of cholesterol around a stent: an slight but steady downshift of f_1. This means that microwave spectrometry could potentially warn the onset of an eventual atherosclerotic transformation inside a stent. This drift towards lower frequencies is unequivocally ascribed to the presence of cholesterol and, despite being moderate, was significant for the four stents investigated. In this regard, we suspect that for a cholesterol mass large enough, the downshift observed should keep increasing up to the theoretical limit established by Equation 5.10. However, by just reminding the morphology of in-stent neoatherosclerotic lesions

[8]Cordis Corporation, Fremont, CA, USA.

introduced in Section 5.1, we realize that our cholesterol test only accounts for the cholesterol crystals that are found within the lipid cores and are also scattered throughout the extracellular matrix of the artery wall cells. In a real situation (see Figure 5.9), the nature and the spatial distribution of the atherosclerotic tissue around an implanted stent are much more complex than our cholesterol-based model. Some questions seem then appropriate: What is the true value of the effective relative permittivity around an implanted stent along a real process of neointimal atherosclerotic transformation? What effect does a non-uniform plaque distribution have on the stent resonance frequencies? A systematic analysis using finite-difference time-domain methods [30] would represent a good starting point to answer. At this stage we are not able to link a given relative downshift with a quantitative clinical indicator, such as the total stent lumen area occlusion or the spatial distribution of the atherosclerotic transformation inside the stent. We think that the computational approach previously proposed along with additional experiments using more reliable stent environments would ultimately lead to obtaining a MWS-based indicator for ISNA.

References

[1] K. Hasegawa, H. Tamai, E. Kyo, K. Kosuga, S. Ikeguchi, T. Hata, M. Okada, S. Fujita, T. Tsuji, S. Takeda, R. Fukuhara, Y. Kikuta, S. Motohara, K. Ono, and E. Takeuchi, "Histopathological findings of new in-stent lesions developed beyond five years," Catheterization and Cardiovascular Interventions **68**, 554–558 (2006) (cit. on p. 96).

[2] M. S. Chen, J. M. John, D. P. Chew, D. S. Lee, S. G. Ellis, and D. L. Bhatt, "Bare metal stent restenosis is not a benign clinical entity," American Heart Journal **151**, 1260–1264 (2006) (cit. on p. 96).

[3] T. Higo, Y. Ueda, J. Oyabu, K. Okada, M. Nishio, A. Hirata, K. Kashiwase, N. Ogasawara, S. Hirotani, and K. Kodama, "Atherosclerotic and thrombogenic neointima formed over sirolimus drug-eluting stent: an angioscopic study," JACC: Cardiovascular Imaging **2**, 616–624 (2009) (cit. on p. 96).

[4] S.-J. Kang, G. S. Mintz, D.-W. Park, S.-W. Lee, Y.-H. Kim, C. W. Lee, K.-H. Han, J.-J. Kim, S.-W. Park, and S.-J. Park, "Tissue characterization of in-stent neointima using intravascular ultrasound radiofrequency data analysis," American Journal of Cardiology **106**, 1561–1565 (2010) (cit. on p. 96).

[5] S.-J. Park, S.-J. Kang, R. Virmani, M. Nakano, and Y. Ueda, "In-stent neoatherosclerosis: a final common pathway of late stent failure," Journal of the American College of Cardiology **59**, 2051–2057 (2012) (cit. on p. 96).

[6] F. Otsuka, R. A. Byrne, K. Yahagi, H. Mori, E. Ladich, D. R. Fowler, R. Kutys, E. Xhepa, A. Kastrati, R. Virmani, and M. Joner, "Neoatherosclerosis: overview of histopathologic findings and implications for intravascular imaging assessment," European Heart Journal **36**, 2147–2159 (2015) (cit. on p. 96).

[7] H. Komiyama, M. Takano, N. Hata, Y. Seino, W. Shimizu, and K. Mizuno, "Neoatherosclerosis: coronary stents seal atherosclerotic lesions but result in making a new problem of atherosclerosis," World Journal of Cardiology **7**, 776–783 (2015) (cit. on p. 96).

[8] R. Virmani, A. P. Burke, F. D. Kolodgie, and A. Farb, "Pathology of the thin-cap fibroatheroma: a type of vulnerable plaque," Journal of Interventional Cardiology **16**, 267–272 (2003) (cit. on p. 96).

[9] T. Inoue, T. Shinke, H. Otake, M. Nakagawa, H. Hariki, T. Osue, M. Iwasaki, Y. Taniguchi, R. Nishio, N. Hiranuma, A. Konishi, H. Kinutani, J. Shite, and K.-i. Hirata, "Neoatherosclerosis and mural thrombus detection after sirolimus-eluting stent implantation," Circulation Journal **78**, 92–100 (2014) (cit. on p. 96).

[10] *What is coronary heart disease?* National Heart, Lung, Blood Institute; National Institute of Health; U.S. Department of Health, and Human Services, (2017) `https://www.nhlbi.nih.gov/` (cit. on p. 97).

[11] T. Yonetsu, K. Kato, S.-J. Kim, L. Xing, H. Jia, I. McNulty, H. Lee, S. Zhang, S. Uemura, Y. Jang, S.-J. Kang, S.-J. Park, S. Lee, B. Yu, T. Kakuta, and I.-K. Jang, "Predictors for neoatherosclerosis: a retrospective observational study from the optical coherence tomography registry," Circulation: Cardiovascular Imaging **5**, 660–666 (2012) (cit. on pp. 96, 98).

[12] G. Nakazawa, F. Otsuka, M. Nakano, M. Vorpahl, S. K. Yazdani, E. Ladich, F. D. Kolodgie, A. V. Finn, and R. Virmani, "The pathology of neoatherosclerosis in human coronary implants: bare-metal and drug-eluting stents," Journal of the American College of Cardiology **57**, 1314–1322 (2011) (cit. on pp. 96, 98, 99).

[13] T. Yonetsu, J.-S. Kim, K. Kato, S.-J. Kim, L. Xing, R. W. Yeh, R. Sakhuja, I. McNulty, H. Lee, S. Zhang, S. Uemura, B. Yu, T. Kakuta, and I.-K. Jang, "Comparison of incidence and time course of neoatherosclerosis between bare metal stents and drug-eluting stents using optical coherence tomography," American Journal of Cardiology **110**, 933–939 (2012) (cit. on pp. 96, 98).

[14] R. Vergallo, T. Yonetsu, S. Uemura, S.-J. Park, S. Lee, K. Kato, H. Jia, F. Abtahian, J. Tian, S. Hu, H. Lee, I. McNulty, A. Prasad, B. Yu, S. Zhang, I. Porto, L. M. Biasucci, F. Crea, and I.-K. Jang, "Correlation between degree of neointimal hyperplasia and incidence and characteristics of neoatherosclerosis as

assessed by optical coherence tomography," American Journal of Cardiology **112**, 1315–1321 (2013) (cit. on pp. 96, 98).

[15] S. Yokoyama, M. Takano, M. Yamamoto, S. Inami, S. Sakai, K. Okamatsu, S. Okuni, K. Seimiya, D. Murakami, T. Ohba, R. Uemura, Y. Seino, N. Hata, and K. Mizuno, "Extended follow-up by serial angioscopic observation for bare-metal stents in native coronary arteries: from healing response to atherosclerotic transformation of neointima," Circulation: Cardiovascular Interventions **2**, 205–212 (2009) (cit. on p. 98).

[16] N. Kipshidze, G. Dangas, M. Tsapenko, J. Moses, M. B. Leon, M. Kutryk, and P. Serruys, "Role of the endothelium in modulating neointimal formation: vasculoprotective approaches to attenuate restenosis after percutaneous coronary interventions," Journal of the American College of Cardiology **44**, 733–739 (2004) (cit. on p. 98).

[17] G. Nakazawa, A. V. Finn, M. Vorpahl, E. Ladich, R. Kutys, I. Balazs, F. D. Kolodgie, and R. Virmani, "Incidence and predictors of drug-eluting stent fracture in human coronary artery: a pathologic analysis," Journal of the American College of Cardiology **54**, 1924–1931 (2009) (cit. on p. 98).

[18] A. V. Finn, and F. Otsuka, "Neoatherosclerosis: a culprit in very late stent thrombosis," Circulation: Cardiovascular Interventions **5**, 6–9 (2012) (cit. on p. 98).

[19] A. Al Mamary, G. Dariol, and M. Napodano, "Neo-atherosclerosis in very late stent thrombosis of drug eluting stent," Journal of the Saudi Heart Association **26**, 226–230 (2014) (cit. on p. 98).

[20] J. Hou, H. Qi, M. Zhang, L. Ma, H. Liu, Z. Han, L. Meng, S. Yang, S. Zhang, B. Yu, and I.-K. Jang, "Development of lipid-rich plaque inside bare metal stent: possible mechanism of late stent thrombosis? an optical coherence tomography study," Heart **96**, 1187–1190 (2010) (cit. on p. 98).

[21] K. Yamaji, K. Inoue, T. Nakahashi, M. Noguchi, T. Domei, M. Hyodo, Y. Soga, S. Shirai, K. Ando, K. Kondo, K. Sakai, M. Iwabuchi, H. Yokoi, H. Nosaka, M. Nobuyoshi, and T. Kimura, "Bare metal stent thrombosis and in-stent neoatherosclerosis,"

Circulation: Cardiovascular Interventions **5**, 47–54 (2012) (cit. on p. 98).

[22] S.-J. Kang, C. W. Lee, H. Song, J.-M. Ahn, W.-J. Kim, J.-Y. Lee, D.-W. Park, S.-W. Lee, Y.-H. Kim, G. S. Mintz, S.-W. Park, and S.-J. Park, "OCT analysis in patients with very late stent thrombosis," JACC: Cardiovascular Imaging **6**, 695–703 (2013) (cit. on p. 98).

[23] F. Otsuka, A. V. Finn, S. K. Yazdani, M. Nakano, F. D. Kolodgie, and Virmani, "The importance of the endothelium in atherothrombosis and coronary stenting," Nature Reviews Cardiology **9**, 439–453 (2012) (cit. on pp. 99, 114).

[24] H. M. van Beusekom, D. M. Whelan, S. H. Hofma, S. C. Krabbendam, V. W. van Hinsbergh, P. D. Verdouw, and W. J. van der Giessen, "Long-term endothelial dysfunction is more pronounced after stenting than after balloon angioplasty in porcine coronary arteries," Journal of the American College of Cardiology **32**, 1109–1117 (1998) (cit. on p. 99).

[25] C. Rogers, D. Y. Tseng, J. C. Squire, and E. R. Edelman, "Balloon-artery interactions during stent placement," Circulation Research **84**, 378–383 (1999) (cit. on p. 99).

[26] P. M. Vanhoutte, "Endothelial dysfunction," Circulation Journal **73**, 595–601 (2009) (cit. on p. 99).

[27] J. M. Jiménez, and P. F. Davies, "Hemodynamically driven stent strut design," Annals of Biomedical Engineering **37**, 1483–1494 (2009) (cit. on p. 99).

[28] *Driver sprint rapid exchange coronary stent system, Instructions for use*, Revision B (2011) (cit. on p. 100).

[29] D. M. Pozar, *Microwave engineering* (Wiley, New York, 1998) (cit. on p. 110).

[30] A. Taflove, and S. C. Hagness, *Computational electrodynamics: the finite-difference time-domain method* (Artech House, Massachusetts, 2005) (cit. on p. 115).

6

General conclusions and future work

6.1 Conclusions

Throughout this thesis we have assessed the prospects of microwave spectrometry as a non-ionizing non-invasive monitoring alternative for stented patients in a very early proof-of-concept stage.

In Chapter 1 we have provided a generalist retrospective medical background along with a state-of-the-art summary of existing microwave-based stent monitoring approaches. First, we have introduced cardiovascular and circulatory diseases in general, and ischemic heart disease in particular. Next we have reviewed how percutaneous coronary interventions addressed the medical problem represented by atherosclerosis, giving a special emphasis to balloon angioplasty, bare-metal stenting and drug-eluting stenting. We have further exposed how the outcomes of such revolutionary strategies were compromised by the high rates of post-procedural complications (such is-stent restenosis and stent thrombosis), making unavoidable the invasive and ionizing follow-up of stented patients. Finally, we have summarized existing non-invasive and non-ionizing stent monitoring alternatives based in microwave techniques.

In Chapter 2 we have introduced the working principle of our microwave spectrometry setup. We have first presented how this arrangement is able to obtain the absorbance of a stent as a function of the frequency and the incidence angle of the microwave fields. We have also shown how these data are combined in a single two-dimensional chart, and how we recognize therein the characteristic

resonance frequencies of stents at a glance. As an example, we have presented a typical absorbance diagram to illustrate the general features of such resonances. In particular we have highlighted that these resonances are discrete and have multi-lobed angular patterns.

In Chapter 3 we have characterized a large number of stents having a wide variety of nominal sizes to better understand their characteristic resonances in terms of microwave scattering. First, we have found that the resonance frequency obeys a reciprocal dependence on the stent length. This has allowed us to obtain an empirical expression for such relationship just by adjusting two fitting parameters. However, we have not been able to find an analogous expression for the dependence on the stent diameter. In any case, while investigating the latter, we have unexpectedly uncovered how the particular stent architecture influences the corresponding resonance frequencies. By gathering all these individual results we have finally suggested a straightforward half-theoretical half-empirical model linking the resonance frequencies of stents with their structural integrity (through their length), with their particular architecture (through the scaling factor), as well as with their surrounding medium (through the relative dielectric permittivity and the relative magnetic permeability). We have also theoretically estimated the resonance frequencies of implanted stents from their corresponding values in free space conditions, showing that *in vivo* resonance frequencies should be around one order of magnitude smaller than their free space counterparts.

Finally, in Chapters 4 and 5 we have explored the potential diagnostic capabilities of microwave spectrometry in two possible scenarios: stent fracture and in-stent neoatherosclerosis. We have started both chapters reviewing the incidence, the medical implications, and the mechanism of these two stent-related complications. Stent fracture has been evaluated in Chapter 4 by means of two "fracture tests" consisting in a successive series of strut cuts. We have shown that microwave spectrometry provides qualitative indicators for single and multiple strut fractures (downshift of the fundamental resonance frequency), and also quantitative indicators for single or multiple complete transverse linear stent fractures (split and upshift of that frequency). In-stent neoatherosclerosis has been evaluated in Chapter 5 by means of four "cholesterol tests" consisting in a gradual process of increasing cholesterol deposition. We have shown that microwave spectrometry provides an indicator for a growing

presence of cholesterol around a stent (downshift of the fundamental resonance frequency). We have concluded this chapter calculating the theoretical evolution of the resonance frequencies along a cholesterol deposition process, estimating the upper limit for the resonance frequency displacement. Taking together the results we have reported in Chapters 4 and 5, we have shown that microwave spectrometry could potentially warn about stent fracture and in-stent neoatherosclerosis.

6.2 Future work

We have shown that it is feasible to obtain relevant information about the structural integrity and the environment of a stent without the incorporation of bulky electronic add-ons on its scaffold. As physicists, we have focused our efforts on answering the *whys* and the *whats*: Why stents exhibit characteristic absorbance resonance frequencies in the microwave range? Why these fingerprints depend on the stent length, the stent architecture and the surrounding medium? What stent-related complications could be reported by microwave spectrometry and what not? Now is time to answer the *hows*. How could we report in-stent restenosis or stent thrombosis? And most important: How could we translate this technology to the clinical arena? At this point we immediately glimpse a "long curvy road" in front of us.

One possible roadmap would pass through the parallel implementation of phantom-based testings and simulations. The combined results of this coordinate route would establish a robust trial-and-error approach which ultimately would lead to a next phase comprising more reliable tests. The following stage should pursue the validation of microwave spectrometry by means of *ex vivo* and *in vivo* porcine animal models as the prelude to future clinical trials. The most important obstacle along this road would be the power loss experienced by the electromagnetic wave while propagating across a lossy medium such as a biological tissue. Both the absorption and the multiple dielectric boundaries that the propagating electromagnetic wave will encounter may end up completely attenuating it. To overcome these issues a good tool would be the use of wideband dual linearly polarized sinuous antennas[1] in order to confine the stent axis and the

[1] QSI-DL-0.2-2-N-SG, Steatite Antennas, Leominster, Herefordshire, UK.

propagating electric field in the same plane and thus enhance the resonant scattering of the incident wave. Another option would be the use of high power electromagnetic pulses finely tuned below the accepted SAR (specific absorption rate) limits.

We believe there is still much more room for improvement, but it is quite clear that such upgrades will require an active collaboration between people from distant disciplines, such as physicists, engineers, veterinarians and physicians. Therefore, we could see this "long curvy road" just like another example highlighting that science is becoming more and more interdisciplinary.

List of publications

Thesis publications

[1] G. Arauz-Garofalo, V. López-Domínguez, J. M. Hernàndez, O. Rodríguez-Leor, A. Bayés-Genís, J. M. O'Callaghan, A. García-Santiago, and J. Tejada, "Microwave spectrometry for the evaluation of the structural integrity of metallic stents," Medical Physics **41**, 041902–041914 (2014).

[2] G. Arauz-Garofalo, V. López-Domínguez, J. M. Hernàndez, O. Rodríguez-Leor, A. Bayés-Genís, J. M. Rius, J. M. O'Callaghan, A. García-Santiago, and J. Tejada, "RF monitoring of commercial vascular stents with dipole scattering resonances," in 2014 IEEE MTT-S International Microwave Symposium (IMS2014) (2014), pp. 1–4.

[3] G. Arauz-Garofalo, L. M. Camacho-Puerma, A. García-Santiago, and J. Tejada, "Microwave spectrometry for the evaluation of in-stent neoatherosclerosis," Biomedical Physics & Engineering Express **1**, 035202–035210 (2015).

[4] O. Rodríguez-Leor, G. Arauz-Garofalo, J. M. O'Callaghan, A. García-Santiago, J. Tejada, E. Fernández-Nofrerias, X. Carrillo, J. Mauri, C. Gálvez-Montón, and A. Bayés-Genís, "Microwave spectrometry for coronary stent characterization," - (In preparation) (2017).

[5] C. Gálvez-Montón, G. Arauz-Garofalo, C. Soler-Botija, S. Amorós-García-de-Valdecasas, F. D. Gerez-Britos, O. Rodríguez-Leor, A. Bayés-Genís, J. M. O'Callaghan, F. Macià, and J. Tejada, "In-vivo validation of microwave spectrometry for non-invasive stent monitoring," - (In preparation) (2017).

Other publications

[6] C. Seco-Martorell, V. López-Domínguez, G. Arauz-Garofalo, A. Redo-Sanchez, J. Palacios, and J. Tejada, "Goya's artwork imaging with terahertz waves," Opt. Express **21**, 17800–17805 (2013).